Geophysical Research Letters

Supporting Information for

Seismic and geodetic transients in Central Apennines from 2008 to 2018

Blaž Vičič[1], Abdelkrim Aoudia[1], Alessandra Borghi[1,2] Seyyedmaalek Momeni[1], Alessandro Vuan[3]

[1] The Abdus Salam International Centre for Theoretical Physics, Italy
[2] Istituto Nazionale Geofisica e Vulcanologia, sezione di Bologna, Italy
[3] Istituto Nazionale di Oceanografia e Geofisica Sperimentale, Italy

Introduction

This file includes 7 supplementary figures referred to in the main article as well as 3 additional Appendixes with information on Kinematic source inversion, its convergence and GPS data analysis.

Contents of this file

Supplementary figures from S1 to S7
Appendix A - Kinematic inversion of moderate magnitude events on the Campotosto fault
Appendix B - Inversion convergence
Appendix C - GPS data analysis

Supplementary figures

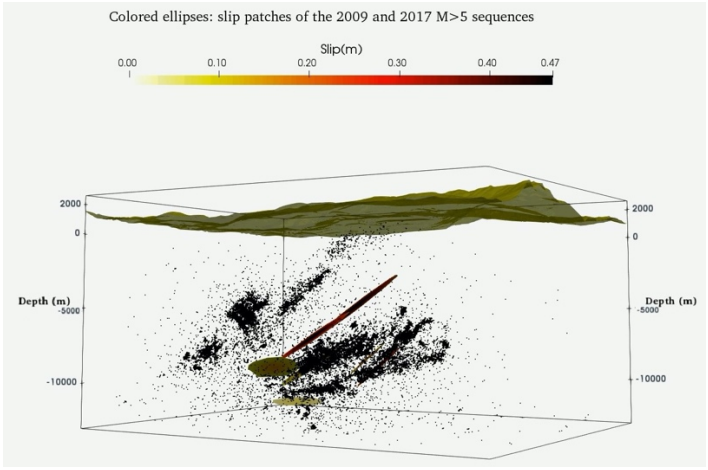

Figure S1: Campotosto fault. Kinematic source models and relocated seismicity of 2009 catalog (Valoroso et al., 2013). SE-NW view. Campotosto fault is a listric normal fault as observed from the relocated 2009 earthquake. Our inverted kinematic source models agree with the listricity and closely follow the geometry of the fault.

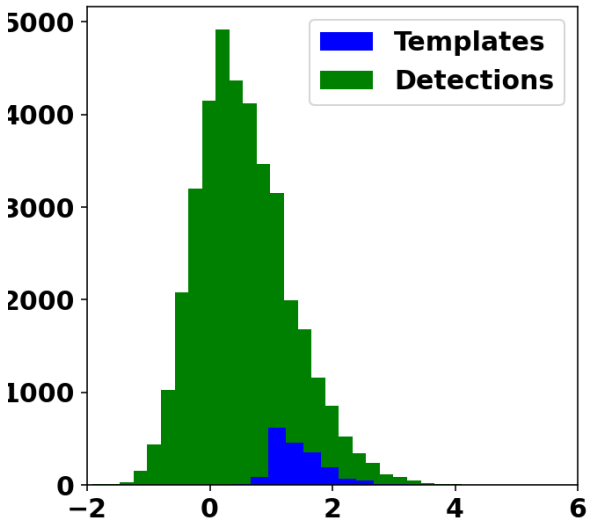

Figure S2: Binned number of detected (green) earthquakes vs number of templates (blue) used. We are able to detect much more small events that have been missed and see that some of the detected events that are larger than the maximum magnitude templates are similar to our templates used.

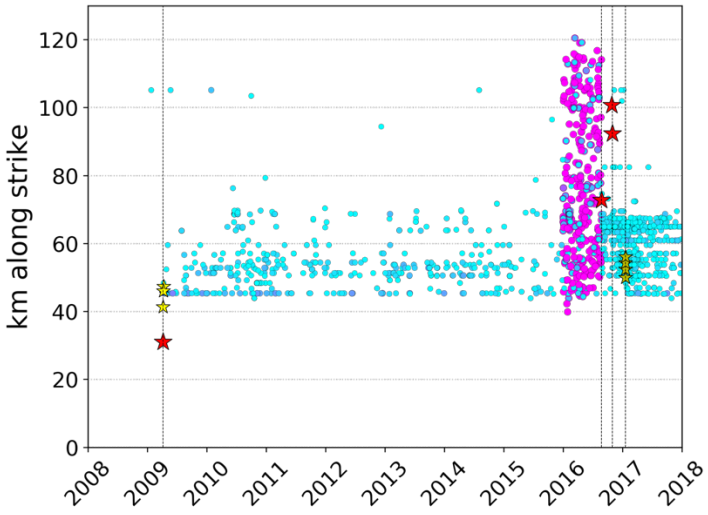

Figure S3a: Newley detected earthquakes and their cross-correlation values. Plotted detections are only those, that were detected by foreshocks of 2016 sequence. We see that using foreshocks we can detect numerous earthquakes along SZ underneath Campotosto fault while the SZ beneath Mt. Vettore does not exhibit a lot of seismicity.

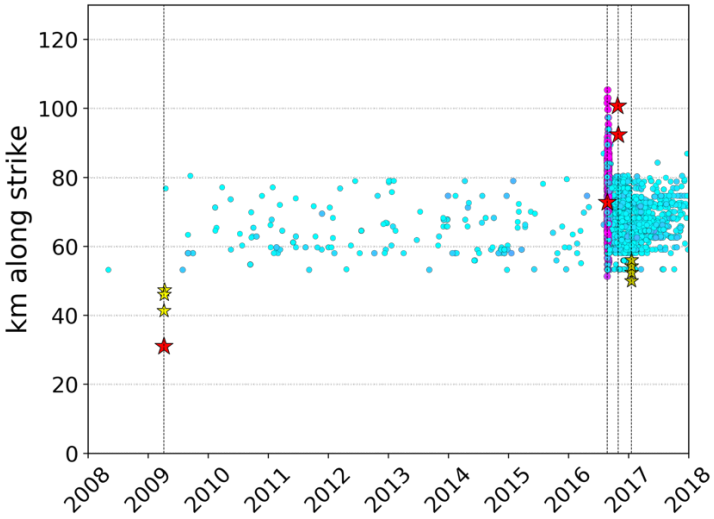

Figure S3b: Same as Fig S3a. Detections from templates of aftershocks of 24th August 2016 M6 earthquake. We see that SZ beneath Campotosto fault exhibit earthquakes in the time between 2009 and 2016 while, similarly to Fig S3a, we cannot detect anything in the Mt. Vettore region.

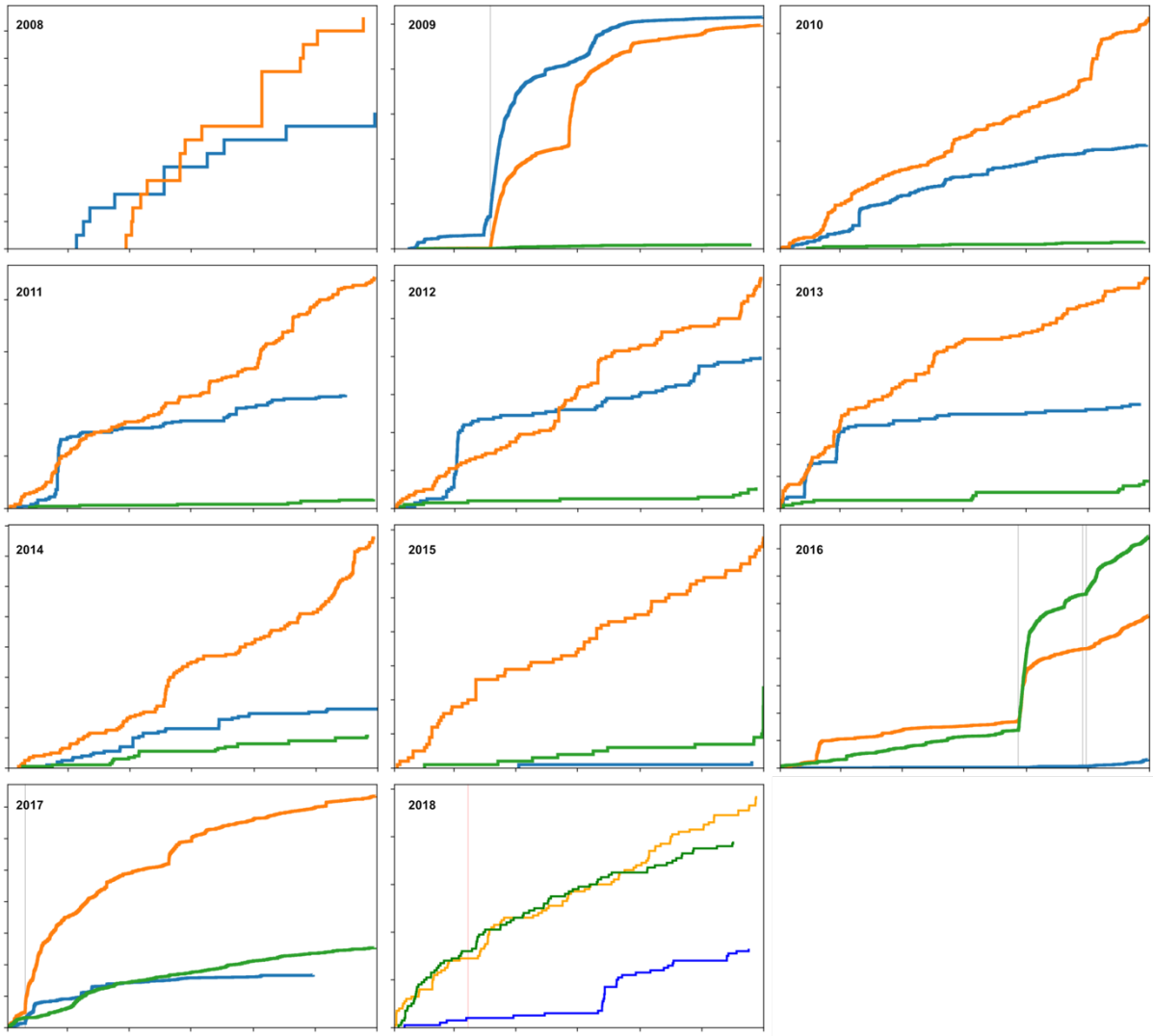

Figure S4: Yearly contribution to seismicity rate regarding the SZ segment. Blue – L'Aquila segment, Green – Mt. Vettore segment, Orange – Campotosto segment.In general Campotosto segment is the leading in terms of seismicity rate.

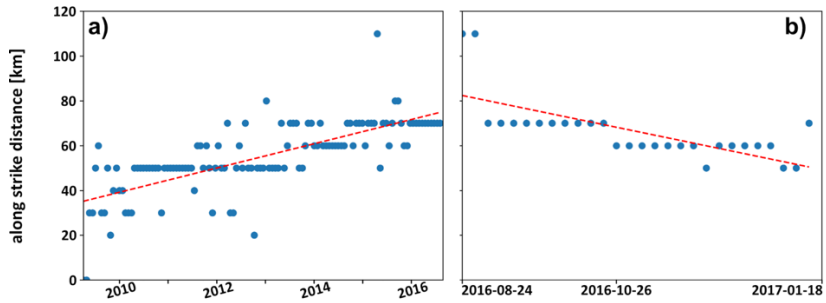

Figure S5: Along-strike distance vs time. a) represents time after the L'Aquila 2009 earthquake. We can observe slow migration of seismicity along the SZ towards the future 2016 Central Italy sequence. b) After the August 2016 event, faster migration towards Campotosto segment is observed.

Appendix-A. Kinematic inversion of moderate magnitude events on the Campotosto fault

The near field strong motion displacement time series of eight small to moderate magnitude ($4.4 \leq M \leq 5.4$) events that occurred on the Cf during 2009 and 2017 sequences are inverted for their source rupture histories (Fig. 2). We follow the inversion methodology explained in a recent study by Momeni et al., (2019). The acceleration waveforms are integrated twice to obtain the displacements. The horizontal components are rotated to E-W and N-S directions. The displacement wave-fields are mostly filtered in the frequency ranges from 0.08 Hz to 0.5 Hz (Figs. A1d to A8d). The low and high frequency ranges are defined to avoid the low frequency noises and considering the resolution provided by the used 1-D crustal velocity model, respectively. They cut from the origin time of each event for the length of 25.6 s. The Green's function produced by Axitra code (Cotton & Coutant, 1997). We used a velocity model for the Central Italian Apennines—CIA by Herrmann et al. (2011) that was slightly modified by Sugan et al., (2014) to fit high-frequency S-waves. The hypocenters reported by INGV are used as initiation points of ruptures (Table 1). Nine parameters explain an elliptical source model: five of them define the geometry of the ruptured area on a planar fault and the other four are slip amplitude, constant rupture velocity, average rake, and rise time. The hypocenters can move 1 km along both strike and dip to accommodate the probable error in their origin times. For each of the model parameters, we define wide ranges and apply the neighbourhood algorithm (Sambridge 1999a, b) to sample all possible models that can fit the best the displacement wave-fields. The produced synthetic displacements are compared to the observed ones using a cost function by Spudich and Miller, (1990).

First, for each event we search for the proper geometry of the ruptured area that can provide a model with the best waveform fit to the observed displacement wave-fields. Figures A1a to A8a are diagrams of the misfits of the obtained source models on the tested geometries of the ruptured areas. We used almost the same model parameters space for the inversion tests (i.e. semi-major/minor axis of ellipse: 1 Km-15 Km; maximum slip:0.1 m-5 m; rupture velocity:1 km/s-5 km/s; rake:90°-180°; rise time: 0.01 s-2 s). We note that the neighbour geometries to the preferred ones in the diagrams A1a to A8a show considerably higher rupture velocities which are not expected for such moderate magnitude events.

After choosing the proper geometry for each event (Table A1), 20 independent inversions ran with different parameters space to assure the independence of final rupture models to the defined parameters space. Then, for each event, 10 final rupture models with the most different features and having minimum misfits are selected to investigate their robust features (Tables S1 to S8).
The final source models obtained for these events are presented in Table-A1 and their waveform fit are shown in Figures A1d to A8d. The noisy components of stations did not use in the inversions, while we produce the regarding synthetic displacements at those components by forward modelling.

Table. A1. The final source rupture parameters of seven 4.4≤M≤5.5 events that occurred on the Campotosto fault during 2009 and 2017 seismic sequences. Np1 and np2 are the nodal planes obtained using point source inversion method reported by INGV.

No.	Event date-time	Ml	used stations	Hypocenter Lon.(°)/Lat.(°)/Dep(Km)	Frequency range (Hz)	Geometry Strike(°)/dip(°) (This study)	Rake(°)	Strike/Dip(°) np1&np2	M0 (Nm)	Mo Scognamiglio et al., 2010	Misfit (%)
1	**2009/4/6-23:15:36.76**	5.0	ANT, AQK, AQV, FMG, LSS, MTR	13.385/42.463/9.7	0.08-0.3	156/50	-82	154/57&316/34	3.23E+16	3.69 E+16	14.5
2	**2009/4/9-00:52:59.69**	5.2	ANT, AQV, GSA, MTR, PCB	13.351/42.489/11	0.08-0.5	152/46	-82	149/45&322/46	9.78E+16	8.25 E+16	10.1
3	**2009/4/9-19:38:16.96**	5.0	ANT, AQK, AQV, BRS, BZZ, FMG, GSA, GSG, MTR, PCB	13.350/42.504/9.3	0.1-0.5	147/48	-78	137/48&311/42	3.43E+16	3.46 E+16	7.4
4	**2009/06/22 20:58:40**	4.4	AMT, ANT, AQV, GSA, MTR, PZI1, SPD	13:35/42/45/10.8	0.2-0.6	60/15	-167	55/14&316/88	5.33E+15	4.37 E+15	8.8
5	**2017/01/18-09:25:40.39**	5.4	AMT, ANT, AQV, CSC, LSS, PCB, PZI1, SPD, TRL	13.277/42.545/10	0.08-0.5	150/30	-88	153/32&331/58	7.78E+16	-	9.5
6	**2017/01/18-10:14:09.9**	5.5	AMT, ANT, BRS, BZZ, CTD, GSA, LSS, PCB, PZI1, SPD, TRL	13.284/42.531/8	0.08-0.5	161/41	-69	161/51&335/39	2.78E+17	-	9.7
7	**2017/01/18-10:25:23.73**	5.4	AMT, ANT, AQV, BRS, BZZ, CTD, GSA, LSS, MSC, PCB, PGG, PZI1, TRL	13.277/42.503/9.4	0.08-0.5	142/37	-89	140/35&319/55	1.86E+17	-	9.5
8	**2017/01/18-13:33:36.74**	5.1	AMT, ANT, AQV, BZZ, FMG, GSA, LSS, PCB, PGG, PZI1,SPD,TRL	13.275/42.473/9.5	0.08-0.5	190/31	-43	188/30&313/71	4.48E+16	-	14.8

For all obtained source models, the rupture direction, its duration, rake angle and total scalar seismic moment obtained reasonably well. While the rupture dimension and its velocity trade-off with each other. The rupture velocity and rise time are also directly proportional to each other, and that is consistent with a study by Schmedes, et al., (2010). We note that for these small to moderate magnitude events rupture dimension is comparable to hypocenter location error and this raises the uncertainty of calculation of the obtained rupture velocity. On the other hand, the rupture dimension itself could change regarding the source-station configuration, and consequently, trade off with rupture velocity and rise time. The obtained final source models that had longer ruptures would necessarily evolve faster to provide almost the same well-resolved rupture duration.

The 2009 rupture models occur on an average geometry of strike/dip=152°/ 48° on the Southeastern part of Cf. The slips are distributed from depths of 5 km to 10 km. The ruptures mostly evolve up-dip and toward the Southeast. A cumulative scalar seismic moment of 1.7*10^17 Nm obtained for these events which is 45% less than total co and post-seismic cumulative strain release obtained by Cheloni et al., (2014) using geodetic data (3.17*10^17

Nm). This confirms that 45% of the deformation has released aseismic on this part of the fault.

The 2017 source models occur on an average geometry of strike/dip =161°/35° on Northwest part of Cf. The slips are distributed from depths of 2 km to 10 km. The ruptures mostly evolve up dip and toward the Northwest. The cumulative scalar seismic moment of these events is estimated 5.87 *10^17 Nm, 35% less than total co and post-seismic cumulative strain release of 9.29*10^17 Nm obtained by Cheloni et al., (2019) using geodetic and near-field data. This confirms that 35% of the deformation has released aseismic on this part of the fault.

The ruptures of two main events of January 18th 2017 with magnitudes M5.5 and M5.4 on the Northwestern part of Cf (Eq#6 & Eq#7 in Table A1) are also studied by Cheloni et al., (2019) using geodetic and near-field data. For the M5.5 event, we obtain a geometry with strike/dip of 161°/41°. The rupture starts at depth of ~8km and evolves mostly up-dip and toward the northwest until reaches to the depth of ~2km. It releases a total scalar seismic moment of ~2.78*10^17 Nm that is close to Cheloni et al., (2019) result (2.81*10^17 Nm). Also, our obtained maximum slip areas for this event mostly matches to Cheloni et al., (2019) result. However, the rake value is obtained 69° which is less than their result (~90°).

Our obtained source model for the M5.4 event show the start of rupture from the depth of 9.4 km and it evolve fully up-dip with two main patches centered at depths of 8 km and 6 km. However, Cheloni et al., (2019) obtained model for this event has also two patches: a big one at the shallow depth of ~6.5 km but a small one at deep areas centered at the depth of ~11.5 km (~2 km beneath their used hypocenter at 9.71 km). We obtain a maximum slip and scalar seismic moment of 34 cm and 1.86*10^17 Nm, respectively, which are close to Cheloni et al., (2019) results (35 cm and 1.76*10^17 Nm, respectively).

To sum up, the Cf has 13° steeper dip on its Southeast part compared to the Northwest part. Some areas on Cf did not rupture during the 2009 and 2017 sequences and can be potential areas for future events. However, we do not reject the possibility that future events rupture on previously slipped areas of this fault.

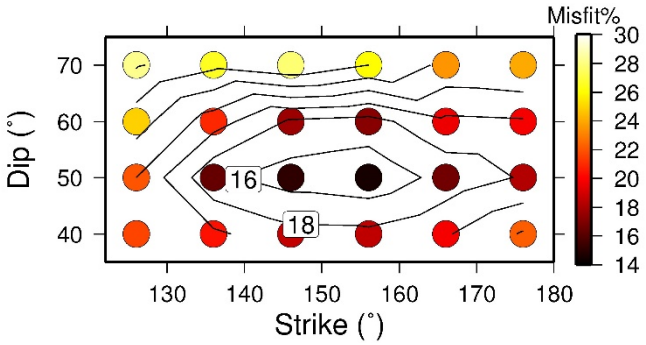

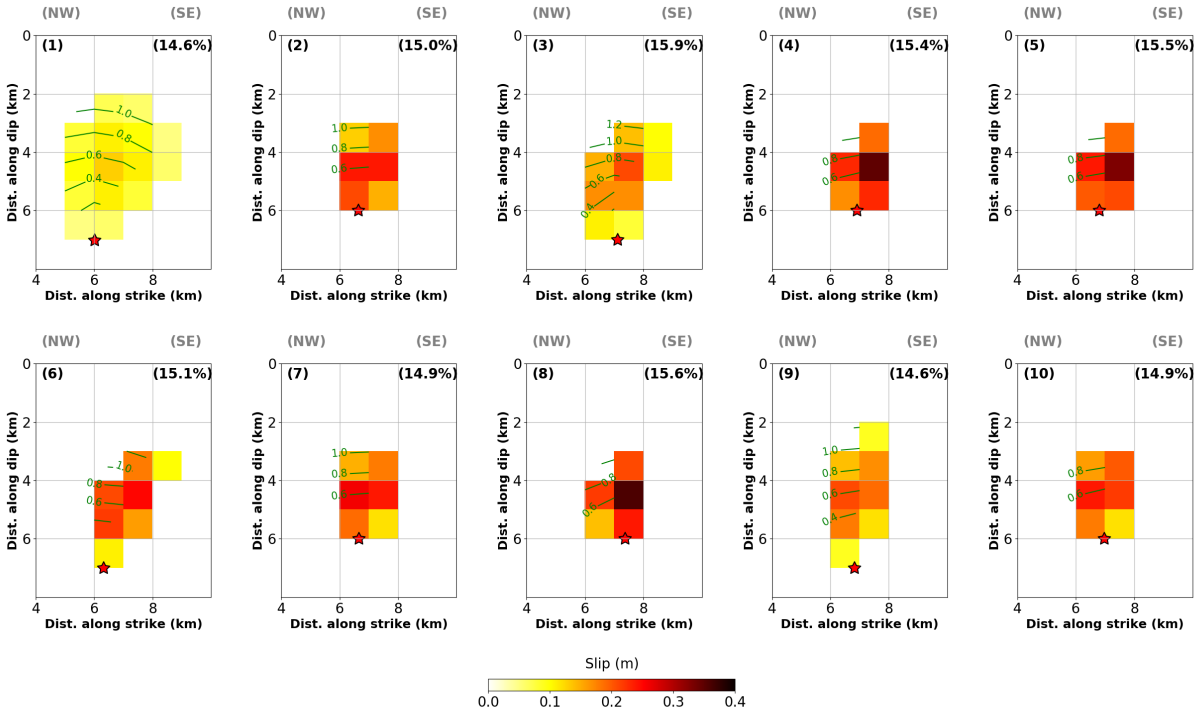
(NW)
(SE)
(1)
(14.6%)
(2)
(15.0%)
(3)
(15.9%)
(4)
(15.4%)
(5)
(15.5%)
(6)
(15.1%)
(7)
(14.9%)
(8)
(15.6%)
(9)
(14.6%)
(10)
(14.9%)
Dist. along dip (km)
Dist. along strike (km)
Slip (m)
0.0
0.1
0.2
0.3
0.4

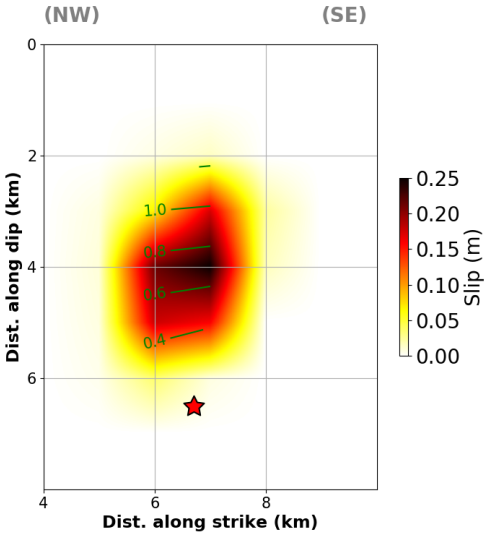
(NW)
(SE)
Dist. along dip (km)
Dist. along strike (km)
Slip (m)
0.25
0.20
0.15
0.10
0.05
0.00

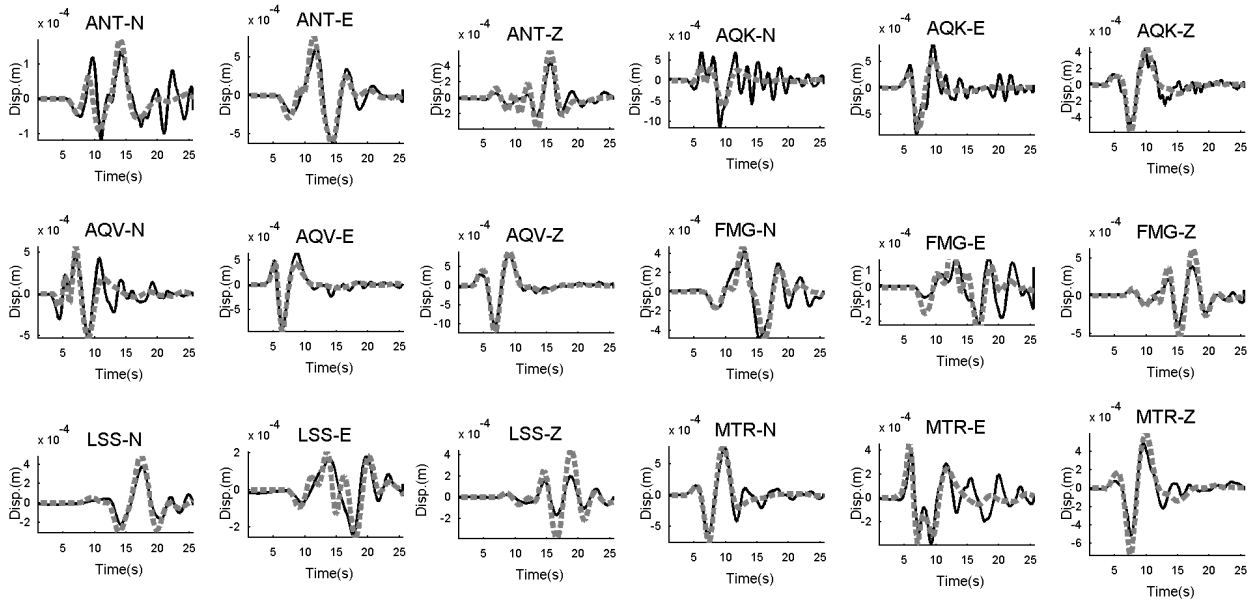

Figure A1. a) Diagram showing the misfits provided by the final source models that are obtained on trial planar geometries for the 2009/04/06 M5 23:15:37 (GMT) event. The preferred geometry has a minimum misfit of 14.5%. **b)** 10 final source models for this event obtained on the preferred geometry with strike/dip of (156/50). **c)** the best averaged model for this event. **d)** the waveform fit of the preferred model shown in (c). The black solid and dotted lines are real and synthetics, respectively.

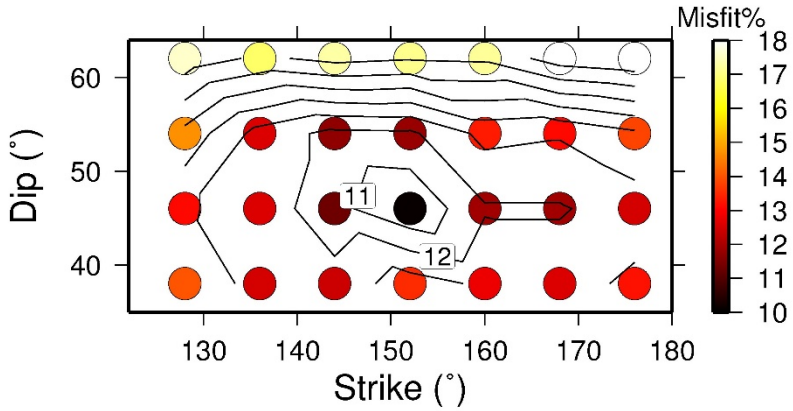

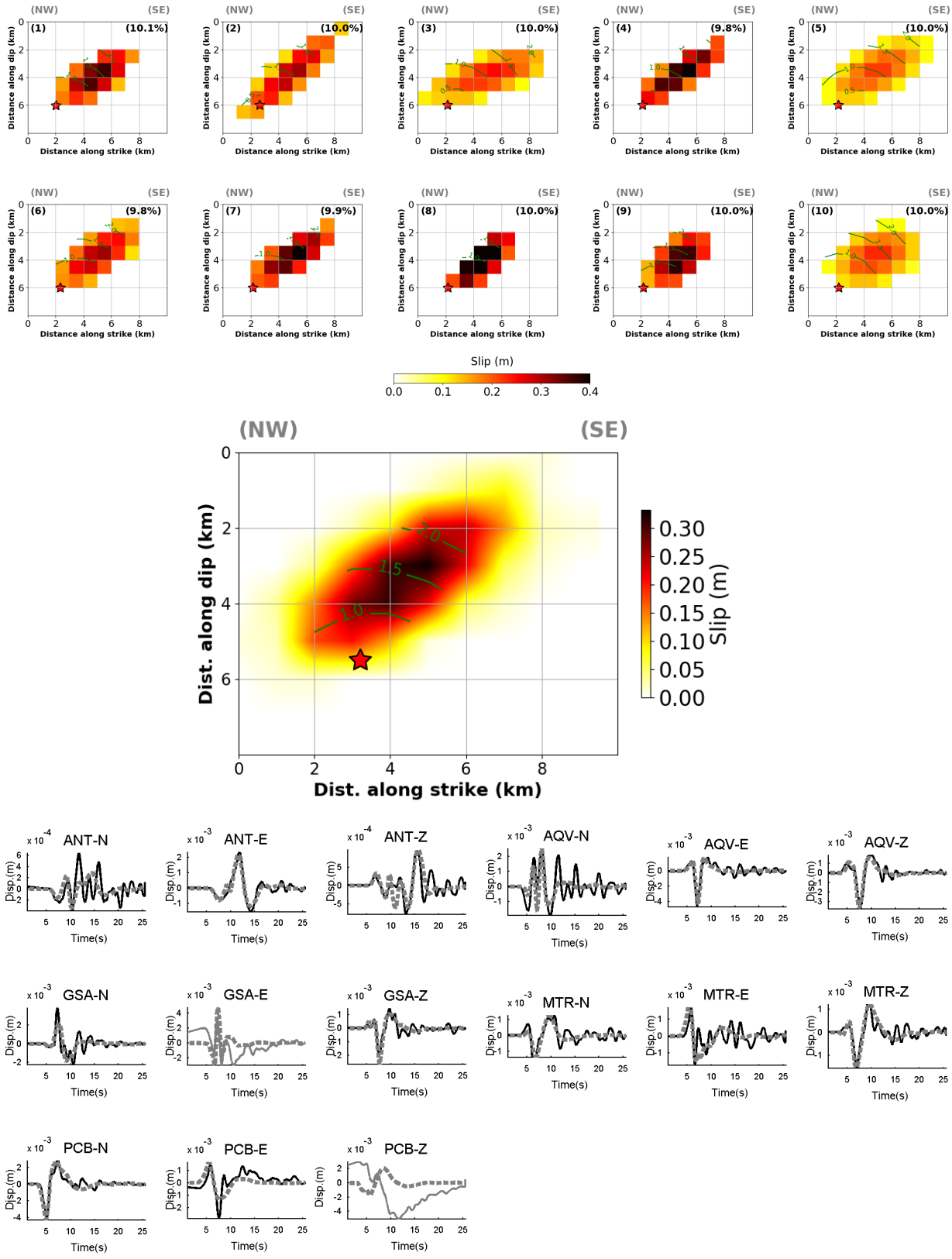

Figure A2. a) Diagram showing the tested geometries for the 2009/04/06 M5.2 00:53:00 (GMT) event. The preferred geometry has a minimum misfit of 10.1%. **b)** 10 final source models for this event obtained on the preferred geometry with strike/dip of (152°/46°). **c)** The best averaged model for this event. **d)** The waveform fit of the preferred source model shown in (c). The black solid and dotted lines are real and synthetics, respectively. The components

shown in grey solid lines (GSA-E, PCB-Z) did not use in the inversion, while the synthetics are produced for them by forward modelling.

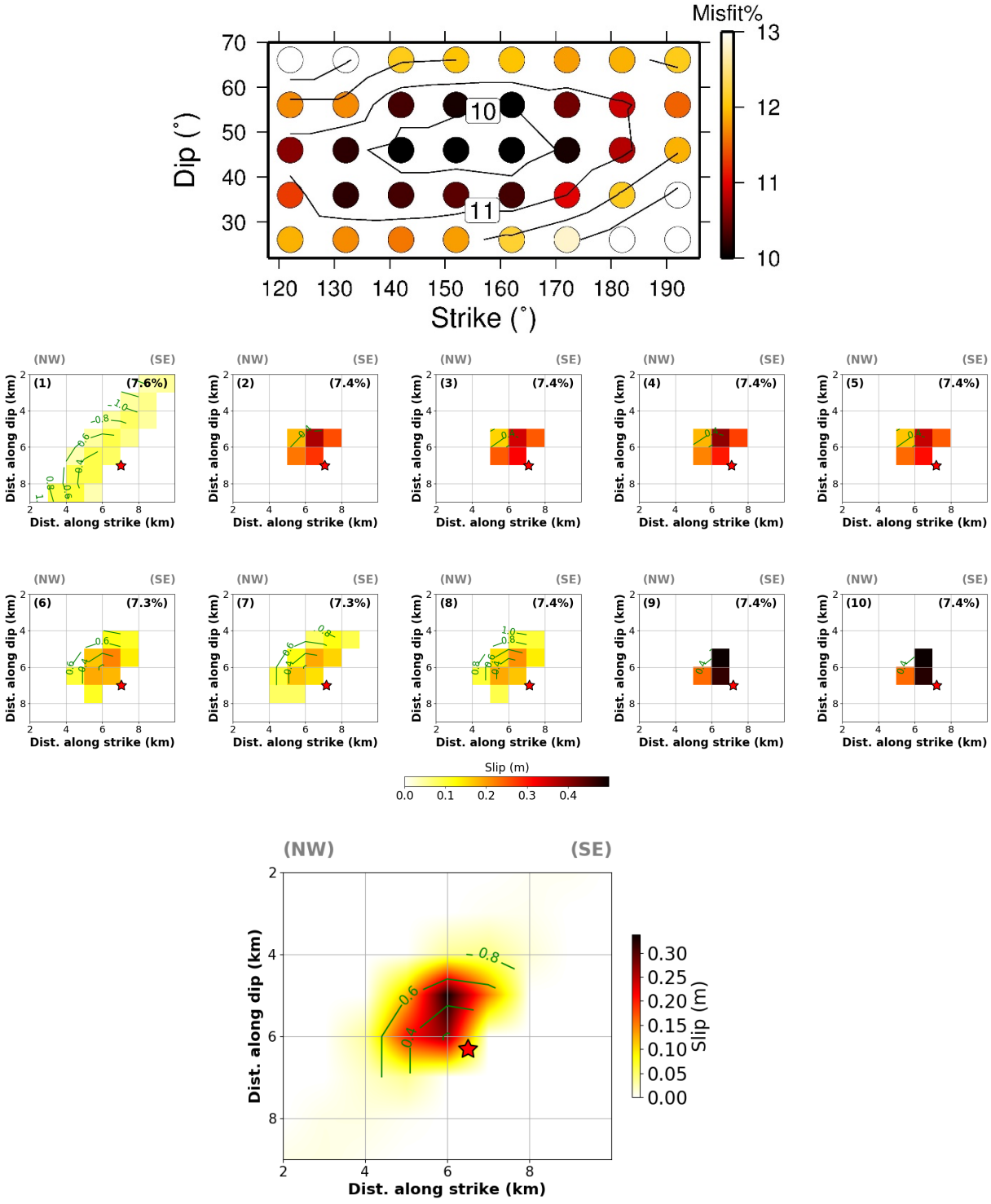

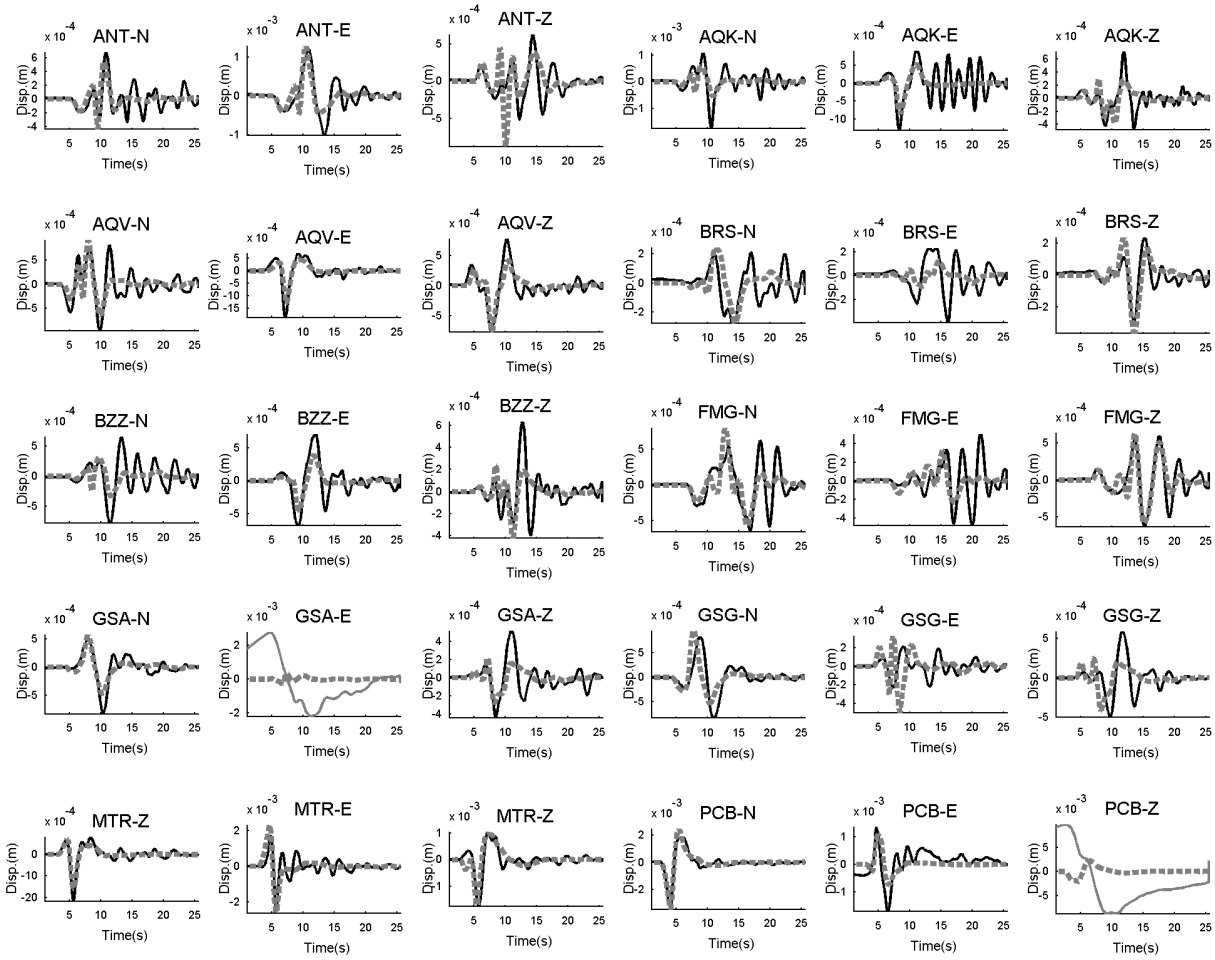

Figure A3. a) Diagram showing the tested geometries for the 2009/04/09 M5.0 19:38:17 (GMT) event. The preferred geometry has a minimum misfit of 7.4%. **b)** 10 final source models for this event obtained on the preferred geometry with strike/dip of (147°/48°). **c)** The best averaged model for this event. **d)** The waveform fit of the preferred model shown in (c). The black solid and dotted lines are real and synthetics, respectively. The components shown in grey solid lines (GSA-E, PCB-Z) did not use in the inversion, while the synthetics are produced for them by forward modelling.

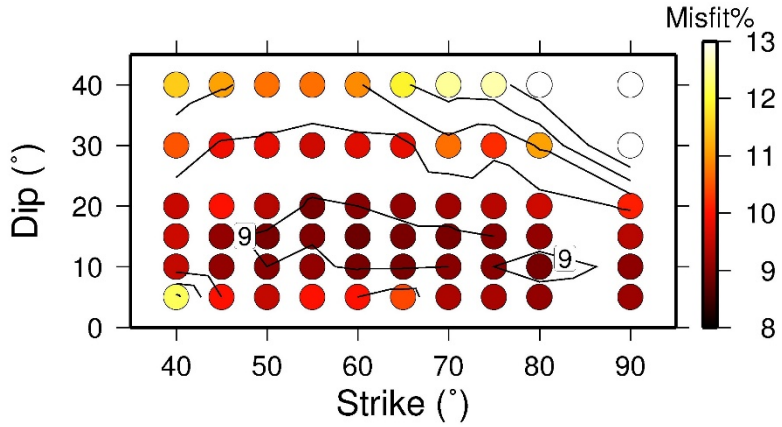

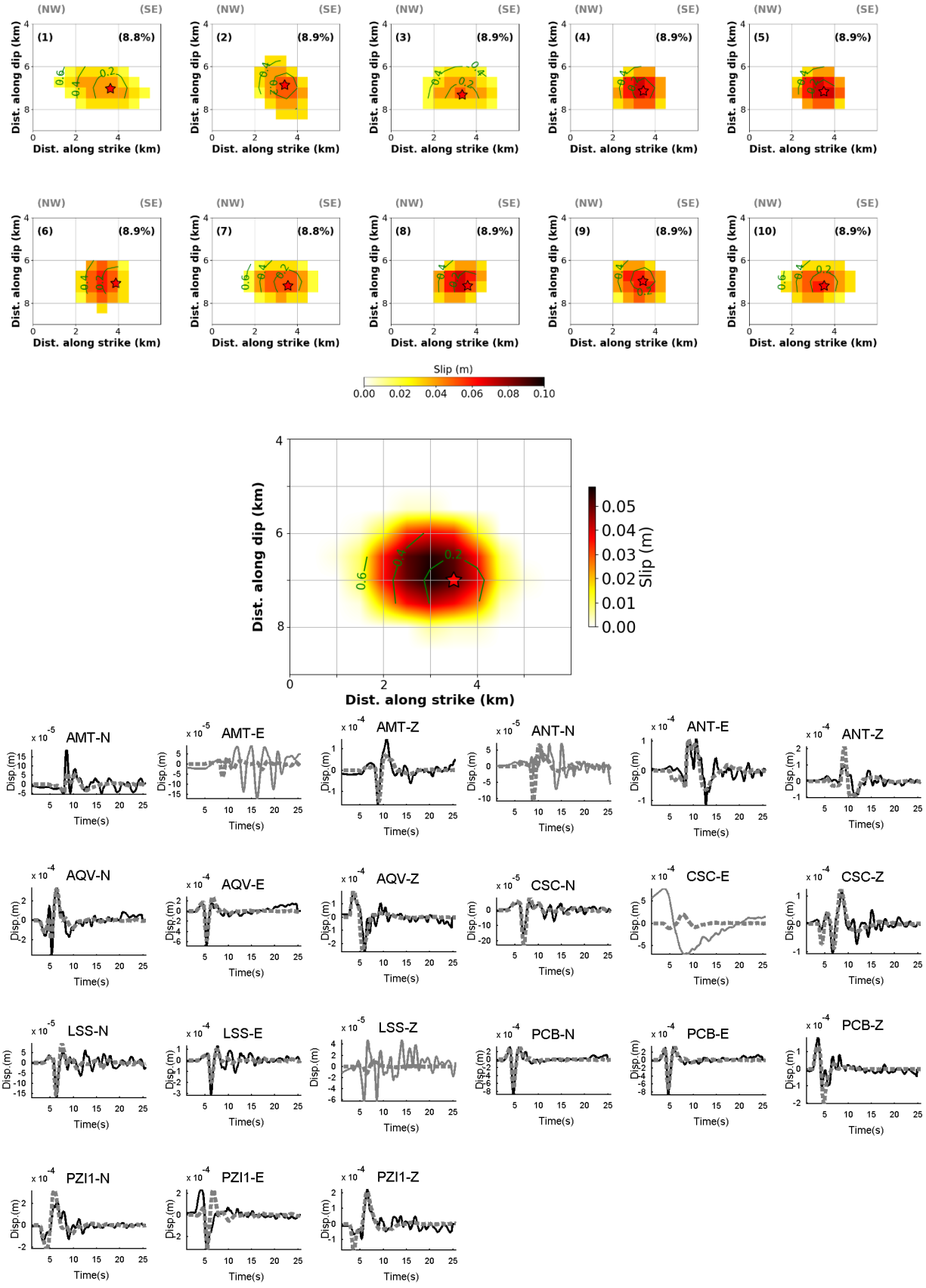

Figure A4. a) Diagram showing the tested geometries for the 2009/06/22 M4.4 20:58:40 (GMT) decollement event. The preferred geometry has a minimum misfit of 8.8%. **b)** 10 final source models for this event obtained on the preferred geometry with strike/dip of (60°/15°).

c) The best averaged model for this event. **d)** The waveform fit of the preferred model shown in (c). The black solid and dotted lines are real and synthetics, respectively. The components for which the waves are shown in grey solid lines (AMT-E, ANT-N, CSC-E, LSS-Z) did not use in the inversion, while the synthetics are produced for them by forward modelling.

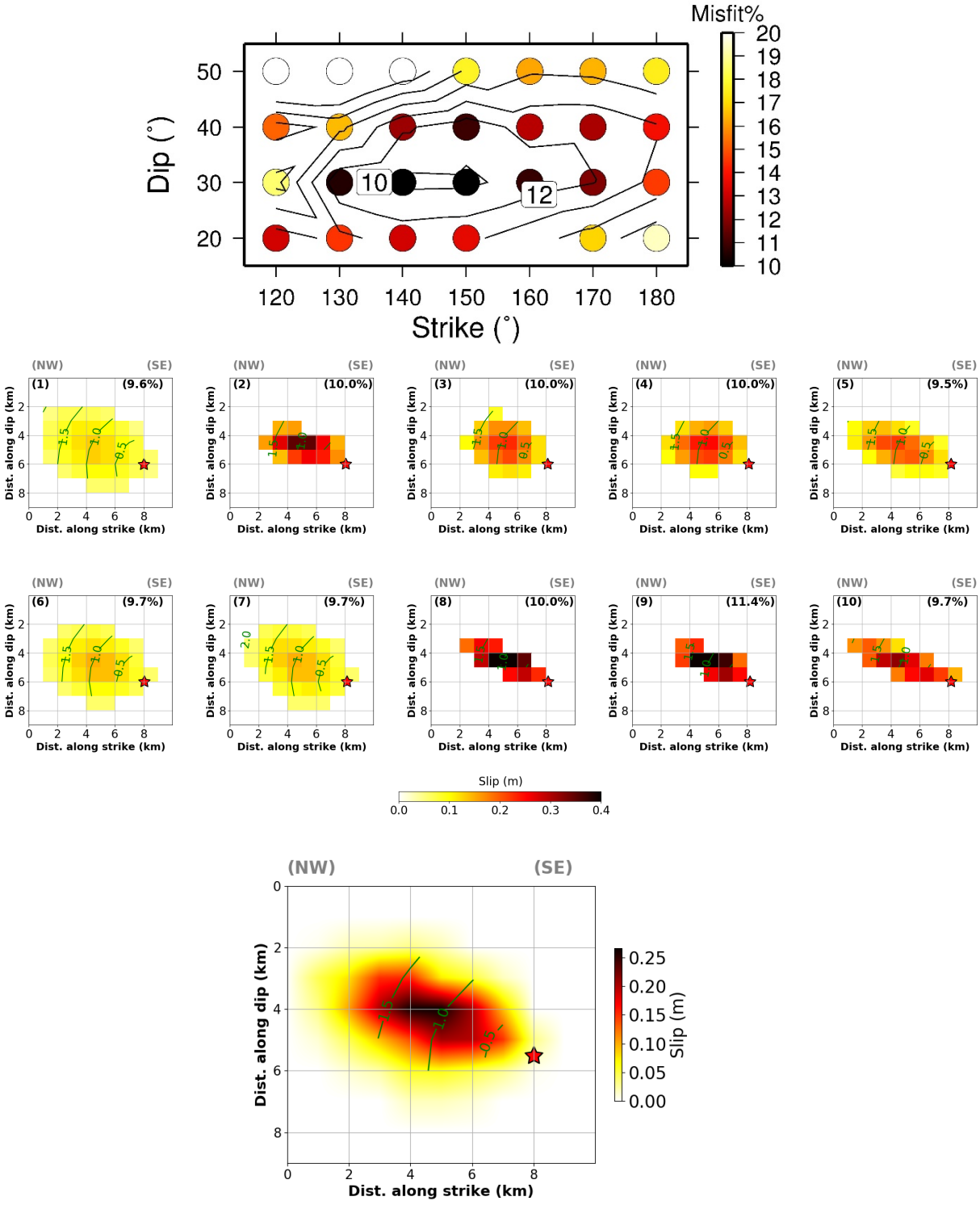

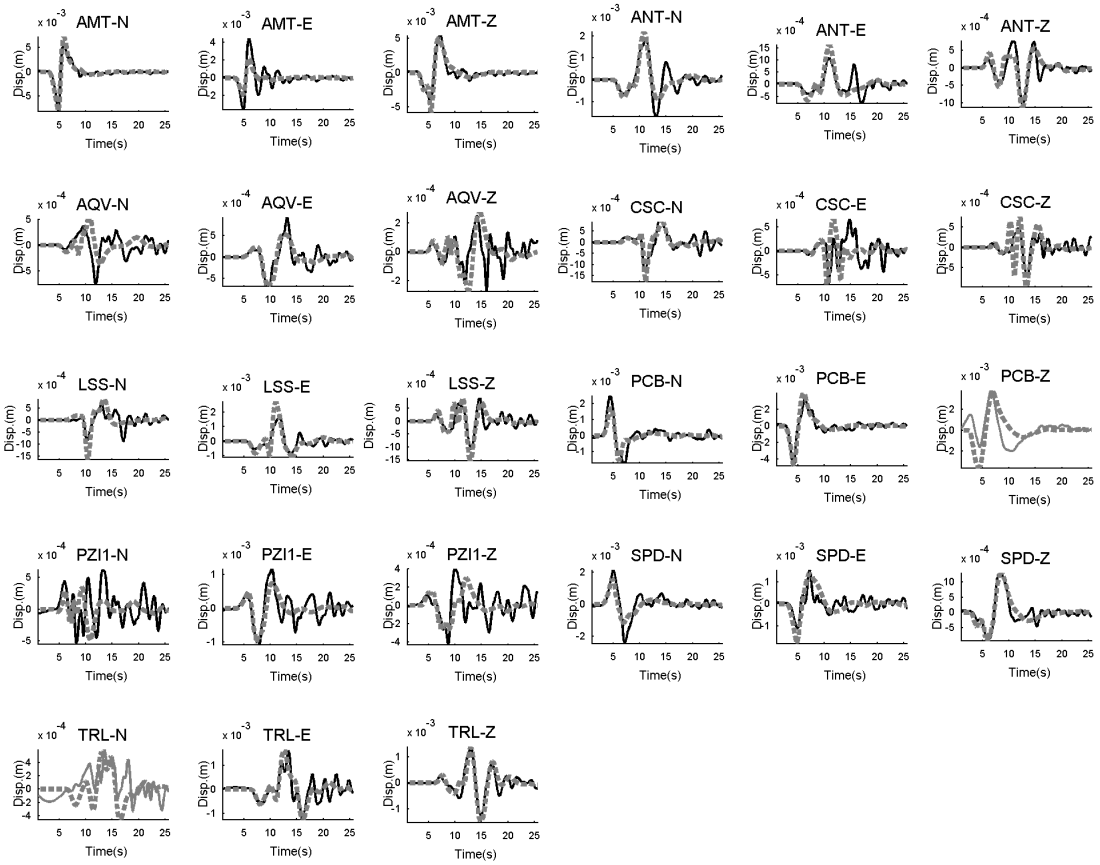

Figure A5. a) Diagram showing the tested geometries for the 2017/01/18 M5.4 09:25:40 (GMT) event. The preferred geometry has a minimum misfit of 9.5%. **b)** 10 final source models for this event obtained on the preferred geometry with strike/dip of 150°/30°. **c)** The best averaged model for this event. **d)** The waveform fit of the preferred model shown in (c). The black solid and dotted lines are real and synthetics, respectively. The components for which the waves are shown in grey solid lines (PCB-Z, TRL-N) did not use in the inversion, while the synthetics are produced for them by forward modelling.

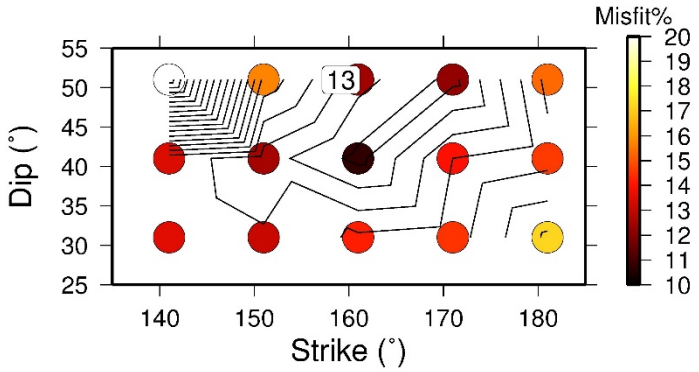

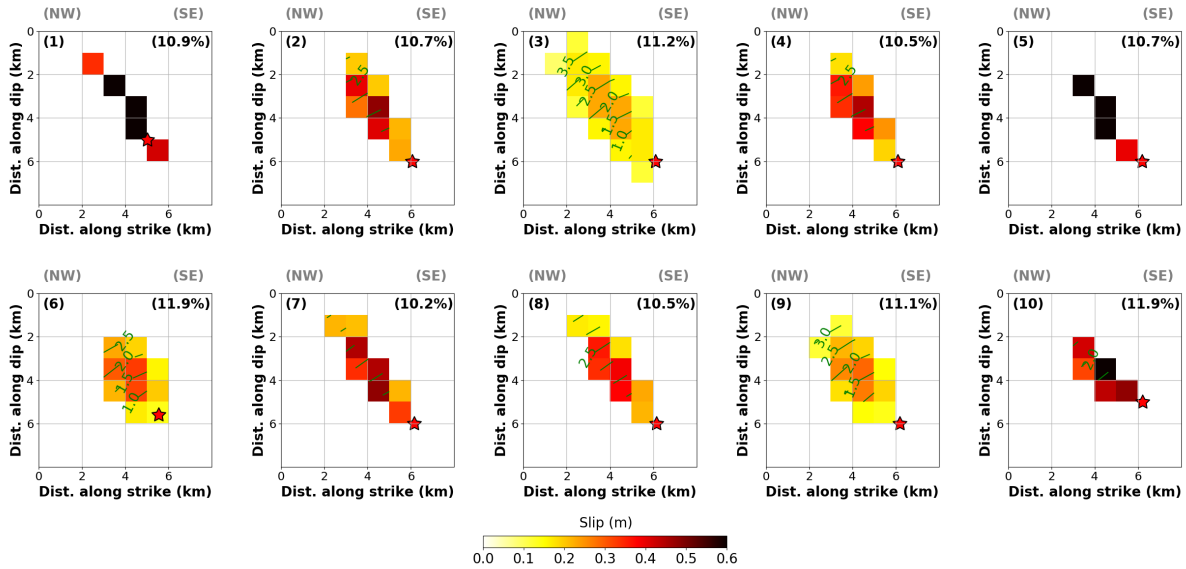
(NW)
(SE)
(1)
(10.9%)
(2)
(10.7%)
(3)
(11.2%)
(4)
(10.5%)
(5)
(10.7%)
(6)
(11.9%)
(7)
(10.2%)
(8)
(10.5%)
(9)
(11.1%)
(10)
(11.9%)
Dist. along dip (km)
Dist. along strike (km)
Slip (m)
0.0 0.1 0.2 0.3 0.4 0.5 0.6

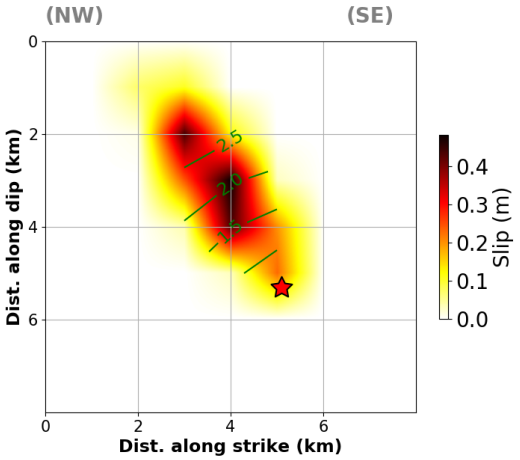
(NW)
(SE)
Dist. along dip (km)
Dist. along strike (km)
Slip (m)
0.0
0.1
0.2
0.3
0.4

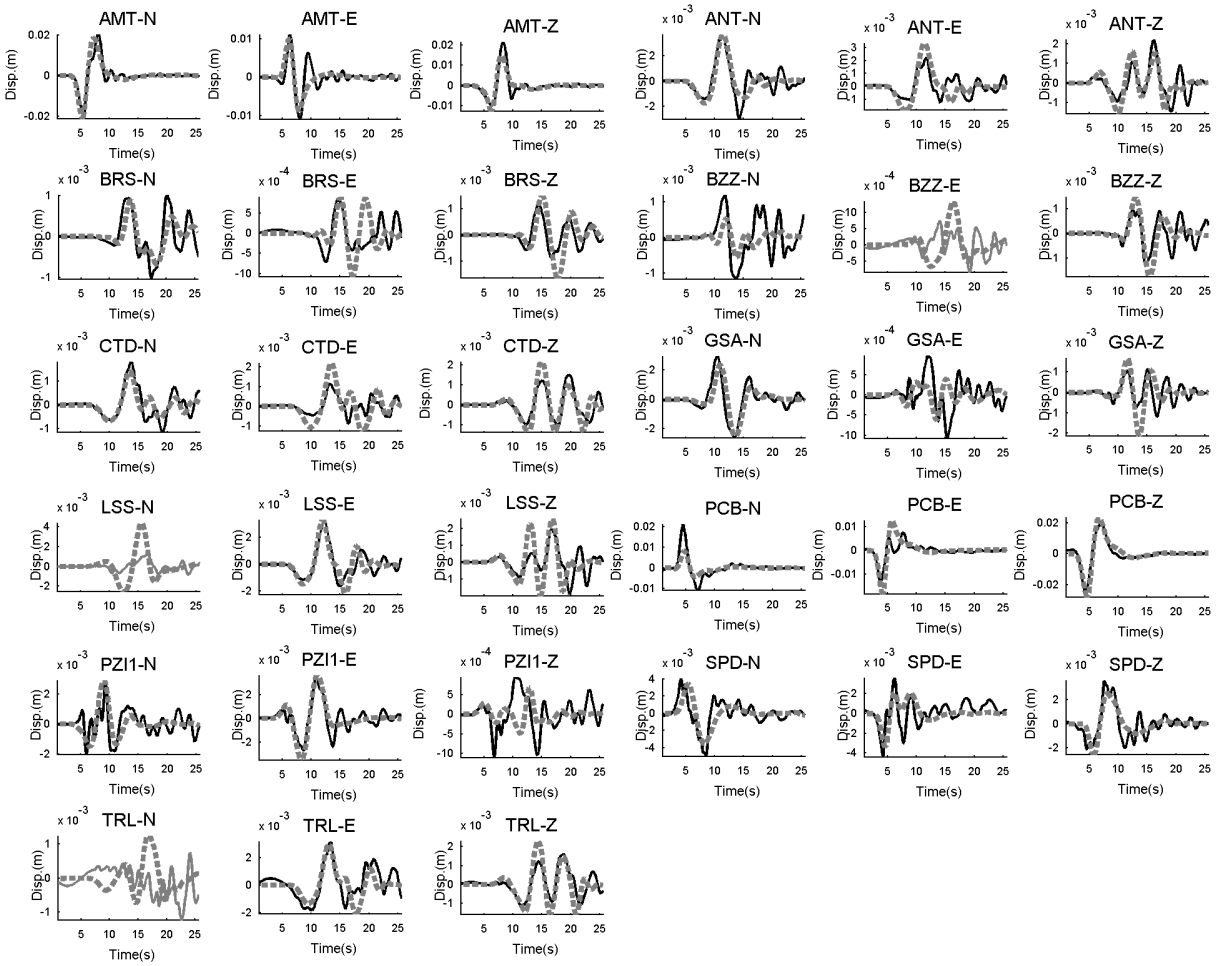

Figure A6. a) Diagram showing the tested geometries for the 2017/01/18 M5.5 10:14:10 (GMT) event. The preferred geometry has a minimum misfit of 10%. **b)** 10 final source models for this event obtained on the preferred geometry with strike/dip of 161°/41°. **c)** the best averaged model for this event. **d)** the waveform fit of the preferred model shown in (c). The black solid and dotted lines are real and synthetics, respectively. The components for which the waves are shown in grey solid lines (BZZ-E, LSS-N, TRL-N) did not use in the inversion, while the synthetics are produced for them by forward modelling.

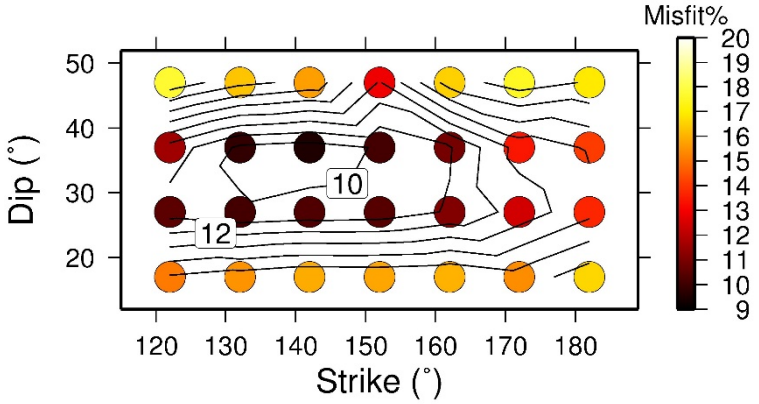

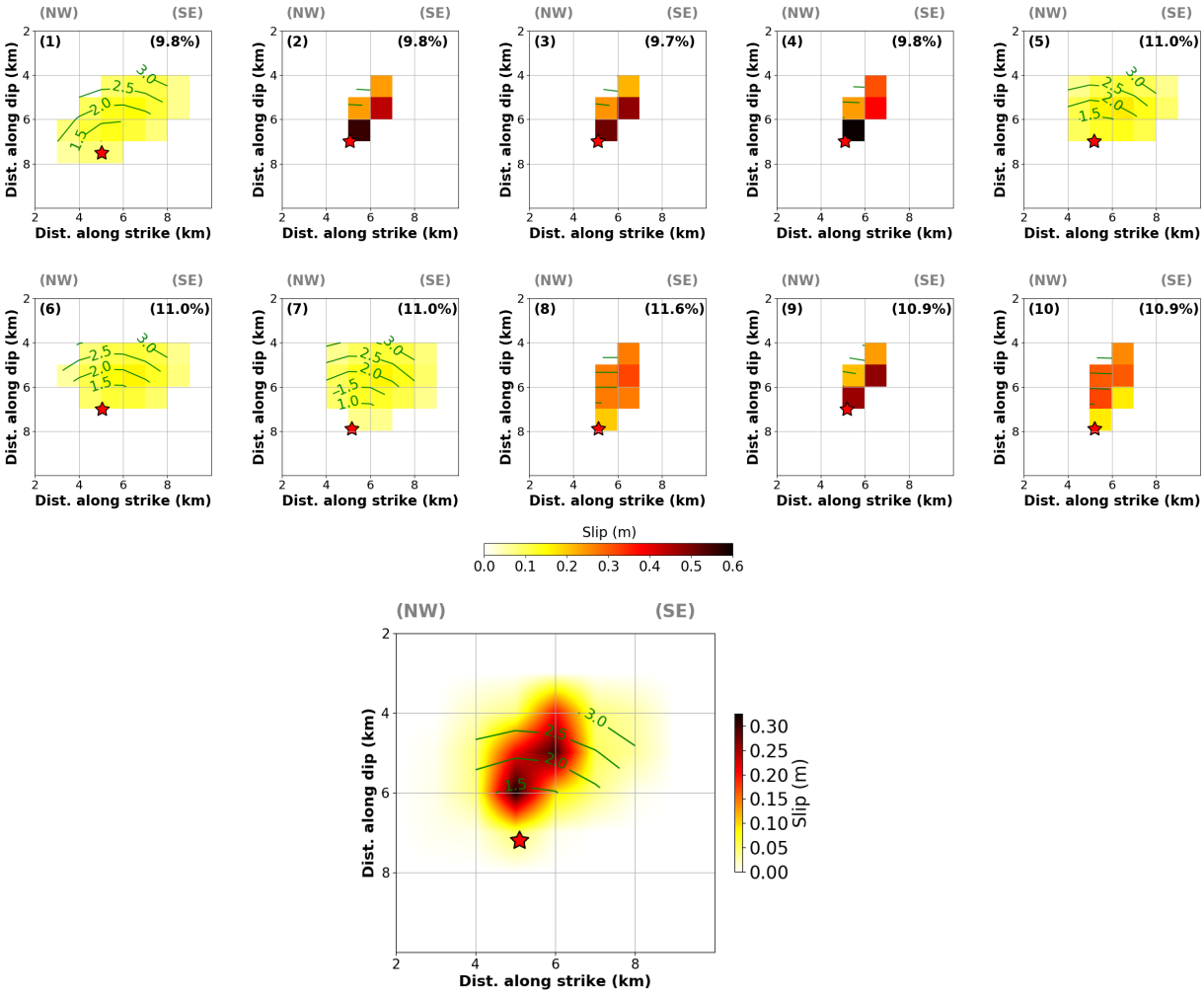
(NW)
(SE)
(1)
(9.8%)
(2)
(9.8%)
(3)
(9.7%)
(4)
(9.8%)
(5)
(11.0%)
(6)
(11.0%)
(7)
(11.0%)
(8)
(11.6%)
(9)
(10.9%)
(10)
(10.9%)
Dist. along dip (km)
Dist. along strike (km)
Slip (m)
0.0 0.1 0.2 0.3 0.4 0.5 0.6

(NW)
(SE)
Dist. along dip (km)
Dist. along strike (km)
Slip (m)
0.30
0.25
0.20
0.15
0.10
0.05
0.00

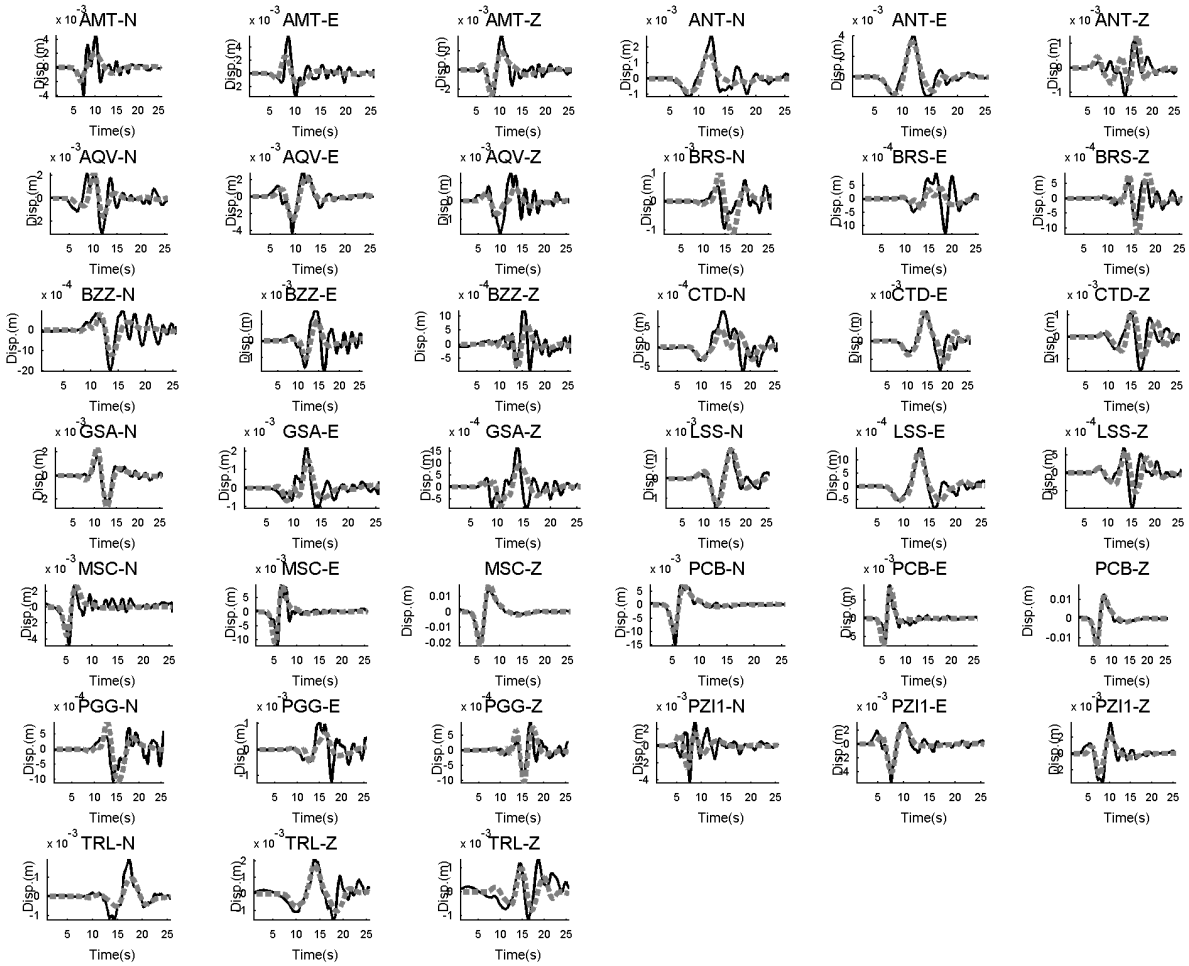

Figure A7. a) Diagram showing the tested geometries for the 2017/01/18 M5.4 10:25:24 (GMT) event. The preferred geometry has a minimum misfit of 9.5%. **b)** 10 final source models for this event obtained on the preferred geometry with strike/dip of 142°/37°. **c)** the best averaged model for this event. **d)** the waveform fit of the preferred model shown in (c). The black solid and dotted lines are real and synthetics, respectively.

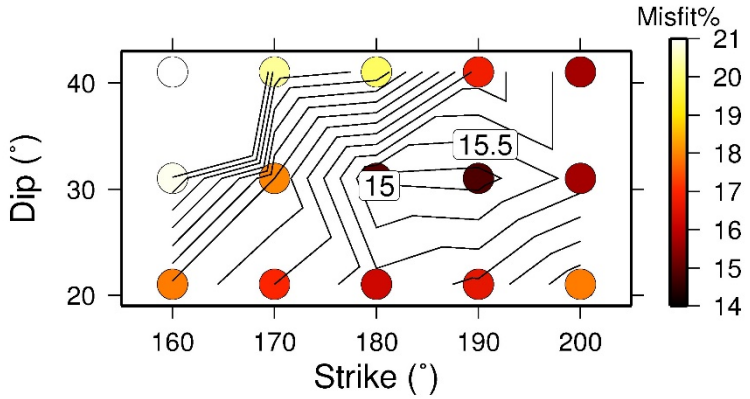

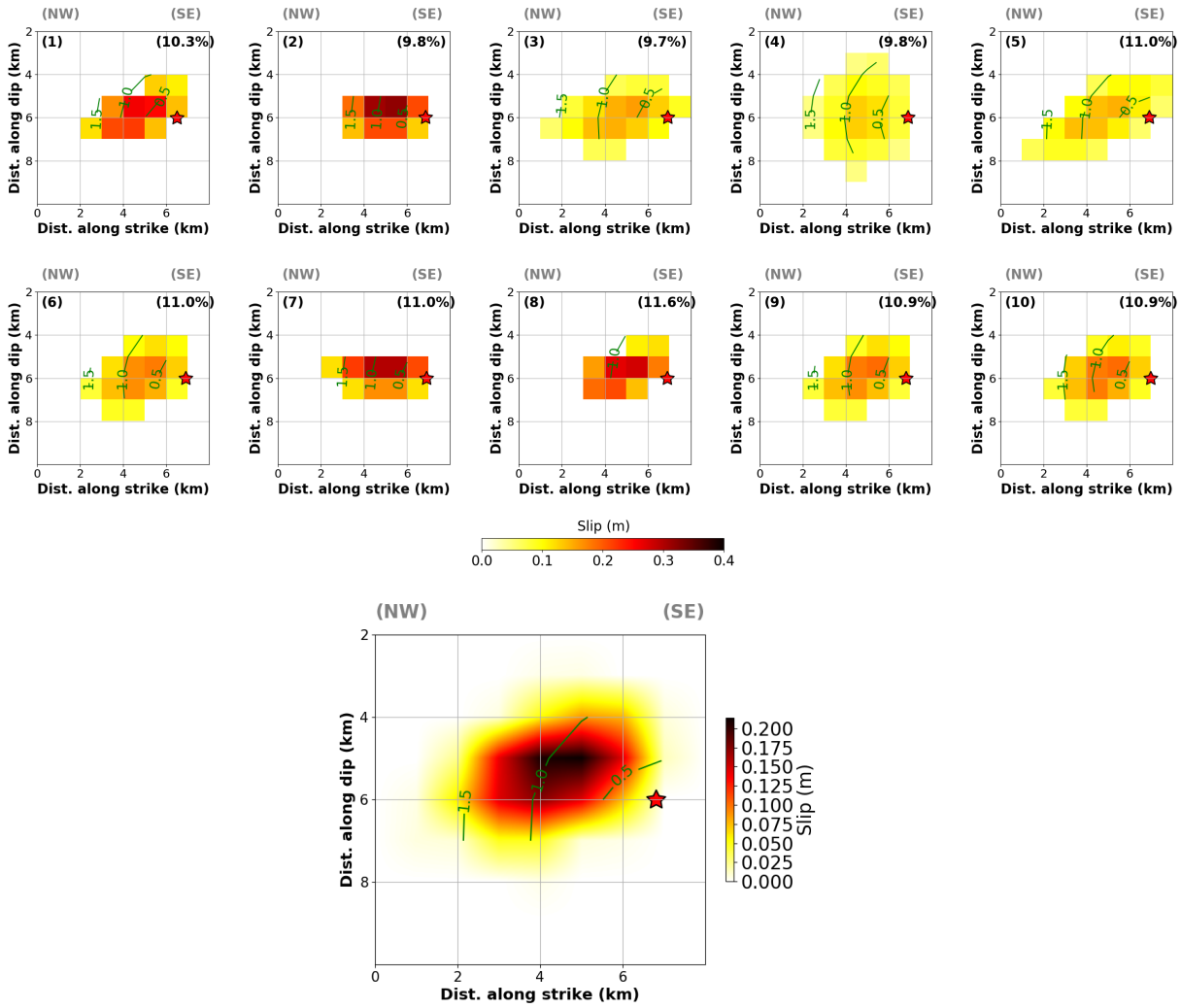
(NW)
(SE)
(1)
(10.3%)
(2)
(9.8%)
(3)
(9.7%)
(4)
(9.8%)
(5)
(11.0%)
(6)
(11.0%)
(7)
(11.0%)
(8)
(11.6%)
(9)
(10.9%)
(10)
(10.9%)
Dist. along dip (km)
Dist. along strike (km)
1.5
1.0
0.5
Slip (m)
0.0
0.1
0.2
0.3
0.4

(NW)
(SE)
Dist. along dip (km)
Dist. along strike (km)
1.5
1.0
0.5
0.200
0.175
0.150
0.125
0.100
0.075
0.050
0.025
0.000
Slip (m)

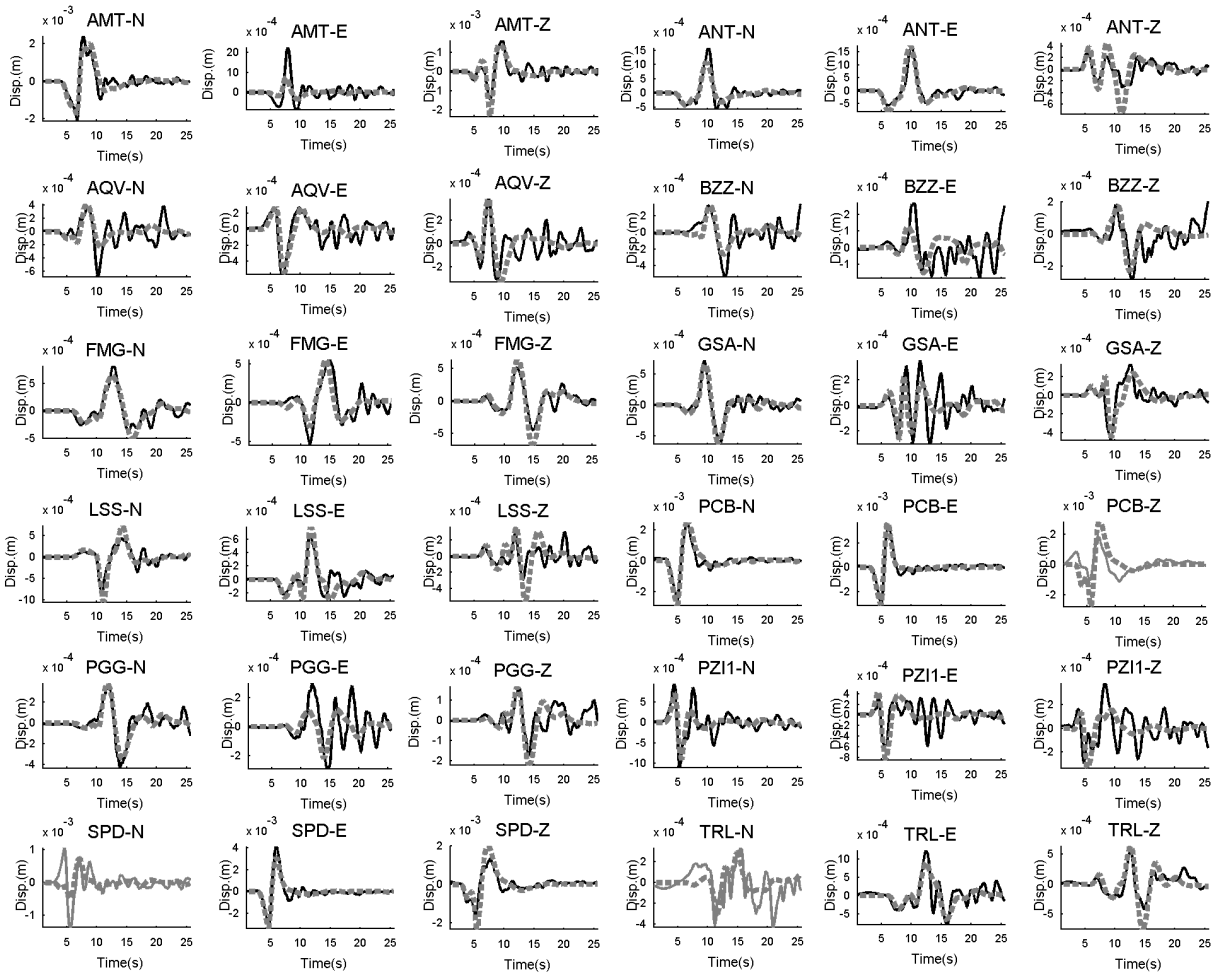

Figure A8. a) Diagram showing the tested geometries for the 2017/01/18 M5.1 13:33:37 (GMT) event. The preferred geometry has a minimum misfit of 14.8%. **b)** 10 final source models for this event obtained on the preferred geometry with strike/dip of 190°/31°. **c)** The best averaged source model for this event. **d)** the waveform fit of the preferred source model shown in (c). The black solid and dotted lines are real and synthetics, respectively. The components for which the waves are shown in grey solid lines (PCB-Z, SPD-N, TRL-N) did not use in the inversion, while the synthetics are produced for them by forward modelling.

Appendix-B. Inversion convergence

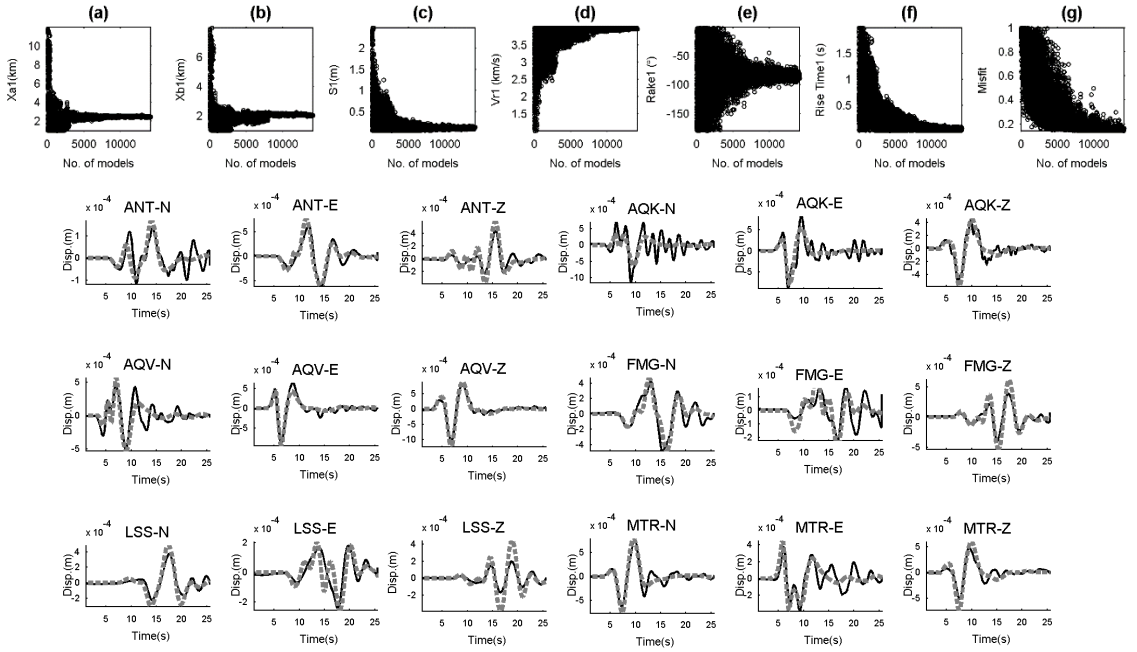

Figure Sb1. A) Convergence of model#1 source parameters obtained for the ML5.0 23:15:37 (GMT) event. b) Waveform fit for the model#1. Black and gray are real and synthetics, respectively.

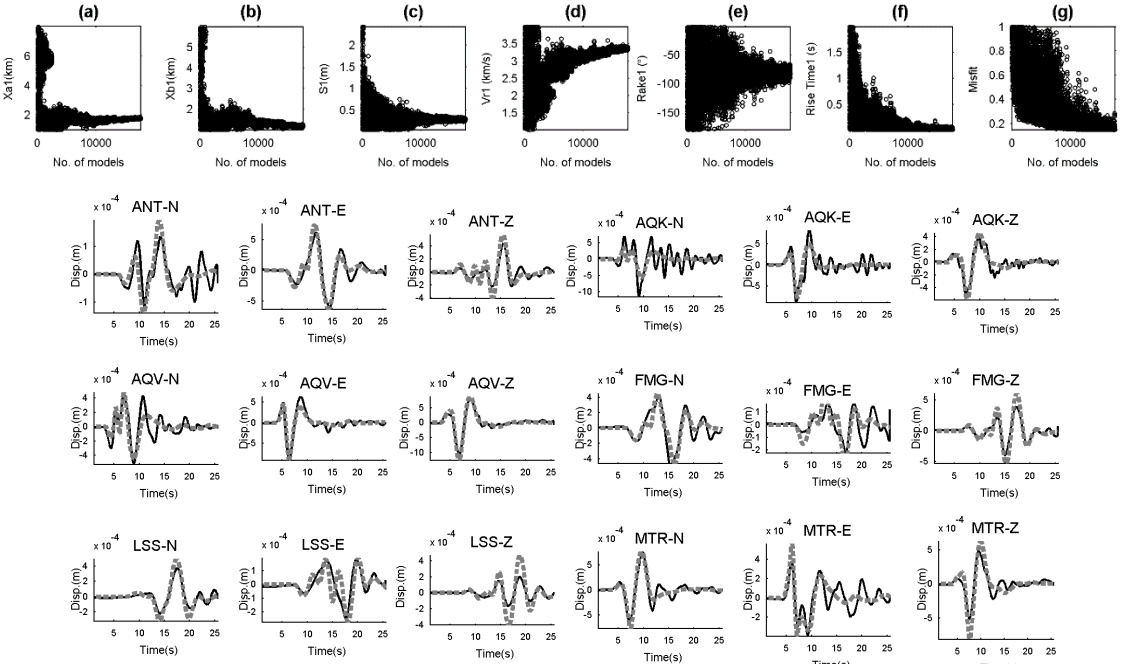

Figure Sb2. A) Convergence of model#2 source parameters obtained for the ML5.0 23:15:37 (GMT) event. b) Waveform fit for the model#2. Black and gray are real and synthetics, respectively.

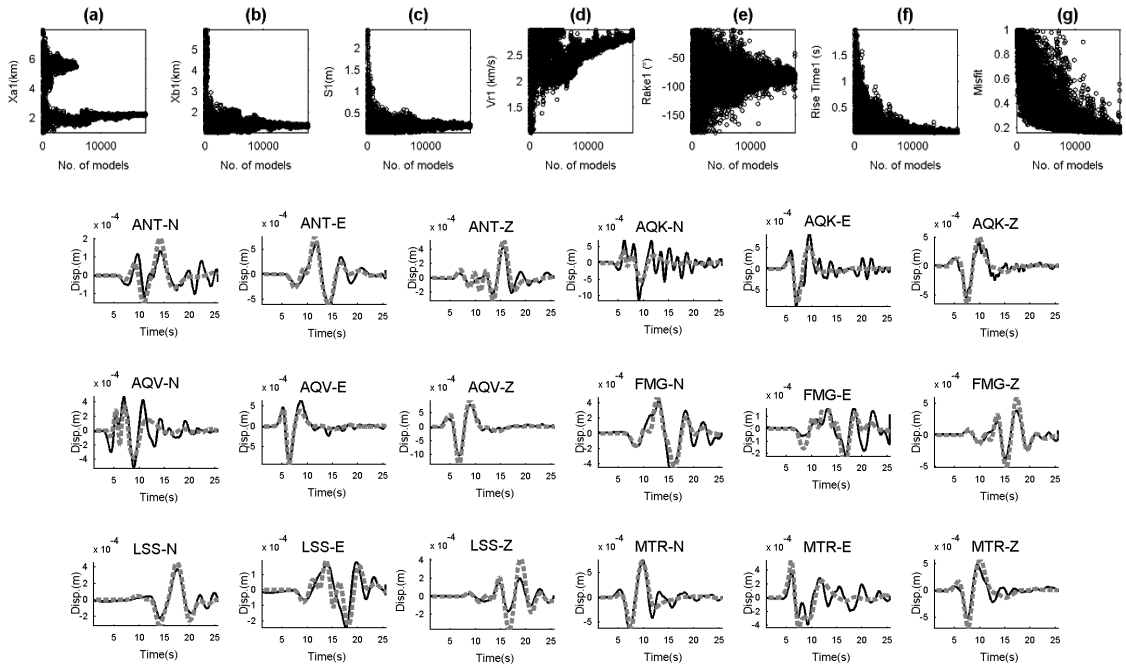

Figure Sb3. A) Convergence of model#3 source parameters obtained for the ML5.0 23:15:37 (GMT) event. b) Waveform fit for the model#3. Black and gray are real and synthetics, respectively.

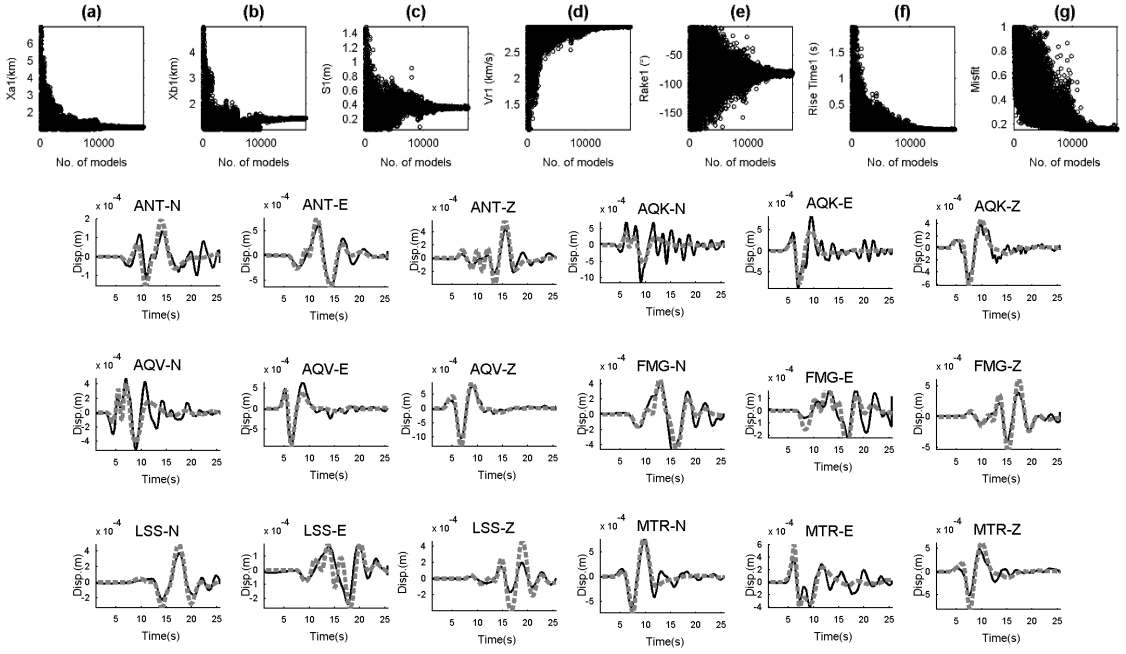

Figure Sb4. A) Convergence of model#4 source parameters obtained for the ML5.0 23:15:37 (GMT) event. b) Waveform fit for the model#4. Black and gray are real and synthetics, respectively.

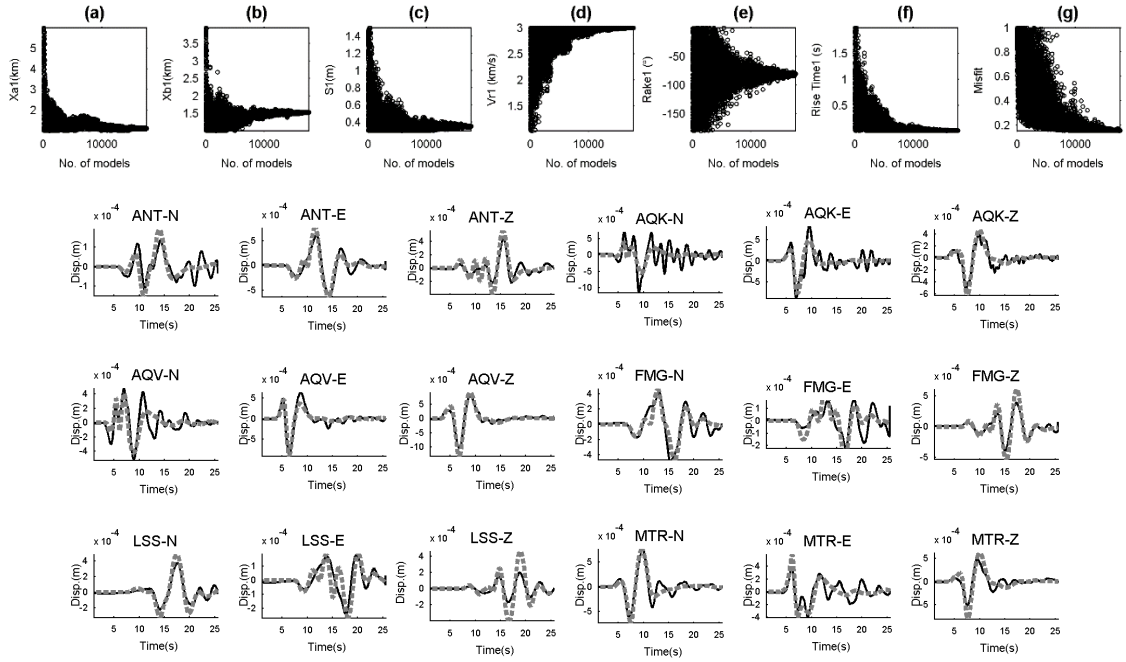

Figure Sb5. A) Convergence of model#5 source parameters obtained for the ML5.0 23:15:37 (GMT) event. b) Waveform fit for the model#5. Black and gray are real and synthetics, respectively.

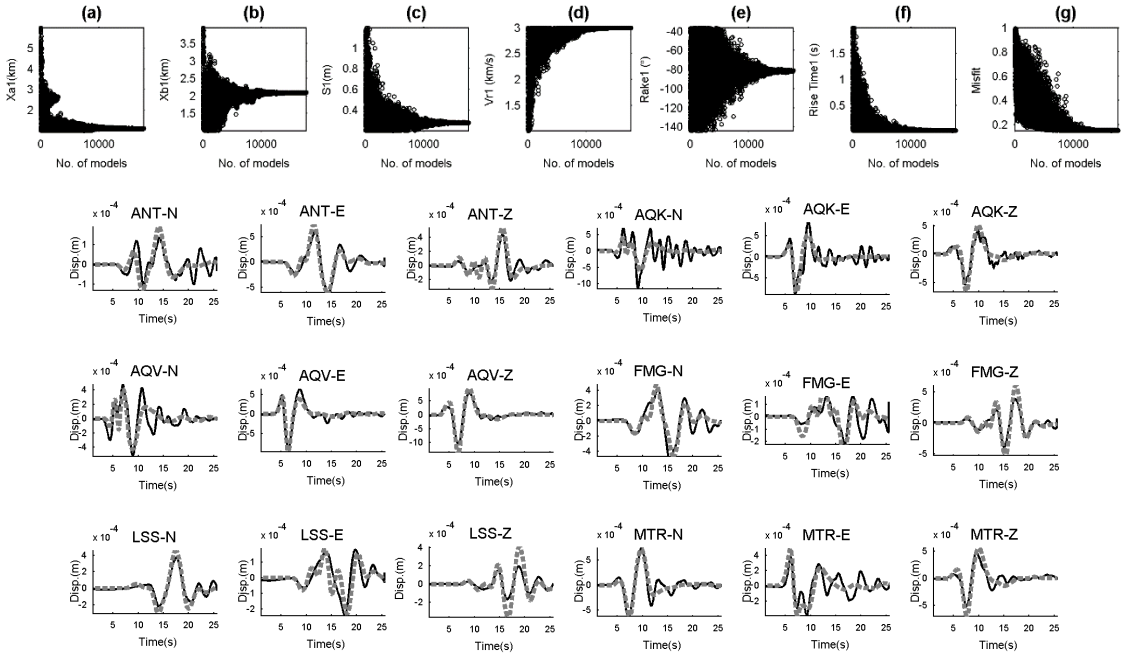

Figure Sb6. A) Convergence of model#6 source parameters obtained for the ML5.0 23:15:37 (GMT) event. b) Waveform fit for the model#6. Black and gray are real and synthetics, respectively.

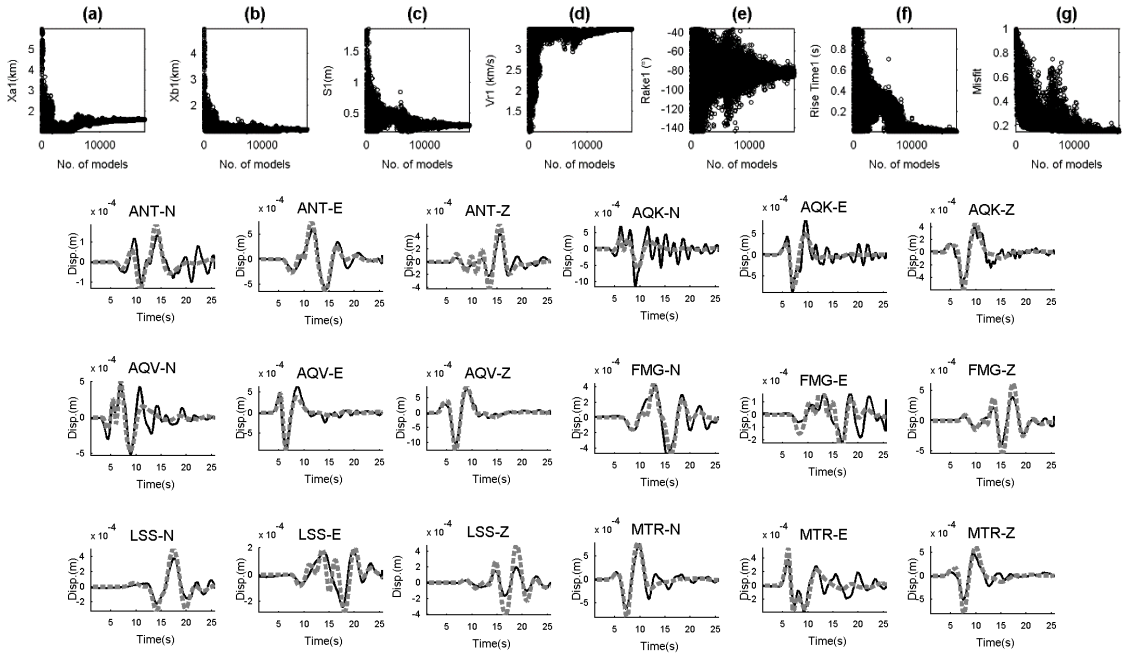

Figure Sb7. A) Convergence of model#7 source parameters obtained for the ML5.0 23:15:37 (GMT) event. b) Waveform fit for the model#7. Black and gray are real and synthetics, respectively.

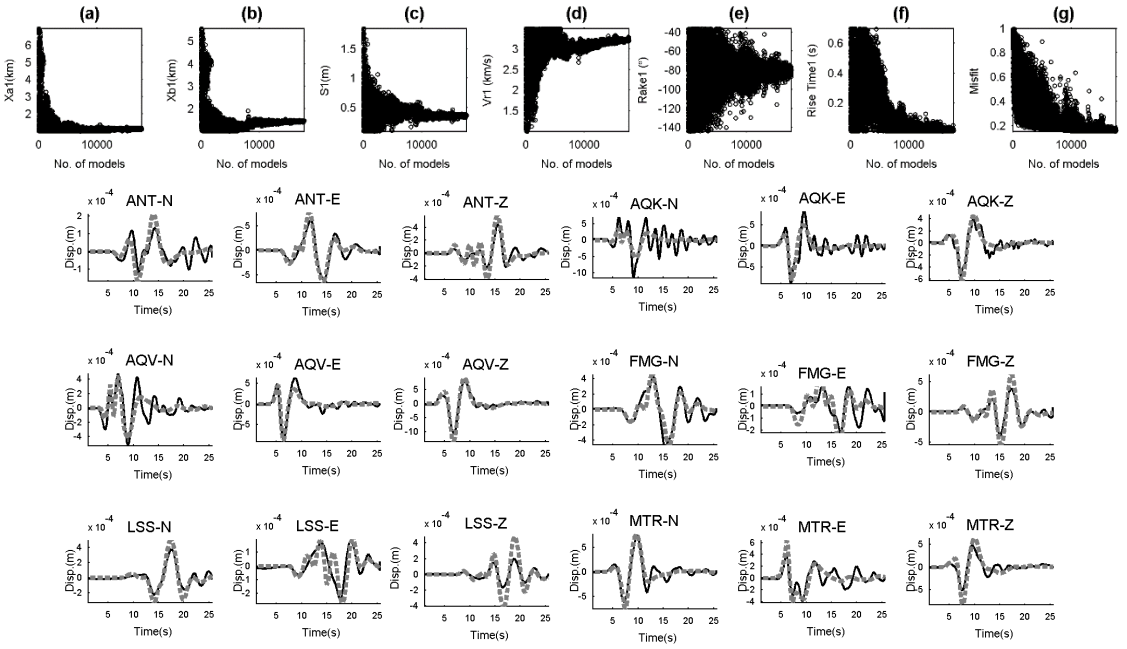

Figure Sb8. A) Convergence of model#8 source parameters obtained for the ML5.0 23:15:37 (GMT) event. b) Waveform fit for the model#8. Black and gray are real and synthetics, respectively.

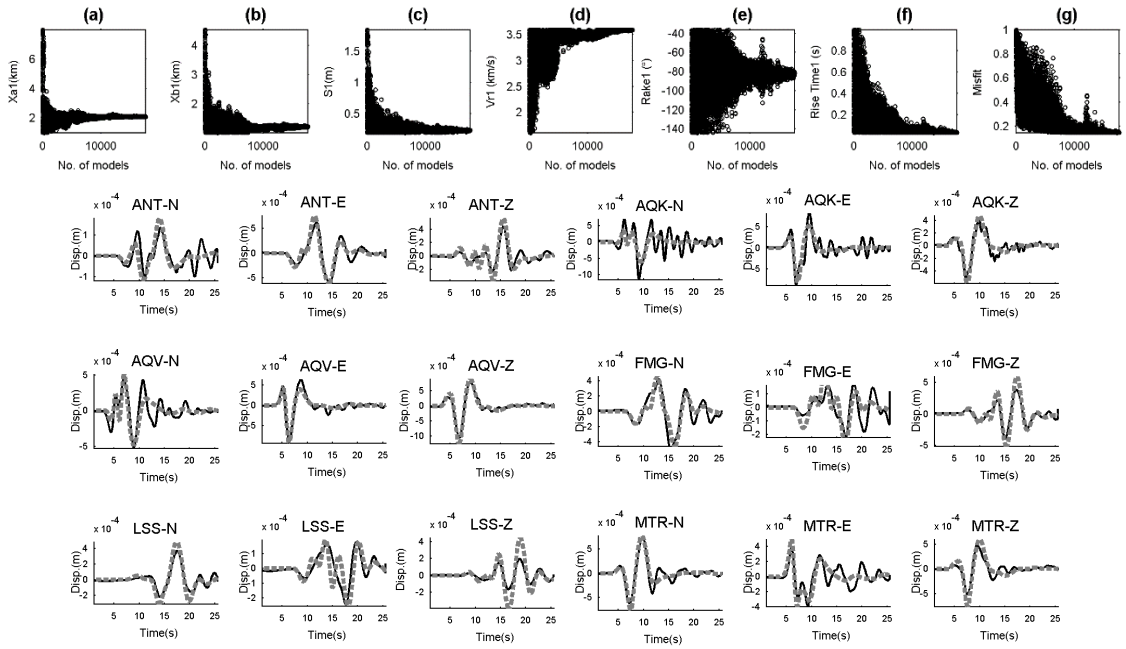

Figure Sb9. A) Convergence of model#9 source parameters obtained for the ML5.0 23:15:37 (GMT) event. b) Waveform fit for the model#9. Black and gray are real and synthetics, respectively.

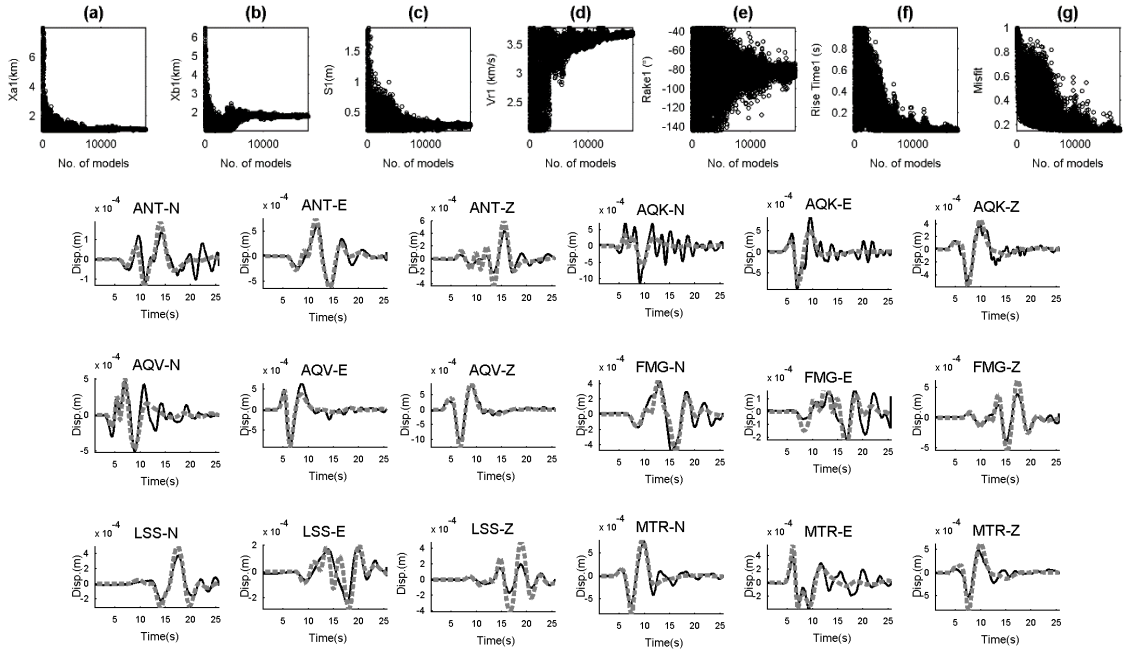

Figure Sb10. A) Convergence of model#10 source parameters obtained for the ML5.0 23:15:37 (GMT) event. b) Waveform fit for the model#10. Black and gray are real and synthetics, respectively.

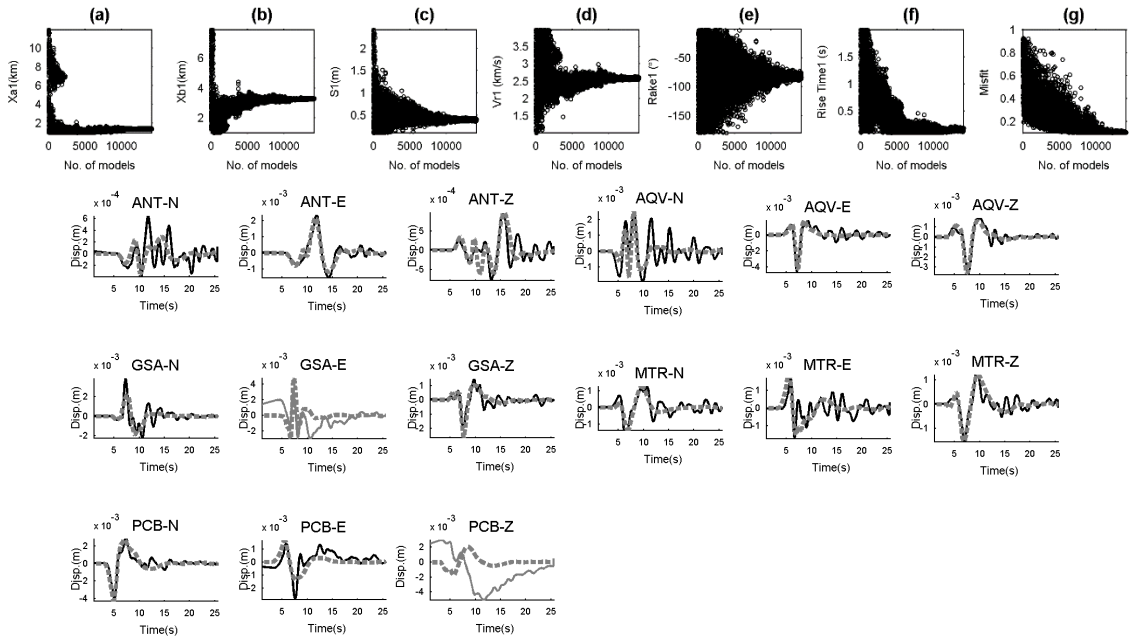

Figure Sb11. A) Convergence of model#1 source parameters obtained for the MW?? 00:52 event. b) Waveform fit for the model#1. Black and gray are real and synthetics, respectively. Gray solid lines did not use in the inversion and their displacements are simulated by forward modeling.

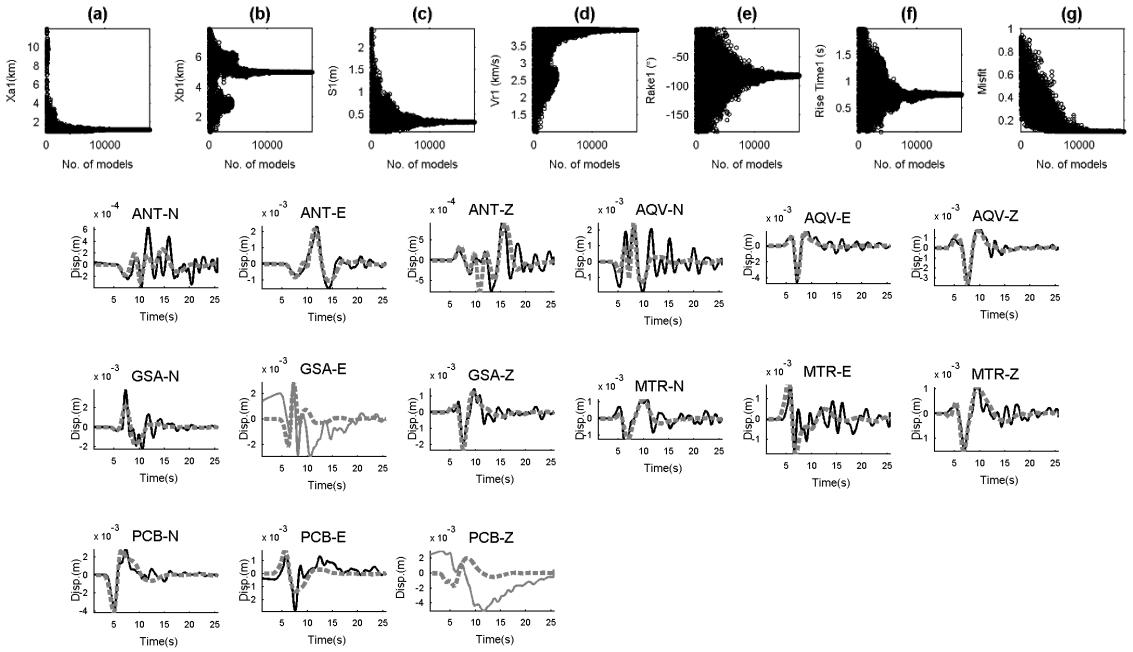

Figure Sb12. A) Convergence of model#2 source parameters obtained for the MW?? 00:52 event. b) Waveform fit for the model#2. Black and gray are real and synthetics, respectively. Gray solid lines did not use in the inversion and their displacements are simulated by forward modeling.

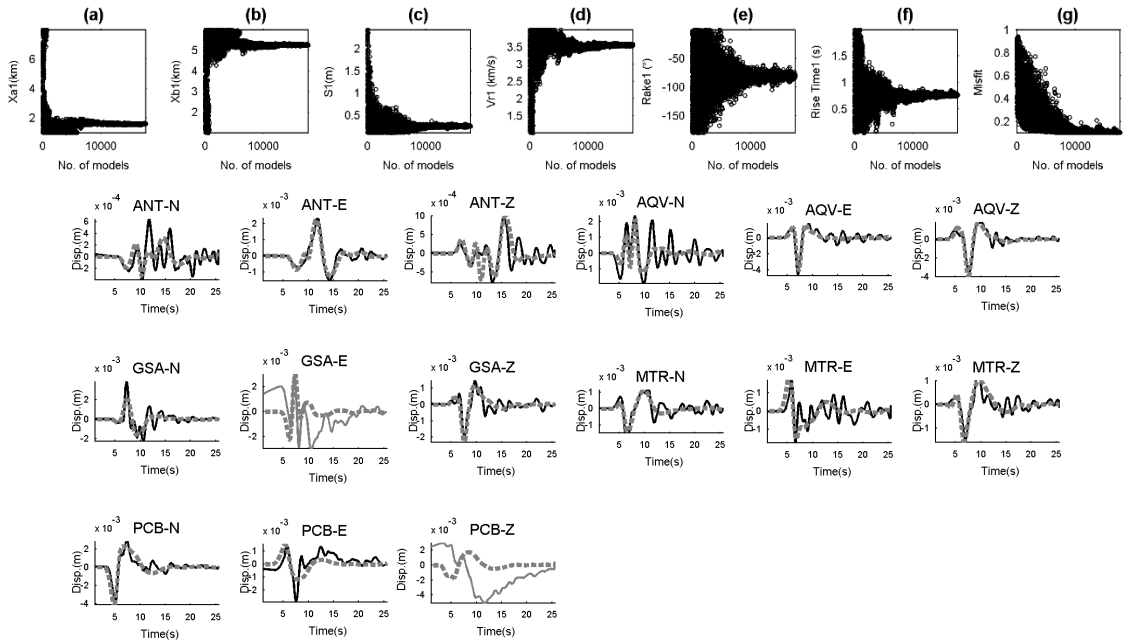

Figure Sb13. A) Convergence of model#3 source parameters obtained for the MW?? 00:52 event. b) Waveform fit for the model#3. Black and gray are real and synthetics, respectively. Gray solid lines did not use in the inversion and their displacements are simulated by forward modeling.

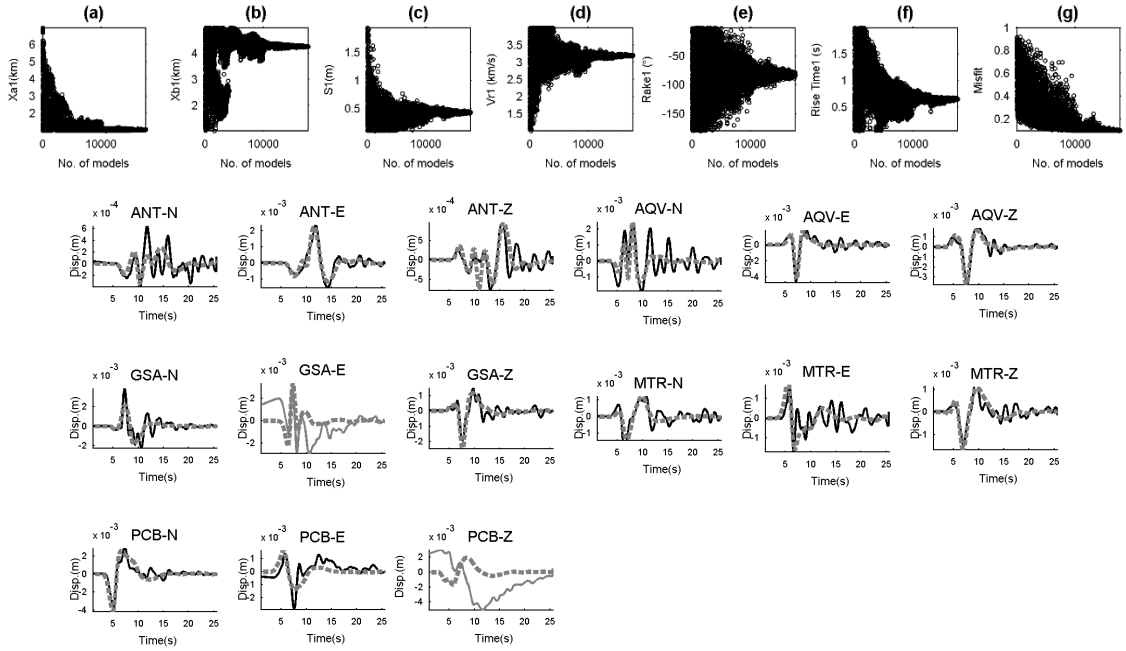

Figure Sb14. A) Convergence of model#4 source parameters obtained for the MW?? 00:52 event. b) Waveform fit for the model#4. Black and gray are real and synthetics, respectively. Gray solid lines did not use in the inversion and their displacements are simulated by forward modeling.

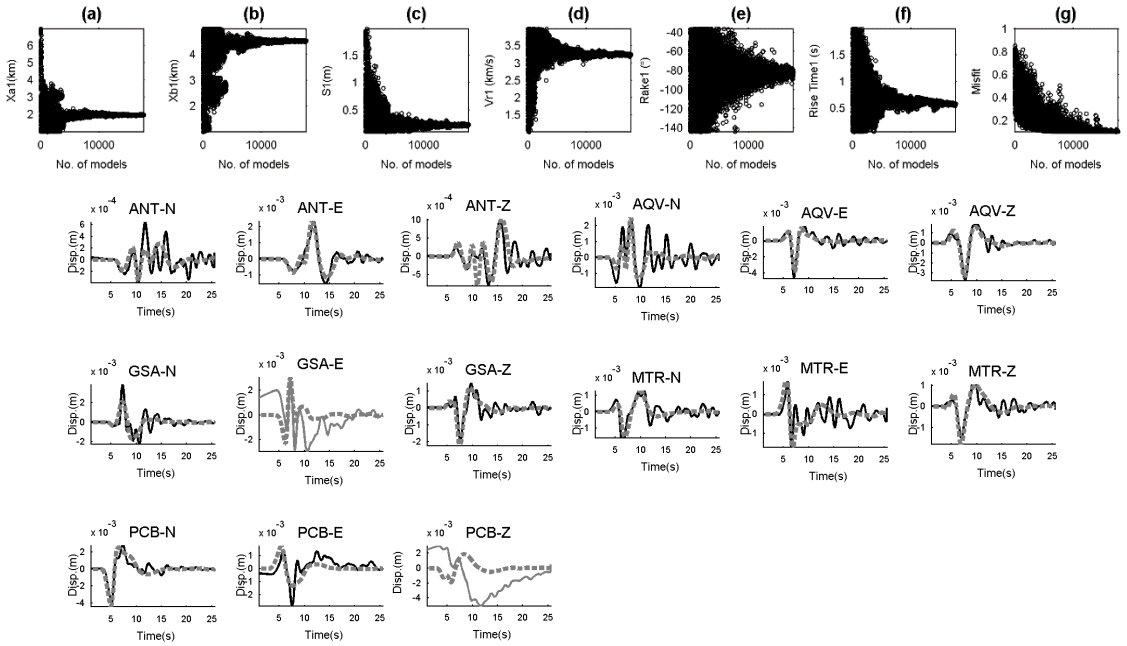

Figure Sb15. A) Convergence of model#5 source parameters obtained for the MW?? 00:52 event. b) Waveform fit for the model#5. Black and gray are real and synthetics, respectively. Gray solid lines did not use in the inversion and their displacements are simulated by forward modeling.

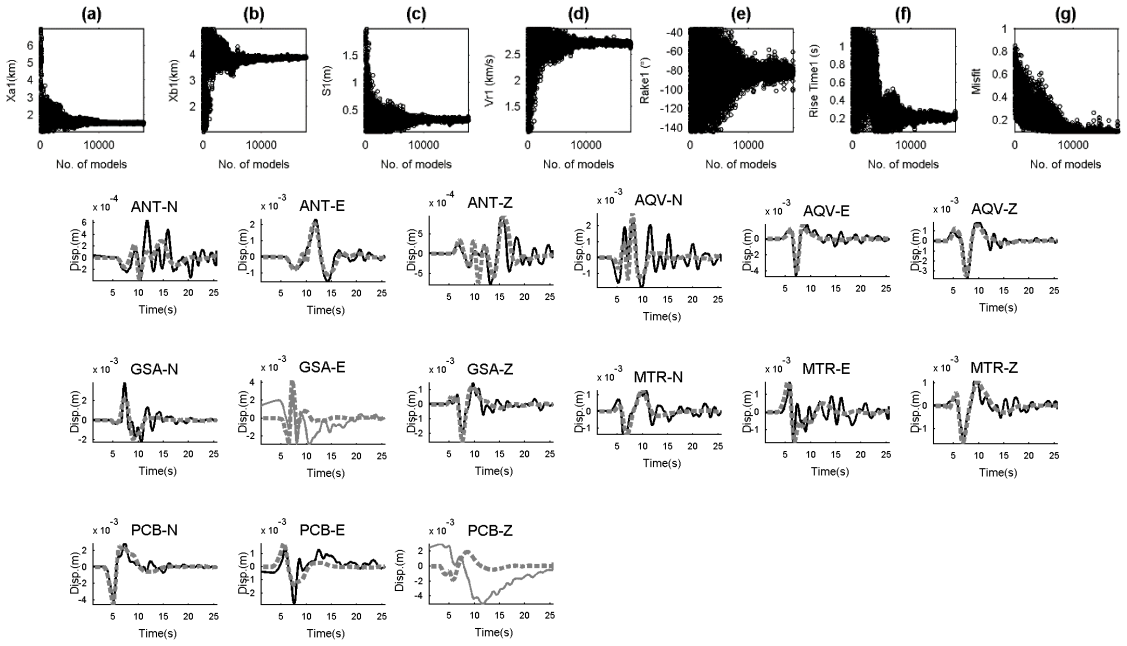

Figure Sb16. A) Convergence of model#6 source parameters obtained for the MW?? 00:52 event. b) Waveform fit for the model#6. Black and gray are real and synthetics, respectively. Gray solid lines did not use in the inversion and their displacements are simulated by forward modeling.

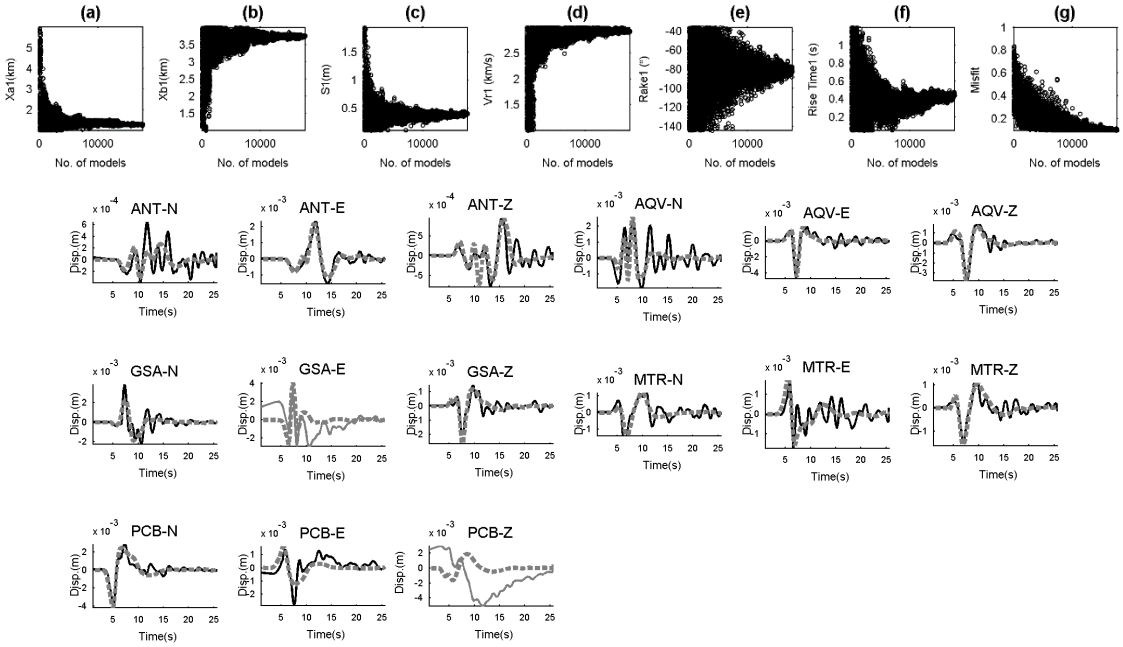

Figure Sb17. A) Convergence of model#7 source parameters obtained for the MW?? 00:52 event. b) Waveform fit for the model#7. Black and gray are real and synthetics, respectively. Gray solid lines did not use in the inversion and their displacements are simulated by forward modeling.

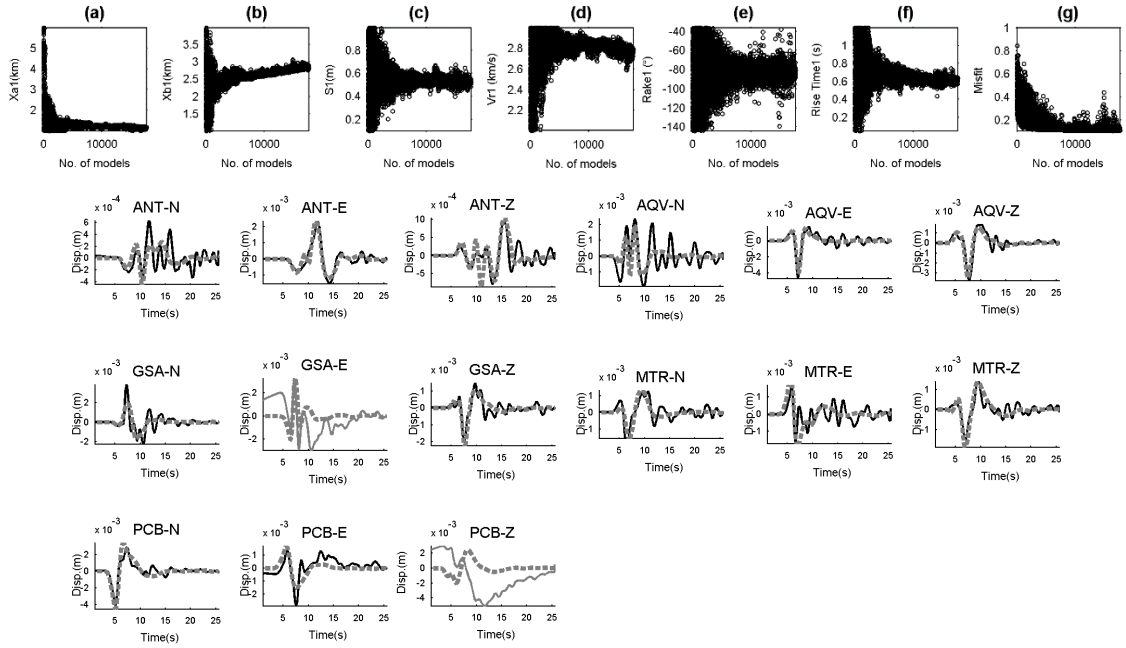

Figure Sb18. A) Convergence of model#8 source parameters obtained for the MW?? 00:52 event. b) Waveform fit for the model#8. Black and gray are real and synthetics, respectively. Gray solid lines did not use in the inversion and their displacements are simulated by forward modeling.

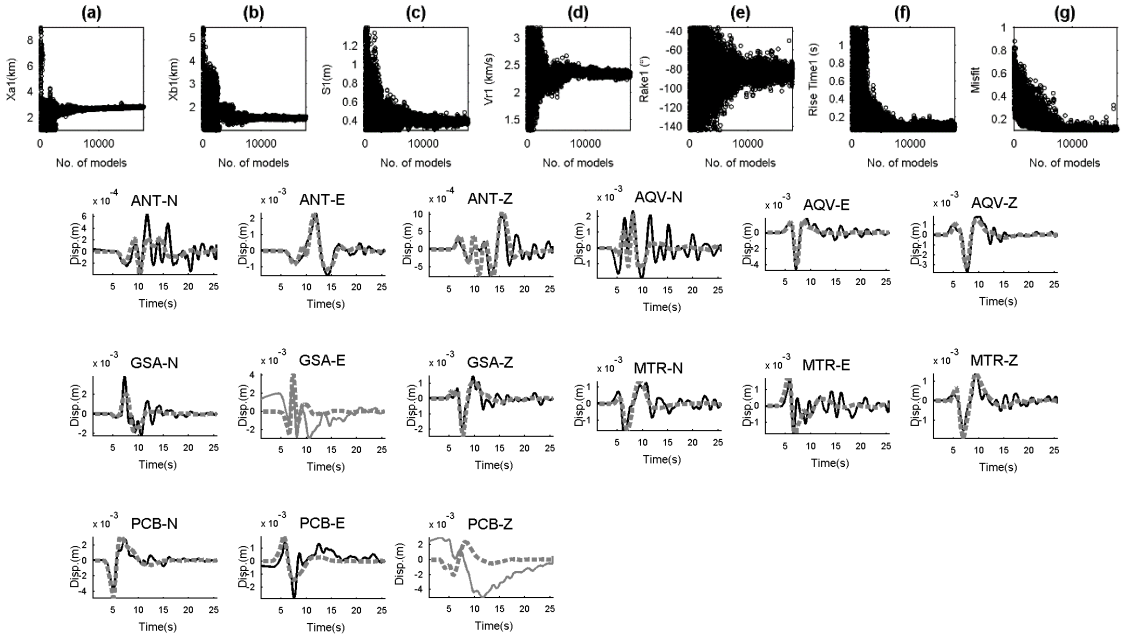

Figure Sb19. A) Convergence of model#9 source parameters obtained for the MW?? 00:52 event. b) Waveform fit for the model#9. Black and gray are real and synthetics, respectively. Gray solid lines did not use in the inversion and their displacements are simulated by forward modeling.

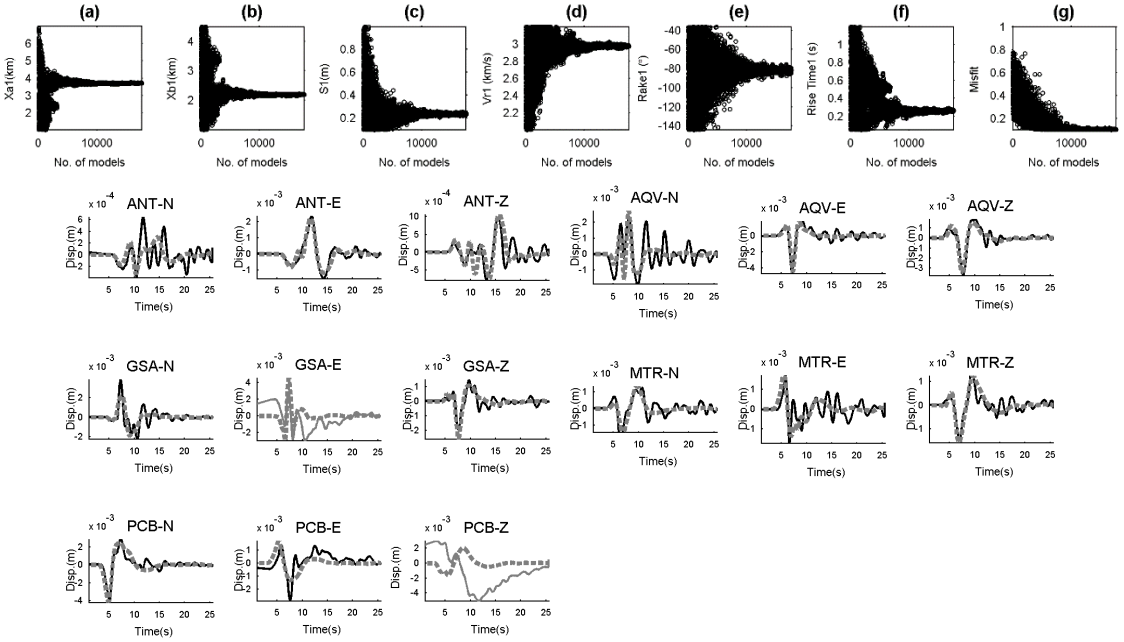

Figure Sb20. A) Convergence of model#10 source parameters obtained for the MW?? 00:52 event. b) Waveform fit for the model#10. Black and gray are real and synthetics, respectively. Gray solid lines did not use in the inversion and their displacements are simulated by forward modeling.

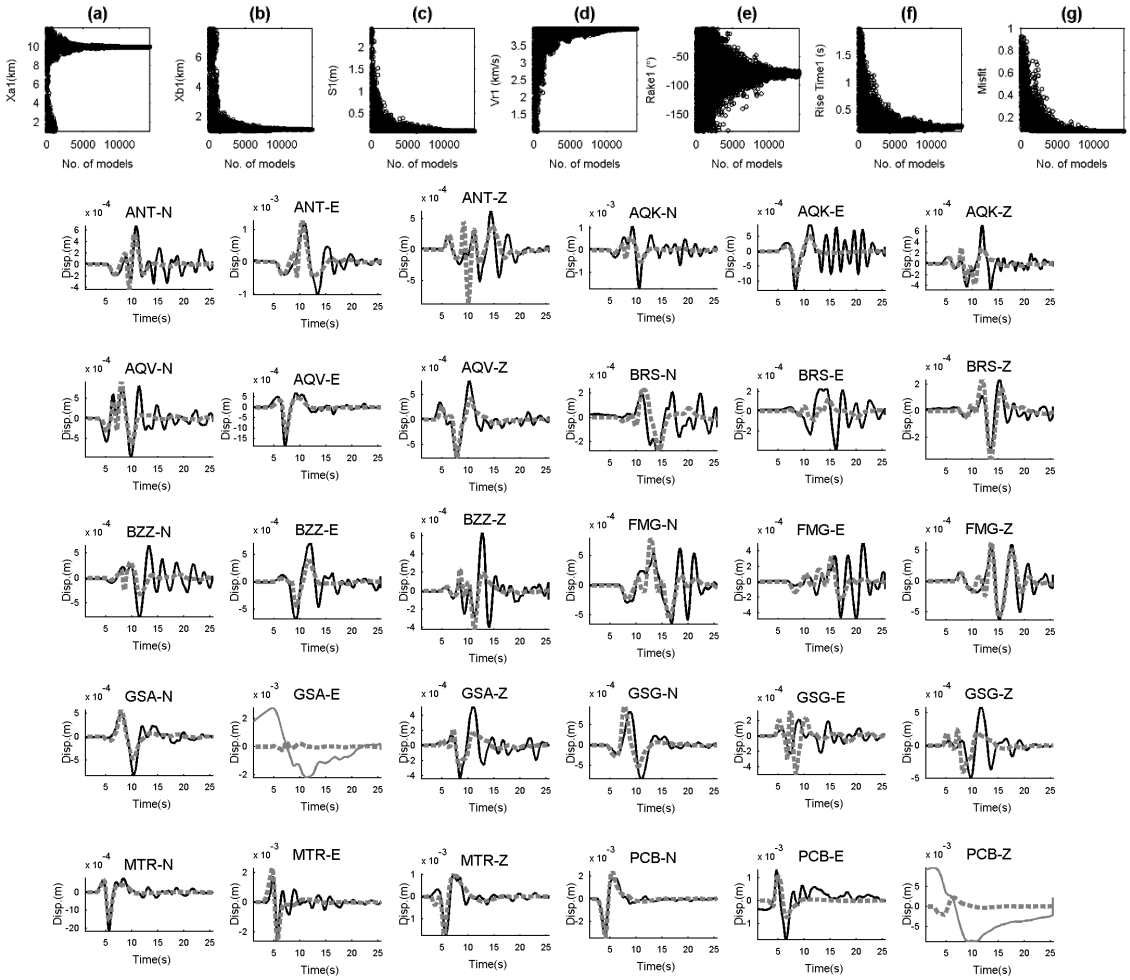

Figure Sb21. A) Convergence of model#1 source parameters obtained for the ML5.0 19:38:17 (GMT) event. b) Waveform fit for the model#1. Black solid and gray dashed lines are real and synthetics, respectively. Gray solid lines did not use in the inversion and their displacements are simulated by forward modeling.

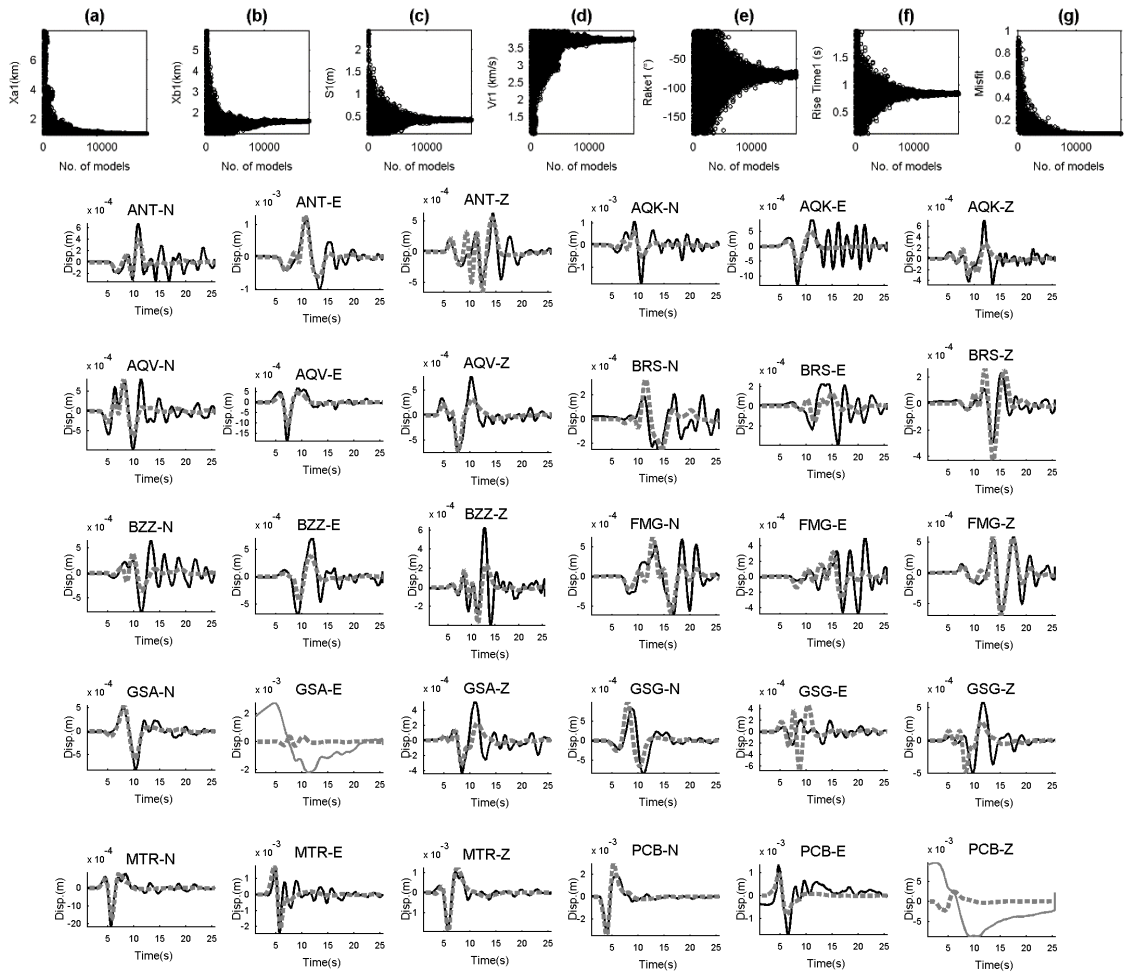

Figure Sb22. A) Convergence of model#2 source parameters obtained for the ML5.0 19:38:17 (GMT) event. b) Waveform fit for the model#2. Black solid and gray dashed lines are real and synthetics, respectively. Gray solid lines did not use in the inversion and their displacements are simulated by forward modeling.

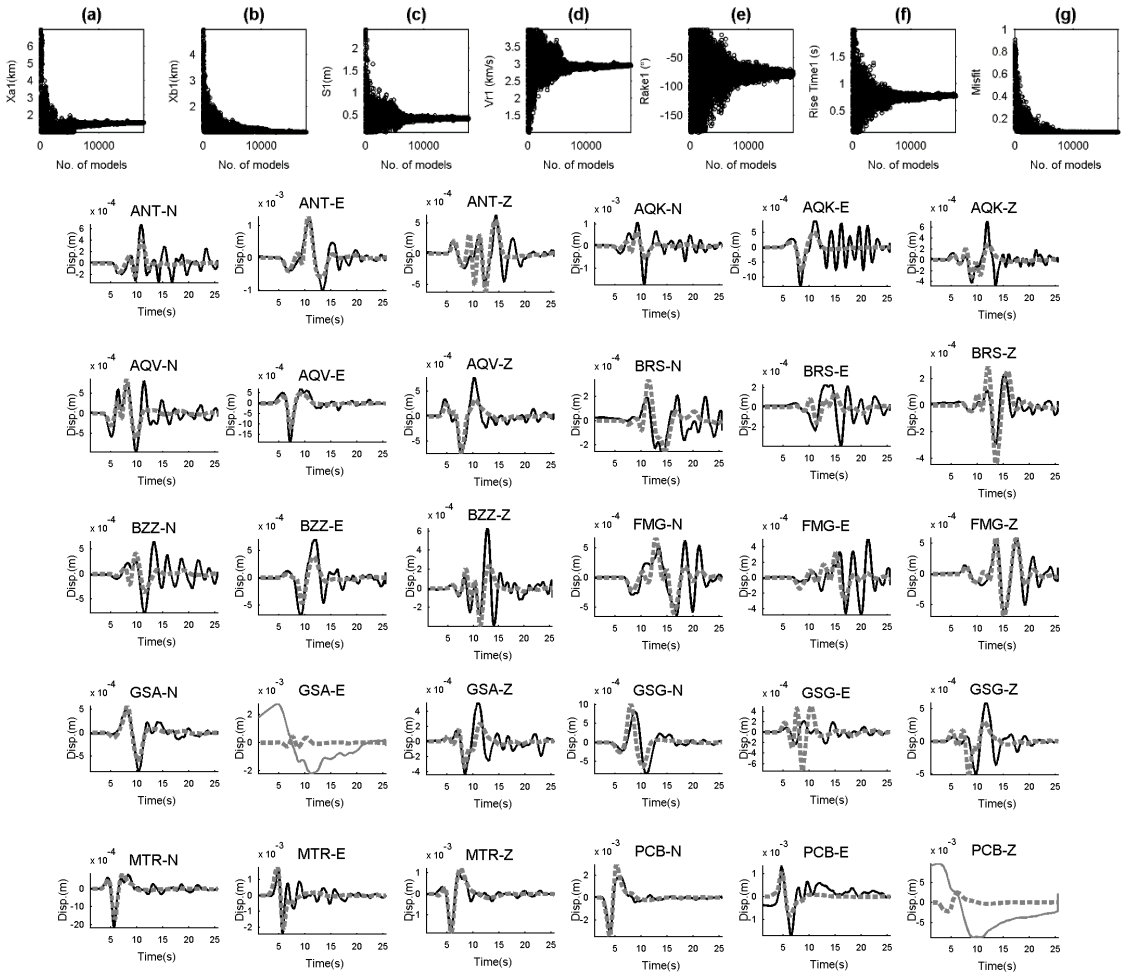

Figure Sb23. A) Convergence of model#3 source parameters obtained for the ML5.0 19:38:17 (GMT) event. b) Waveform fit for the model#3. Black solid and gray dashed lines are real and synthetics, respectively. Gray solid lines did not use in the inversion and their displacements are simulated by forward modeling.

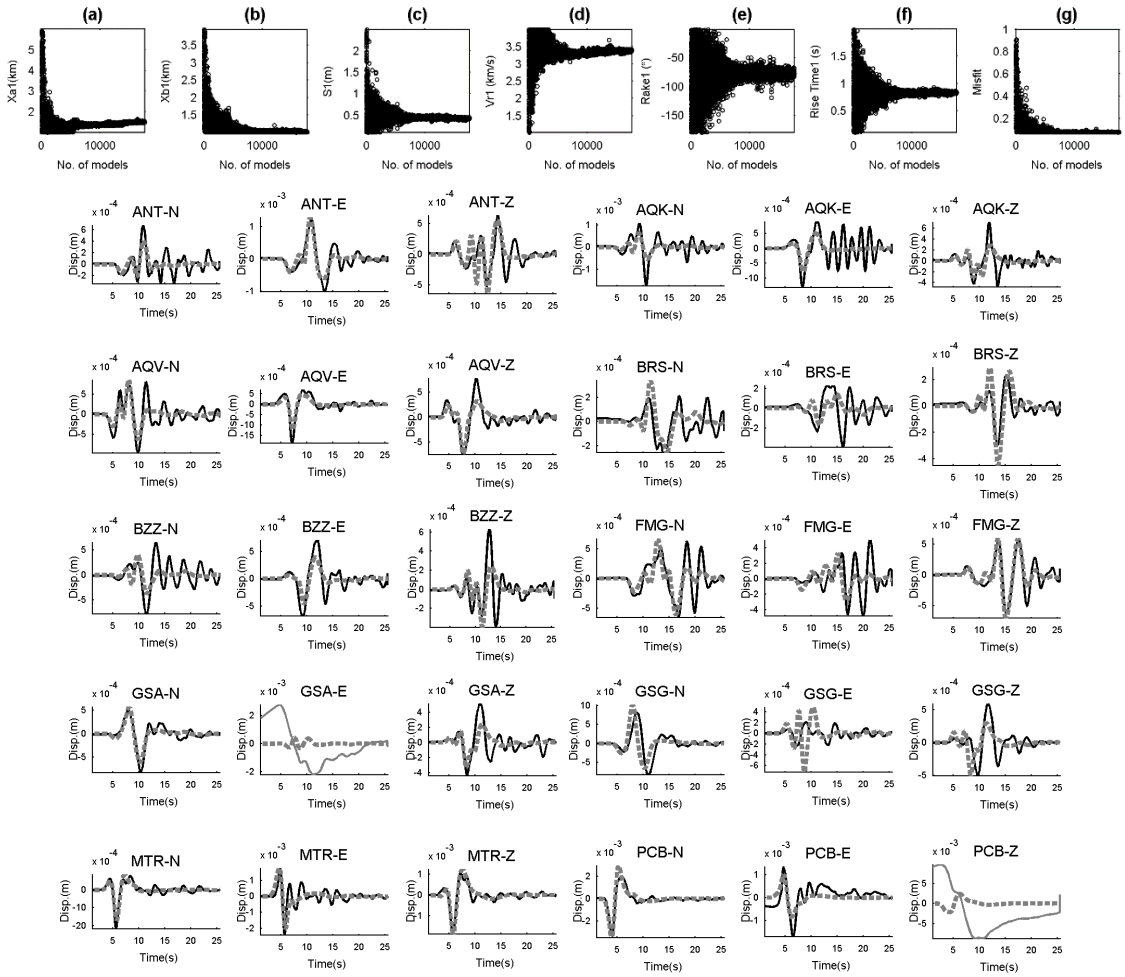

Figure Sb24. A) Convergence of model#4 source parameters obtained for the ML5.0 19:38:17 (GMT) event. b) Waveform fit for the model#4. Black solid and gray dashed lines are real and synthetics, respectively. Gray solid lines did not use in the inversion and their displacements are simulated by forward modeling.

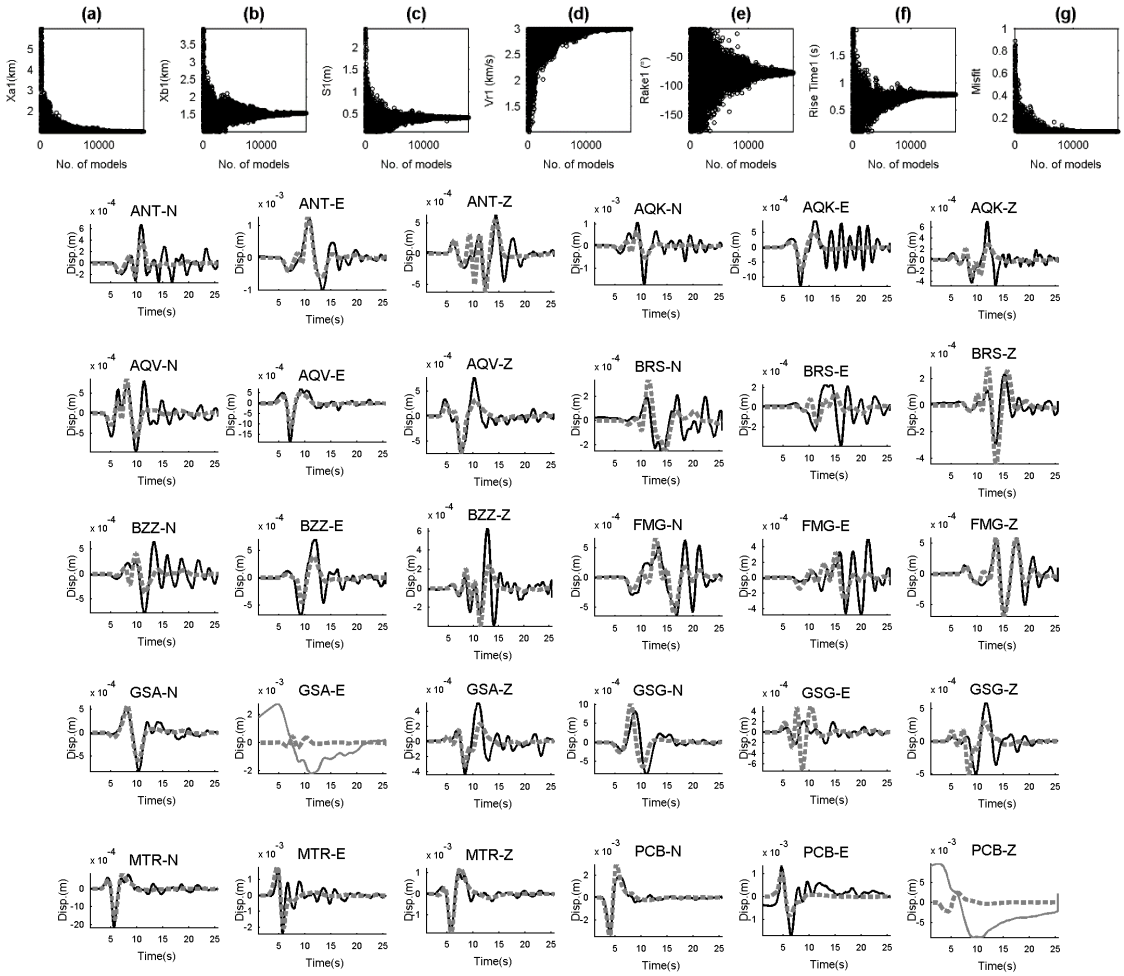

Figure Sb25. A) Convergence of model#5 source parameters obtained for the ML5.0 19:38:17 (GMT) event. b) Waveform fit for the model#5. Black solid and gray dashed lines are real and synthetics, respectively. Gray solid lines did not use in the inversion and their displacements are simulated by forward modeling.

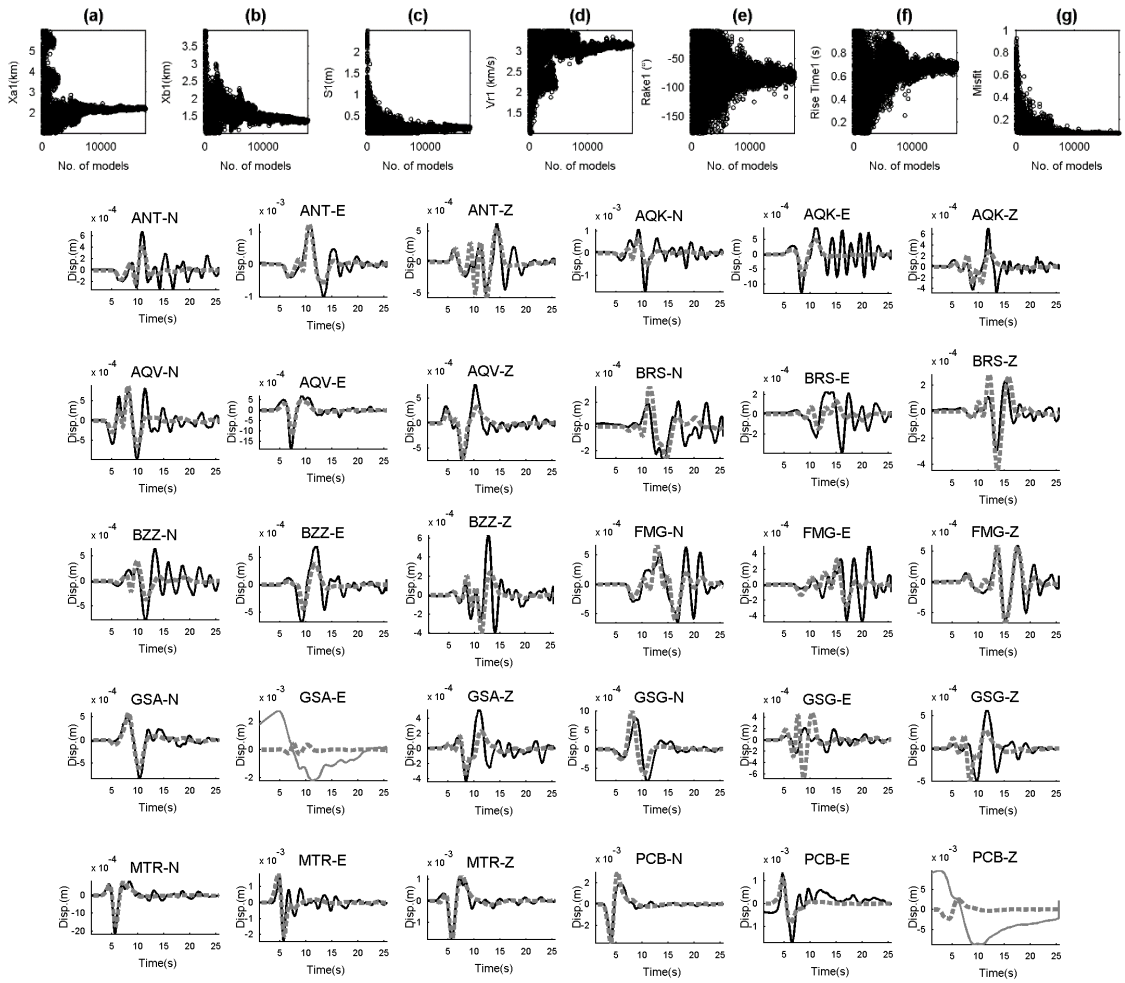

Figure Sb26. A) Convergence of model#6 source parameters obtained for the ML5.0 19:38:17 (GMT) event. b) Waveform fit for the model#6. Black solid and gray dashed lines are real and synthetics, respectively. Gray solid lines did not use in the inversion and their displacements are simulated by forward modeling.

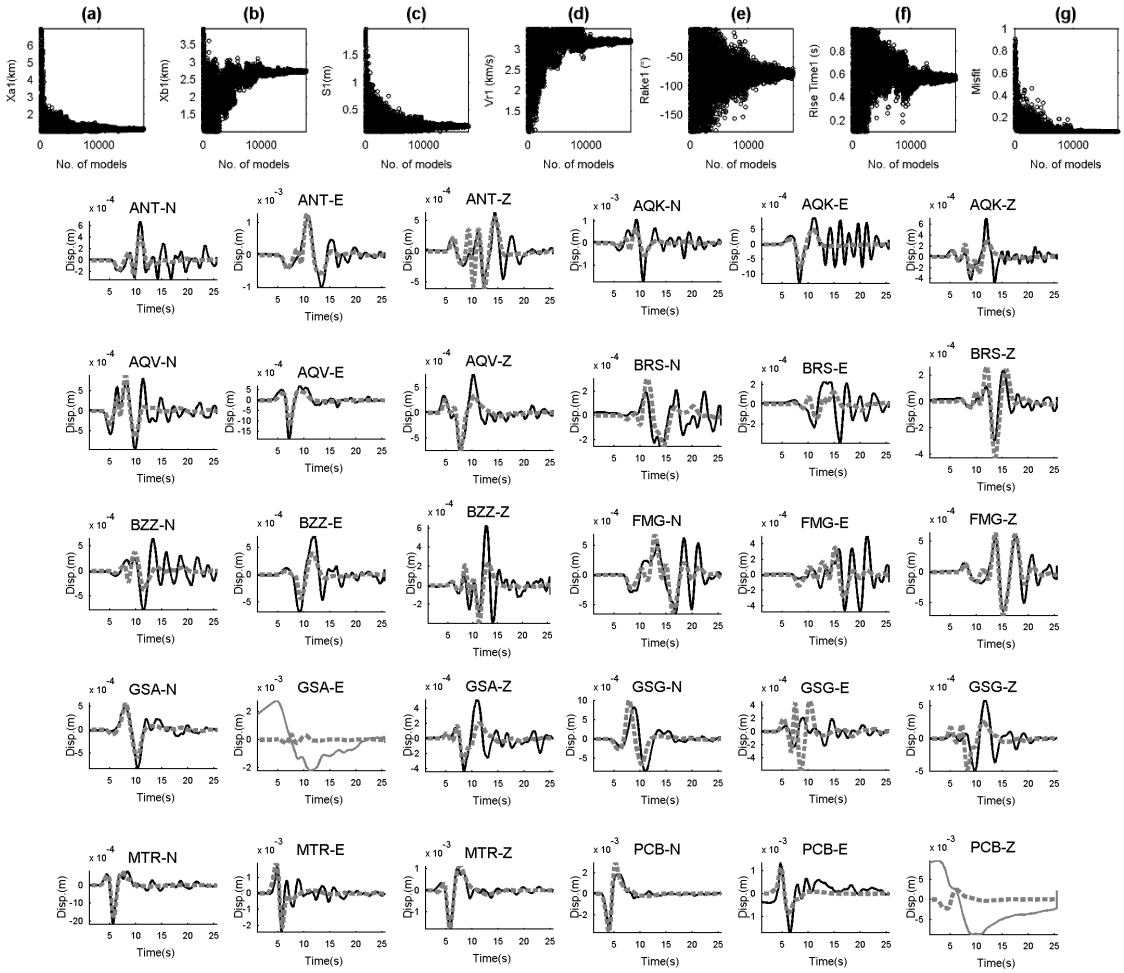

Figure Sb27. A) Convergence of model#7 source parameters obtained for the ML5.0 19:38:17 (GMT) event. b) Waveform fit for the model#7. Black solid and gray dashed lines are real and synthetics, respectively. Gray solid lines did not use in the inversion and their displacements are simulated by forward modeling.

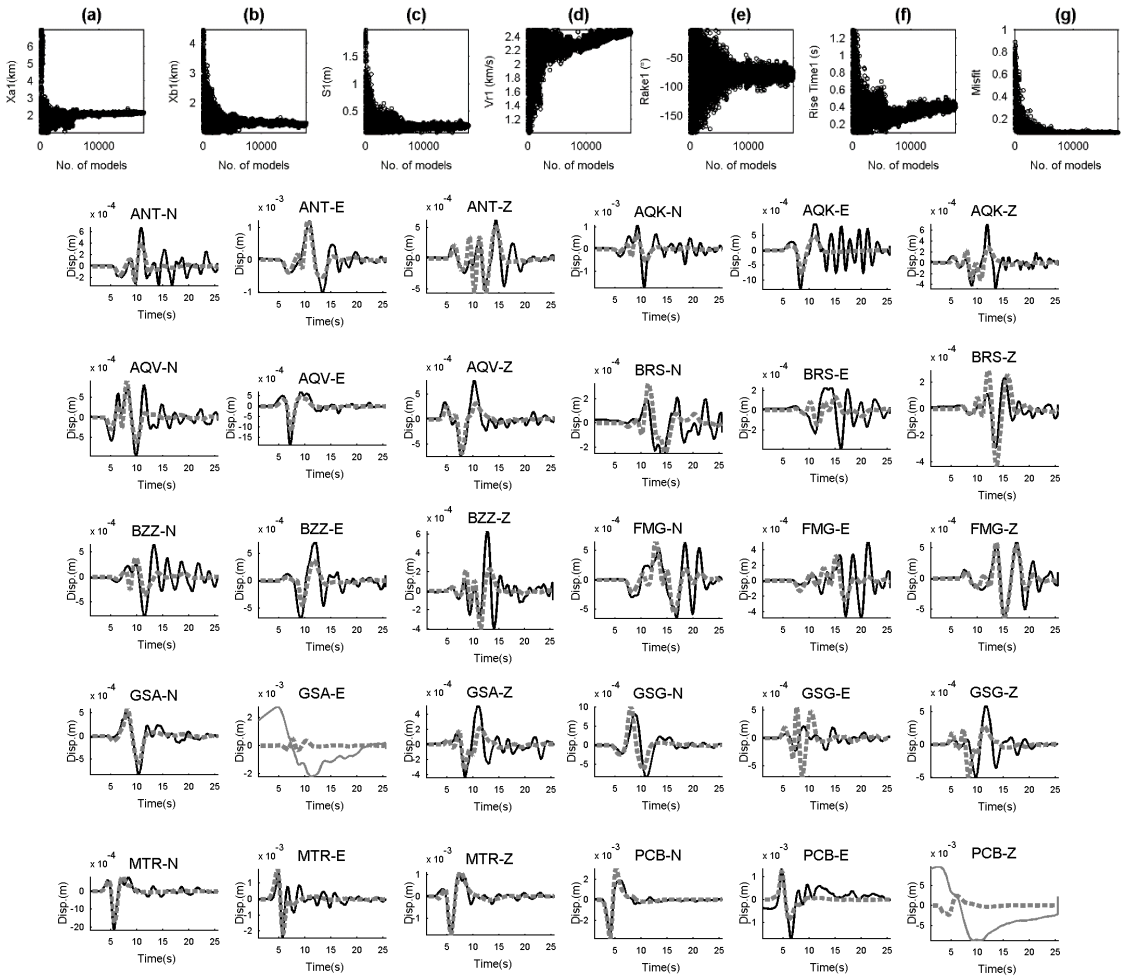

Figure Sb28. A) Convergence of model#8 source parameters obtained for the ML5.0 19:38:17 (GMT) event. b) Waveform fit for the model#8. Black solid and gray dashed lines are real and synthetics, respectively. Gray solid lines did not use in the inversion and their displacements are simulated by forward modeling.

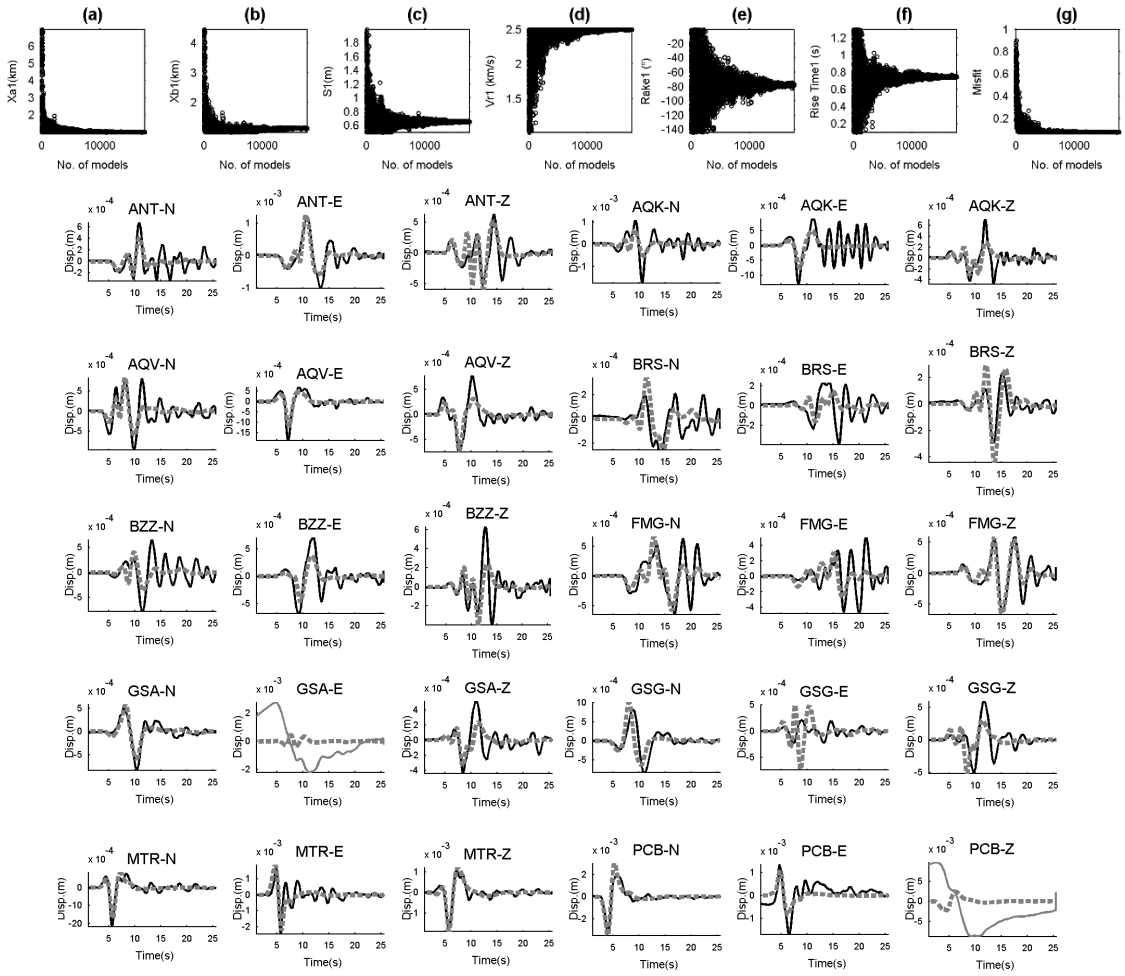

Figure Sb29. A) Convergence of model#9 source parameters obtained for the ML5.0 19:38:17 (GMT) event. b) Waveform fit for the model#9. Black solid and gray dashed lines are real and synthetics, respectively. Gray solid lines did not use in the inversion and their displacements are simulated by forward modeling.

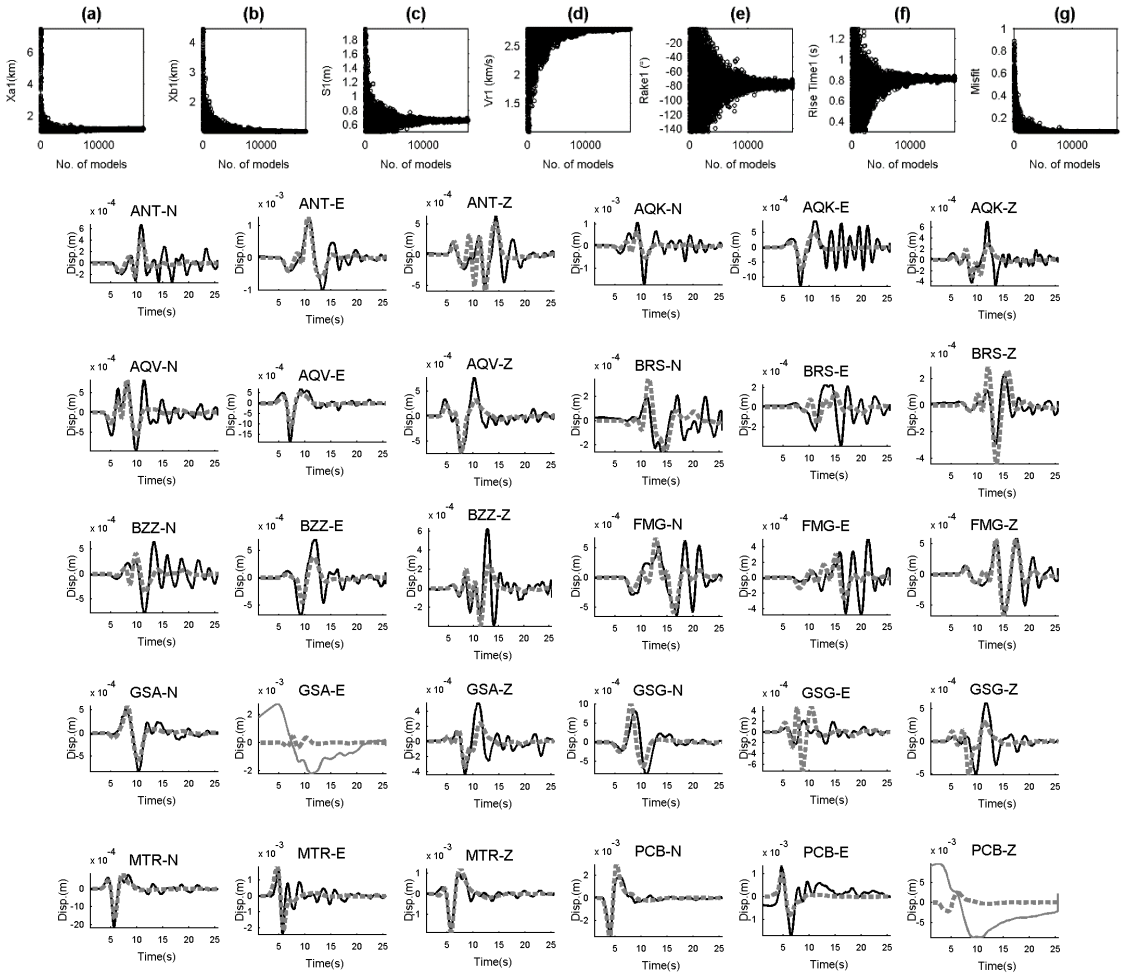

Figure Sb30. A) Convergence of model#10 source parameters obtained for the ML5.0 19:38:17 (GMT) event. b) Waveform fit for the model#10. Black solid and gray dashed lines are real and synthetics, respectively. Gray solid lines did not use in the inversion and their displacements are simulated by forward modeling.

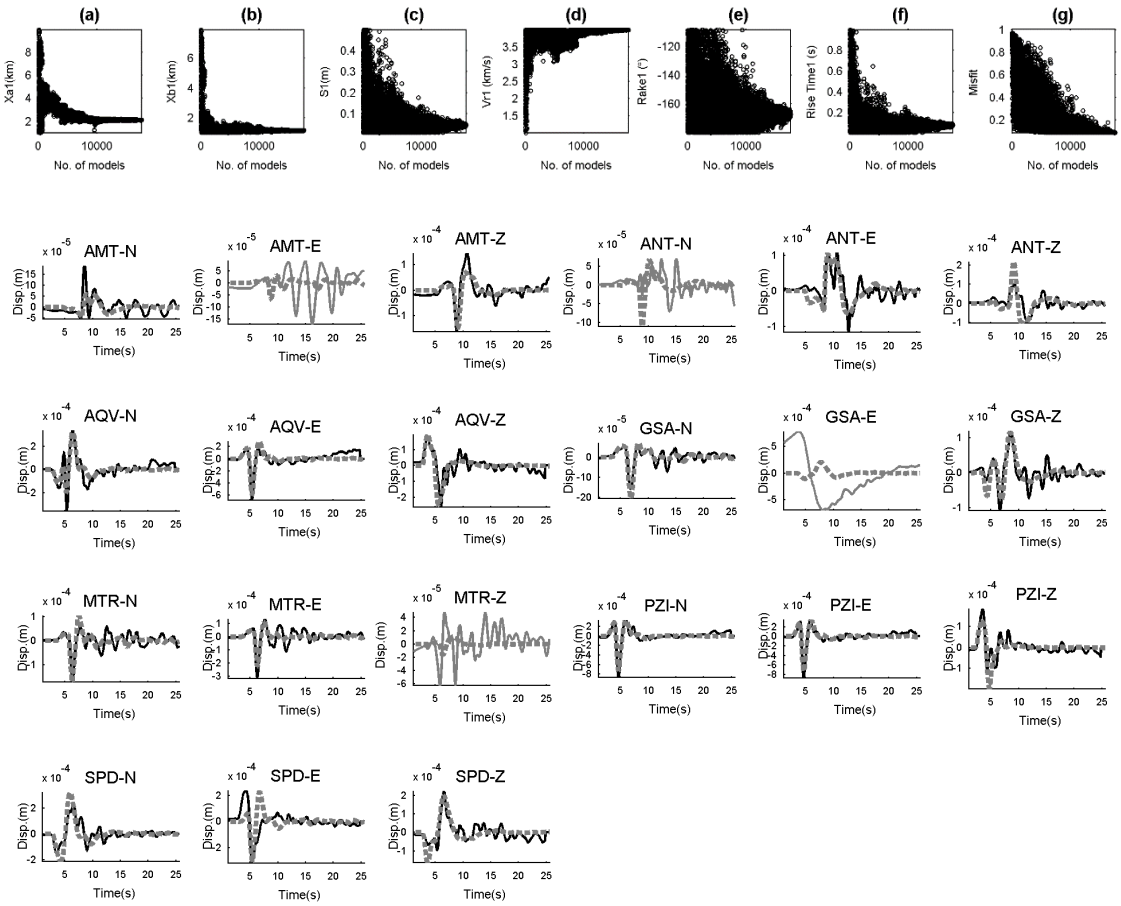

Figure Sb31. A) Convergence of model#1 source parameters obtained for the ML4.4 20:58:40 (GMT) decollement event. b) Waveform fit for the model#1. Black and gray are real and synthetics, respectively. Gray solid lines did not use in the inversion and their displacements are simulated by forward modeling.

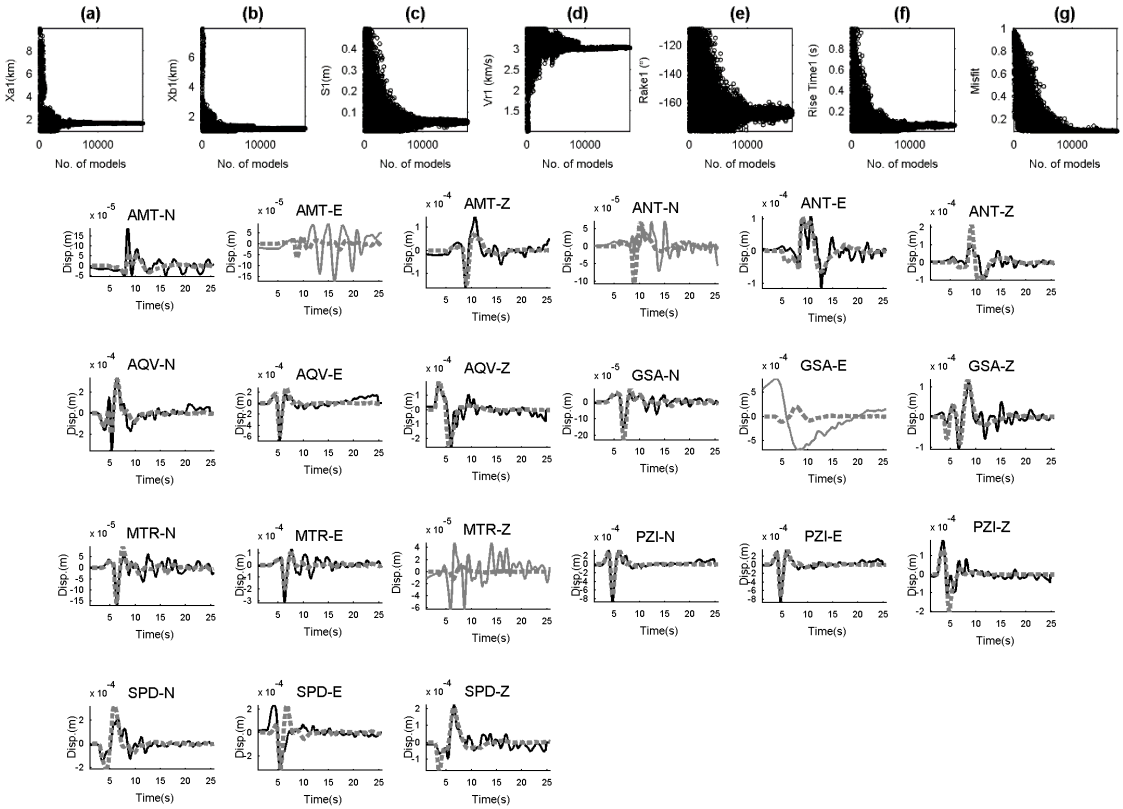

Figure Sb32. A) Convergence of model#2 source parameters obtained for the ML4.4 20:58:40 (GMT) decollement event. b) Waveform fit for the model#2. Black and gray are real and synthetics, respectively. Gray solid lines did not use in the inversion and their displacements are simulated by forward modeling.

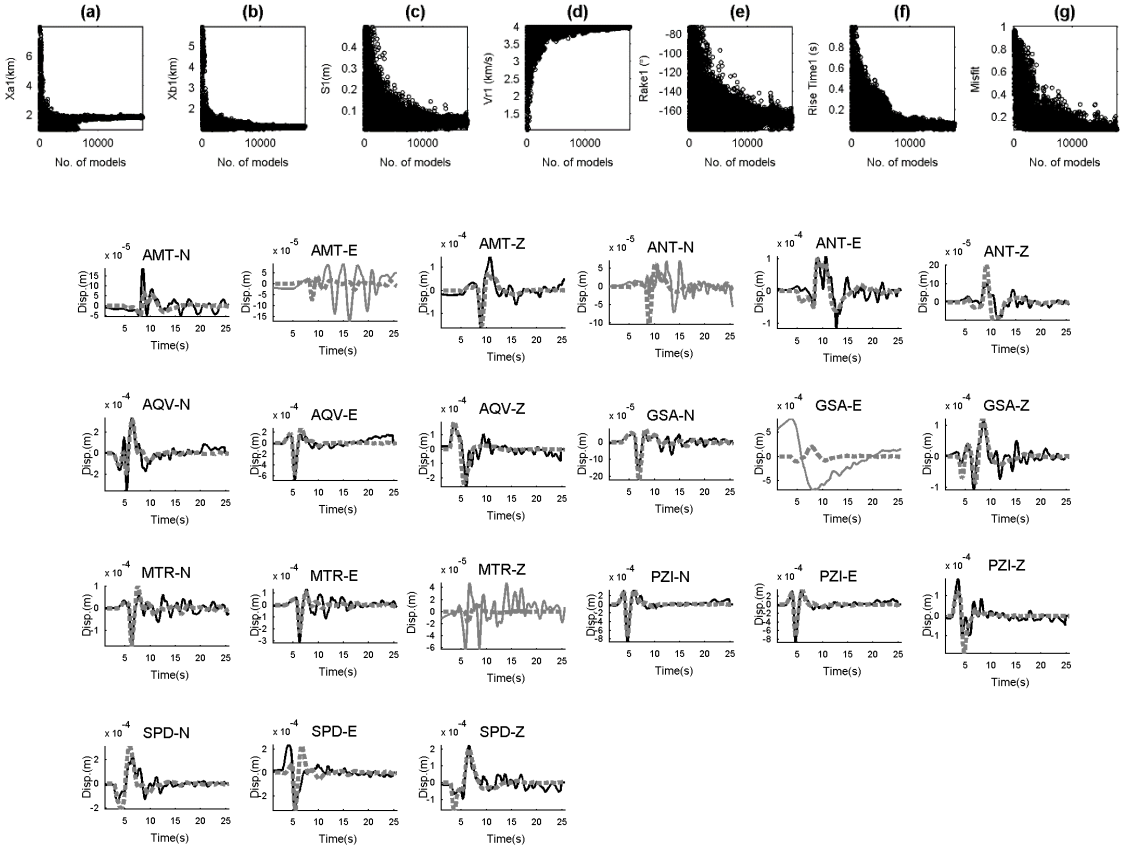

Figure Sb33. A) Convergence of model#3 source parameters obtained for the ML4.4 20:58:40 (GMT) decollement event. b) Waveform fit for the model#3. Black and gray are real and synthetics, respectively. Gray solid lines did not use in the inversion and their displacements are simulated by forward modeling.

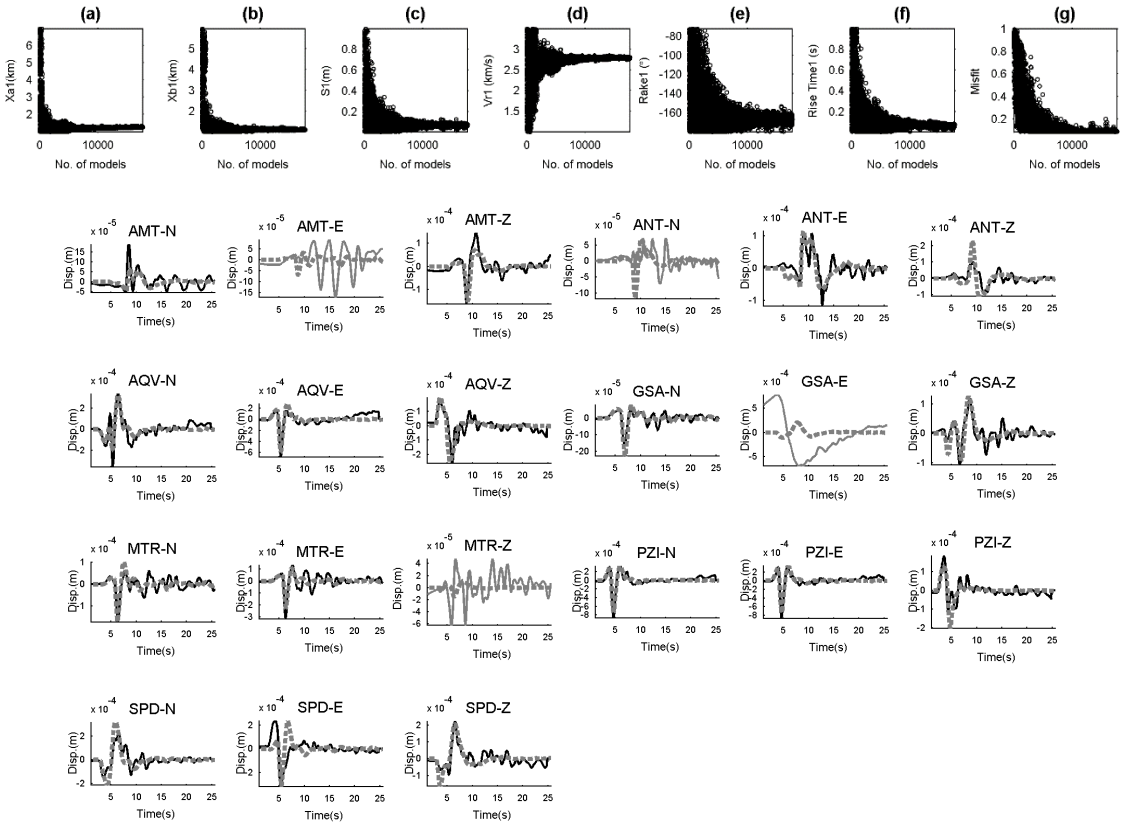

Figure Sb34. A) Convergence of model#4 source parameters obtained for the ML4.4 20:58:40 (GMT) decollement event. b) Waveform fit for the model#4. Black and gray are real and synthetics, respectively. Gray solid lines did not use in the inversion and their displacements are simulated by forward modeling.

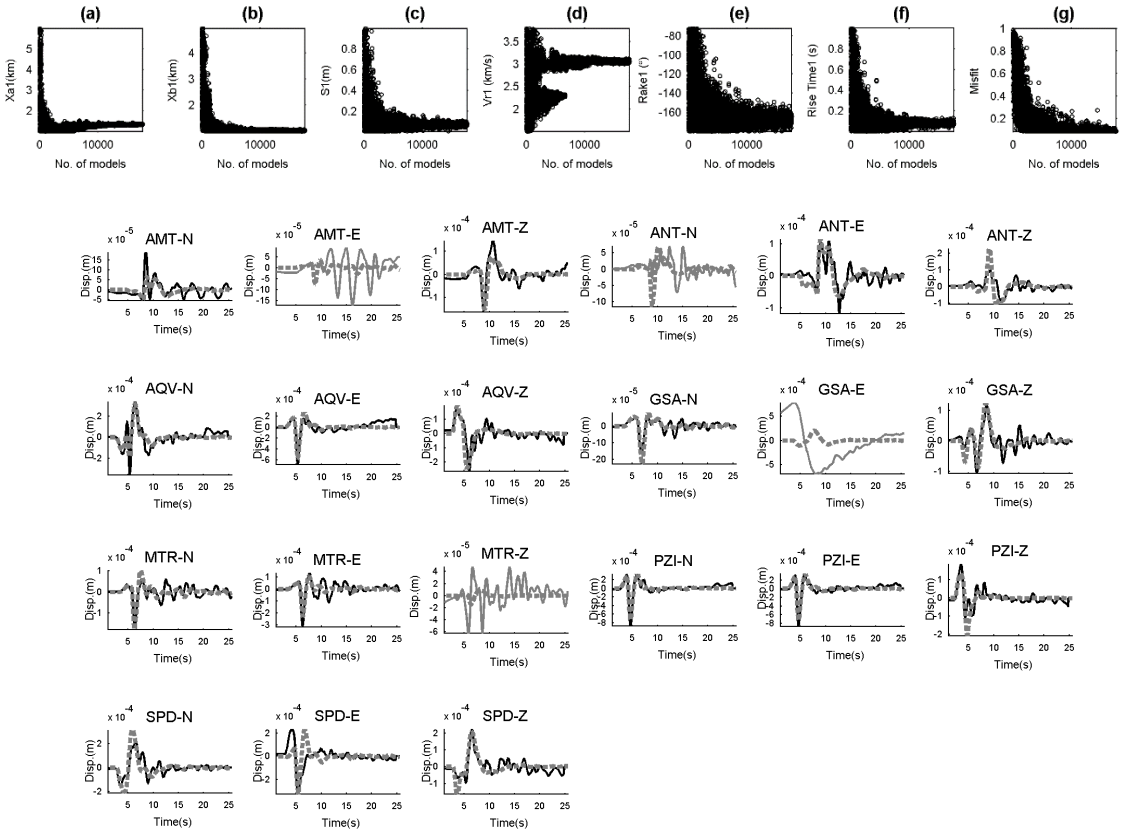

Figure Sb35. A) Convergence of model#5 source parameters obtained for the ML4.4 20:58:40 (GMT) decollement event. b) Waveform fit for the model#5. Black and gray are real and synthetics, respectively. Gray solid lines did not use in the inversion and their displacements are simulated by forward modeling.

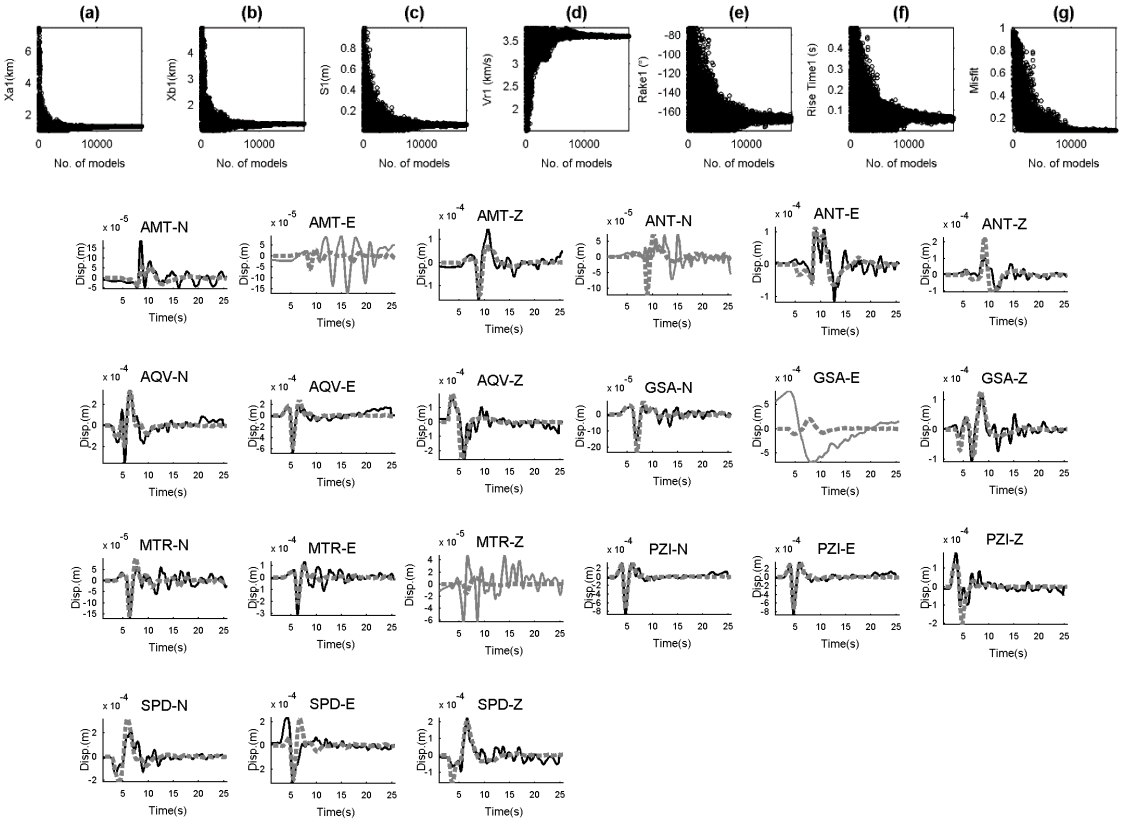

Figure Sb36. A) Convergence of model#6 source parameters obtained for the ML4.4 20:58:40 (GMT) decollement event. b) Waveform fit for the model#6. Black and gray are real and synthetics, respectively. Gray solid lines did not use in the inversion and their displacements are simulated by forward modeling.

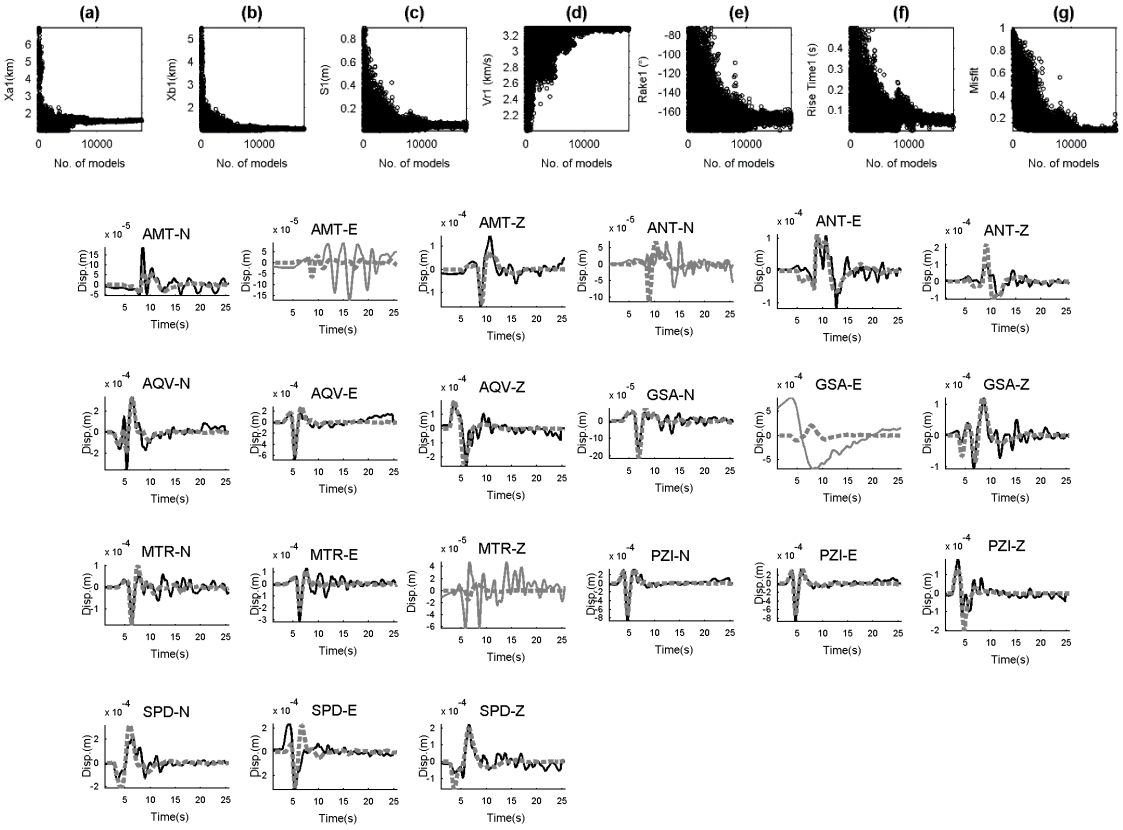

Figure Sb37. A) Convergence of model#7 source parameters obtained for the ML4.4 20:58:40 (GMT) decollement event. b) Waveform fit for the model#7. Black and gray are real and synthetics, respectively. Gray solid lines did not use in the inversion and their displacements are simulated by forward modeling.

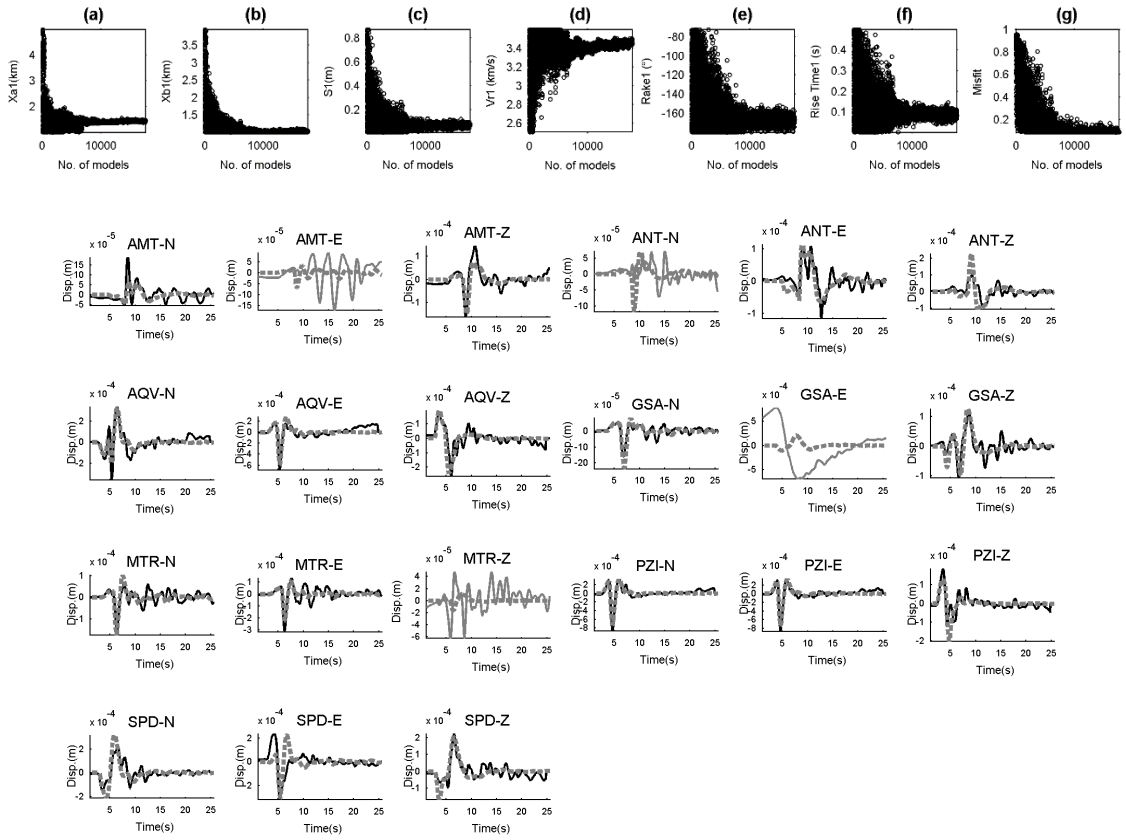

Figure Sb38. A) Convergence of model#8 source parameters obtained for the ML4.4 20:58:40 (GMT) decollement event. b) Waveform fit for the model#8. Black and gray are real and synthetics, respectively. Gray solid lines did not use in the inversion and their displacements are simulated by forward modeling.

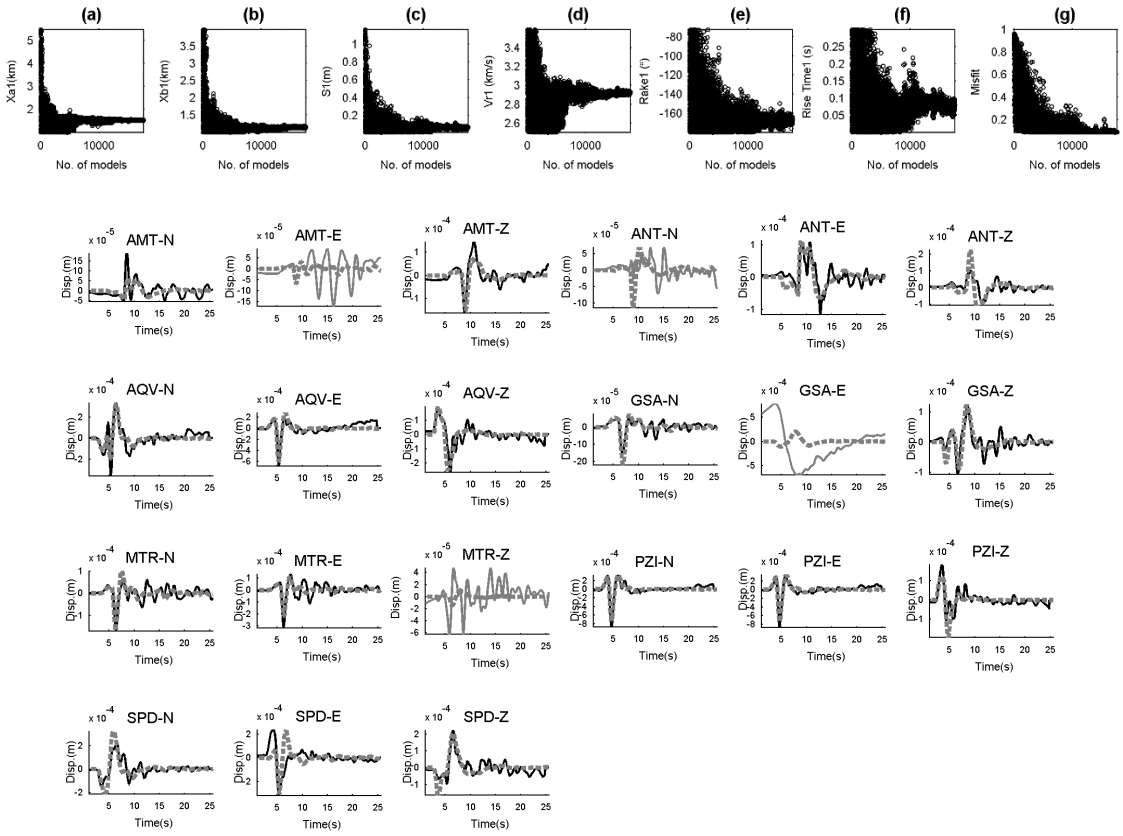

Figure Sb39. A) Convergence of model#9 source parameters obtained for the ML4.4 20:58:40 (GMT) decollement event. b) Waveform fit for the model#9. Black and gray are real and synthetics, respectively. Gray solid lines did not use in the inversion and their displacements are simulated by forward modeling.

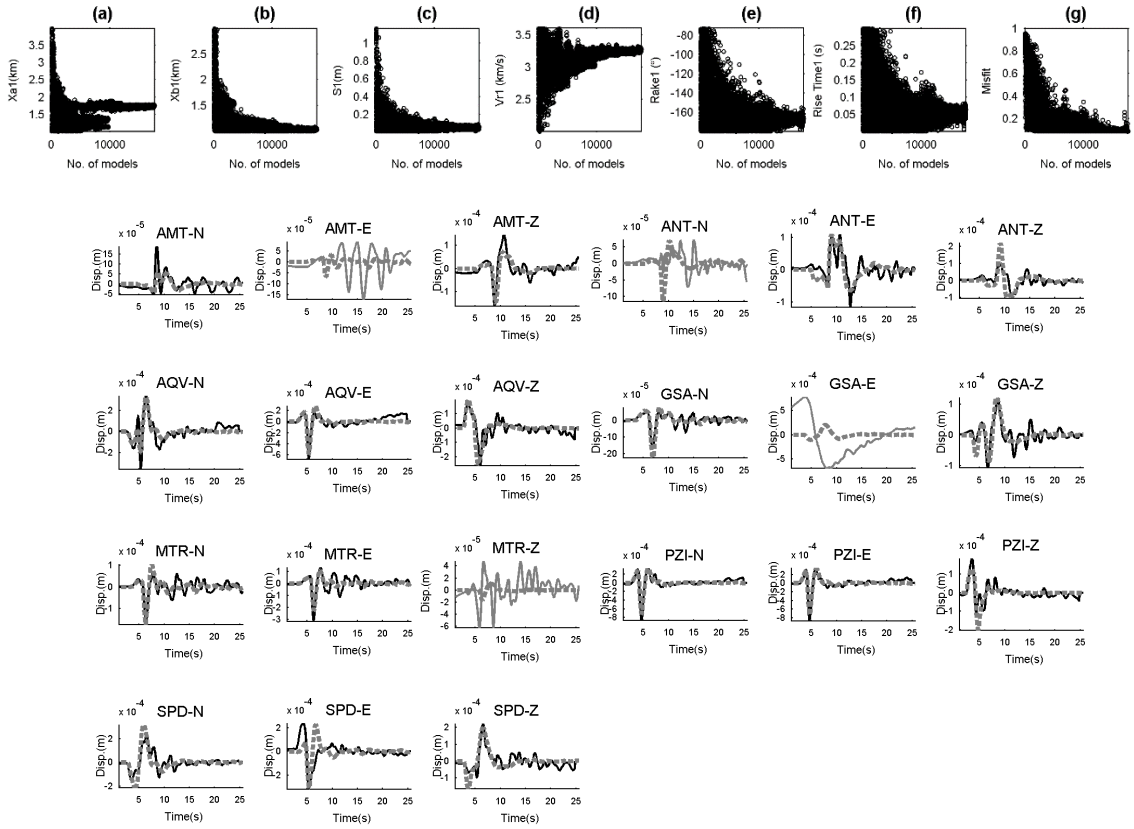

Figure Sb40. A) Convergence of model#10 source parameters obtained for the ML4.4 20:58:40 (GMT) decollement event. b) Waveform fit for the model#10. Black and gray are real and synthetics, respectively. Gray solid lines did not use in the inversion and their displacements are simulated by forward modeling.

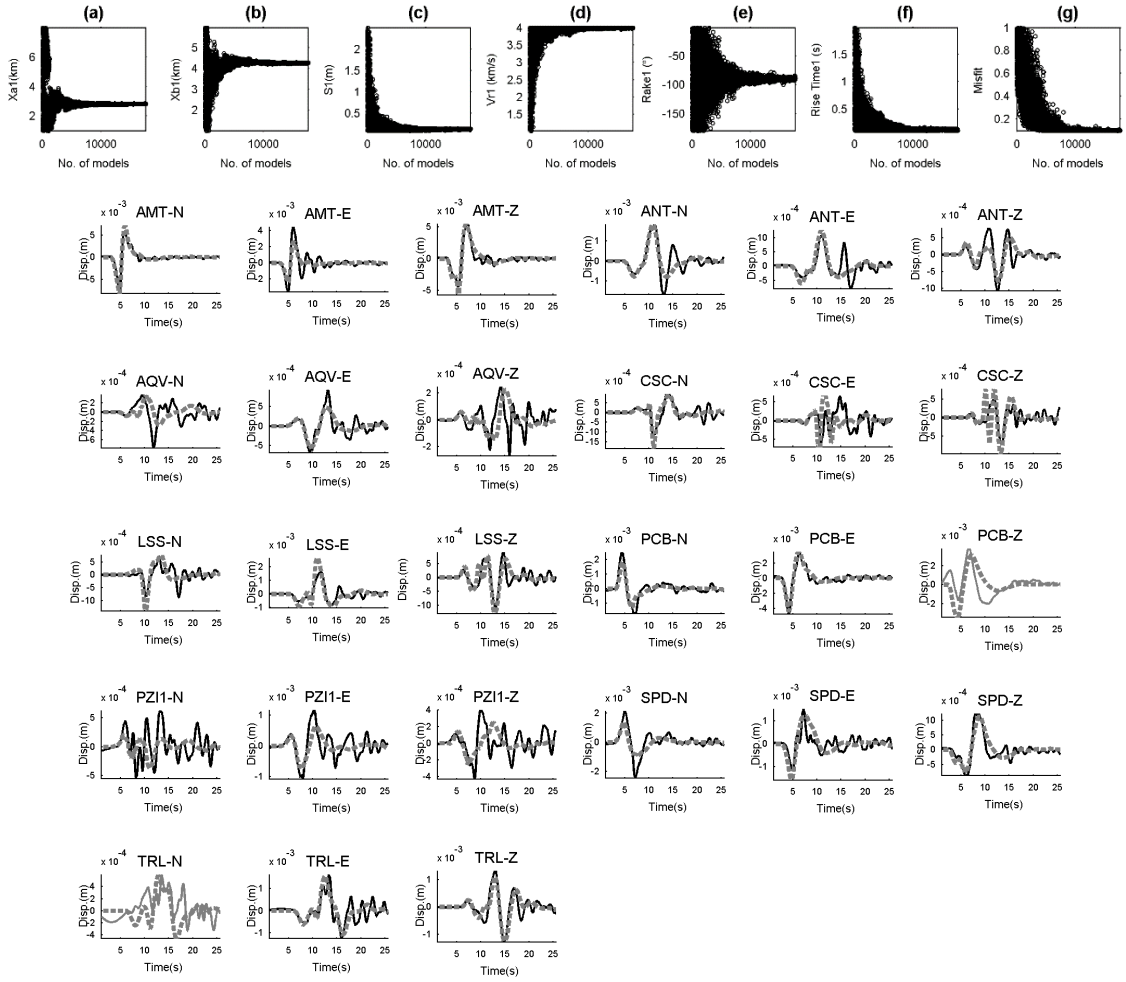

Figure Sb41. A) Convergence of model#1 source parameters obtained for the ML5.4 09:25:40 (GMT) event. b) Waveform fit of the model#1. Black and gray are real and synthetics, respectively. Gray solid lines did not use in the inversion and their displacements are simulated by forward modeling.

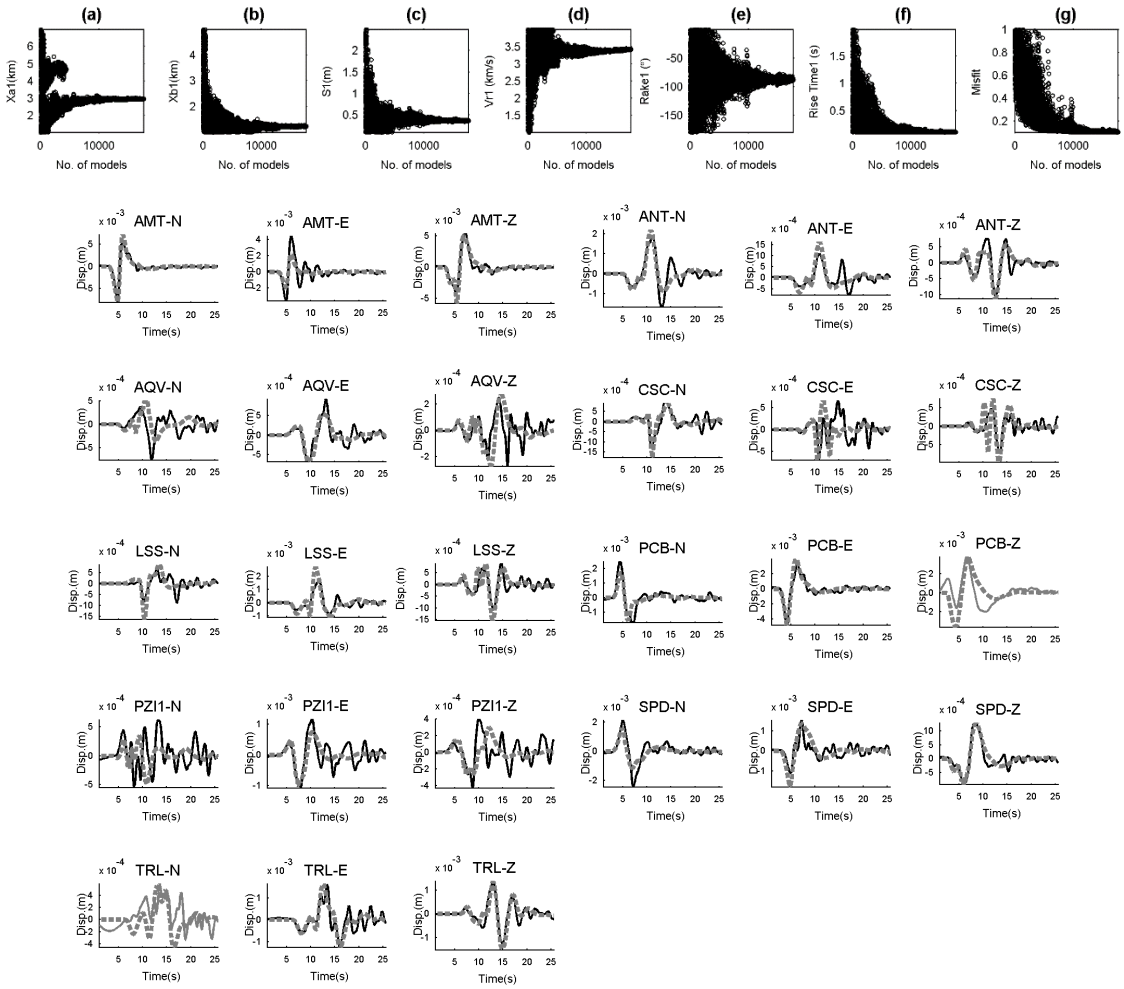

Figure Sb42. A) Convergence of model#2 source parameters obtained for the ML5.4 09:25:40 (GMT) event. b) Waveform fit of the model#2. Black and gray are real and synthetics, respectively. Gray solid lines did not use in the inversion and their displacements are simulated by forward modeling.

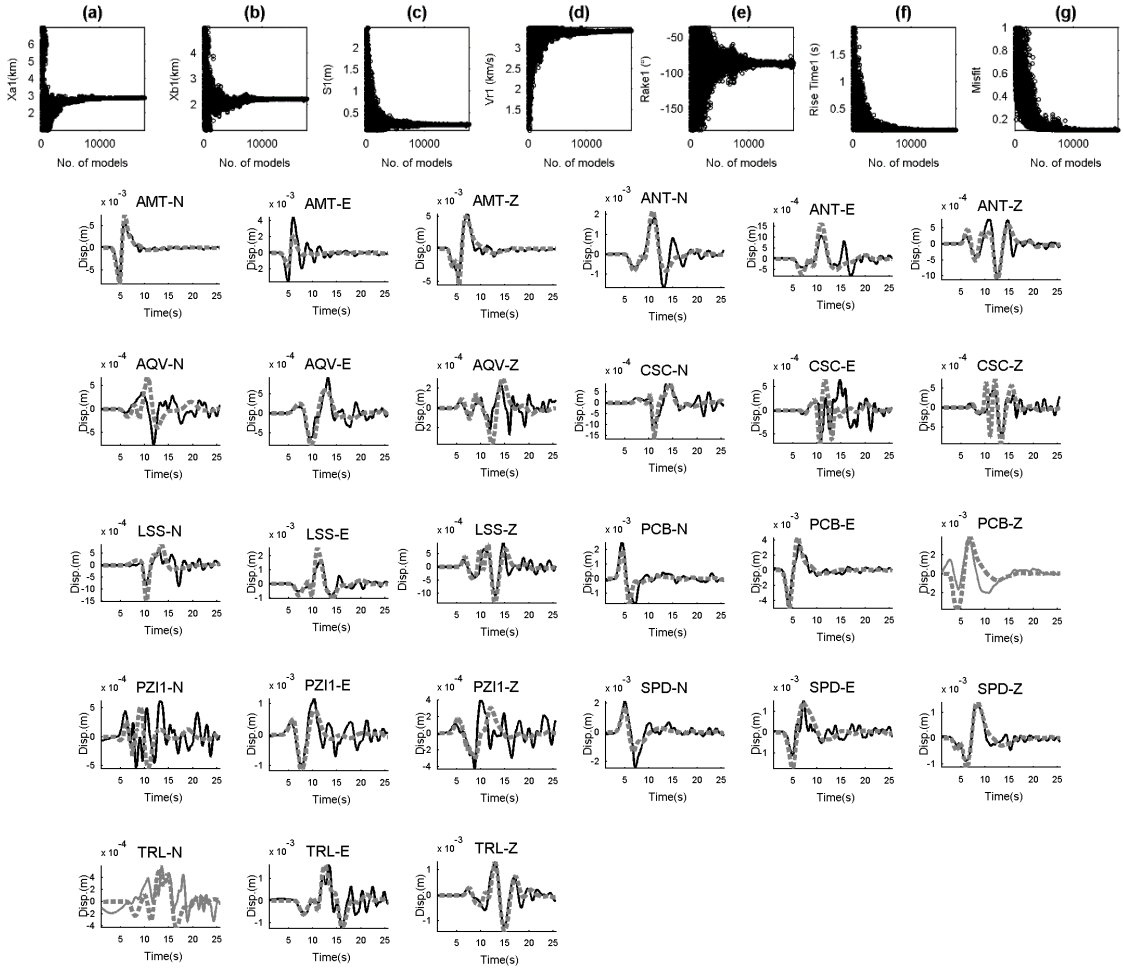

Figure Sb43. A) Convergence of model#3 source parameters obtained for the ML5.4 09:25:40 (GMT) event. b) Waveform fit of the model#3. Black and gray are real and synthetics, respectively. Gray solid lines did not use in the inversion and their displacements are simulated by forward modeling.

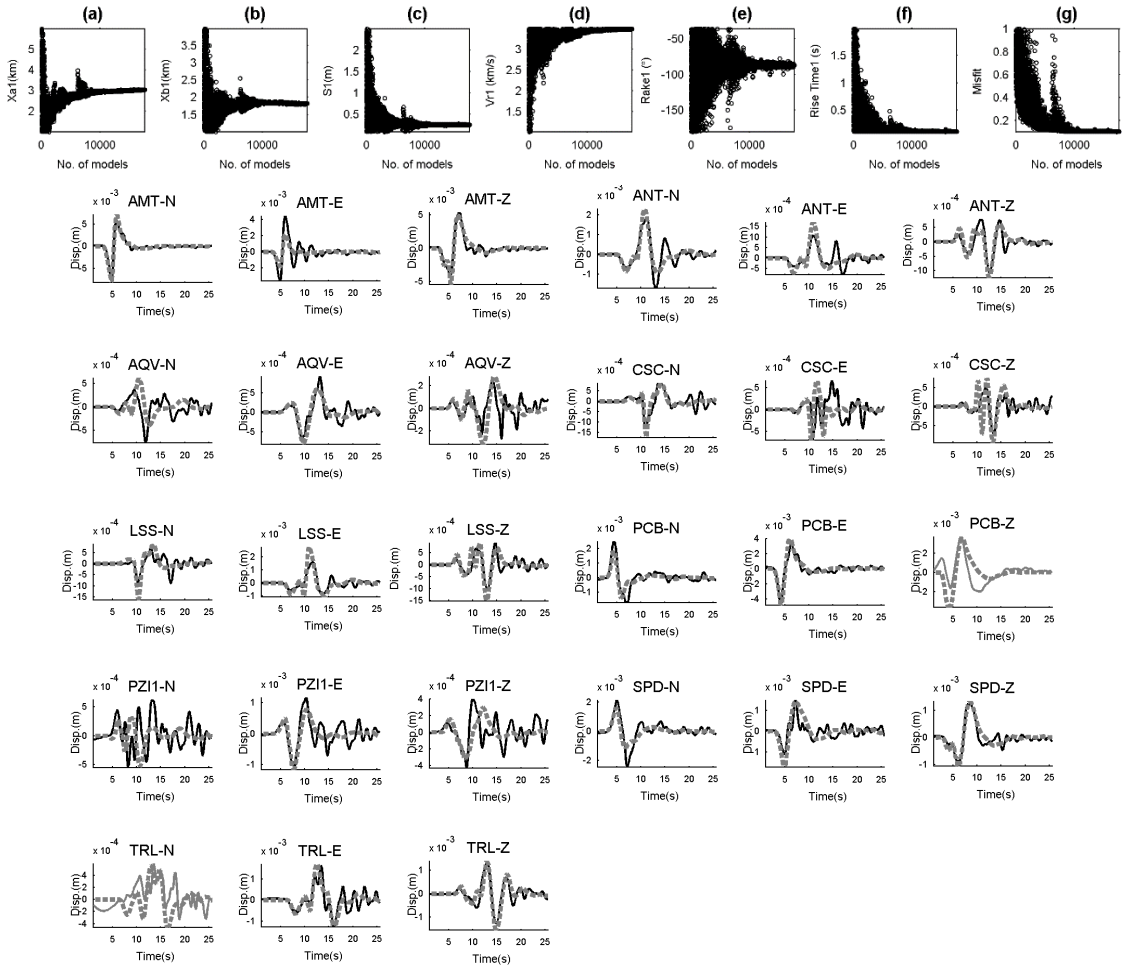

Figure Sb44. A) Convergence of model#4 source parameters obtained for the ML5.4 09:25:40 (GMT) event. b) Waveform fit of the model#4. Black and gray are real and synthetics, respectively. Gray solid lines did not use in the inversion and their displacements are simulated by forward modeling.

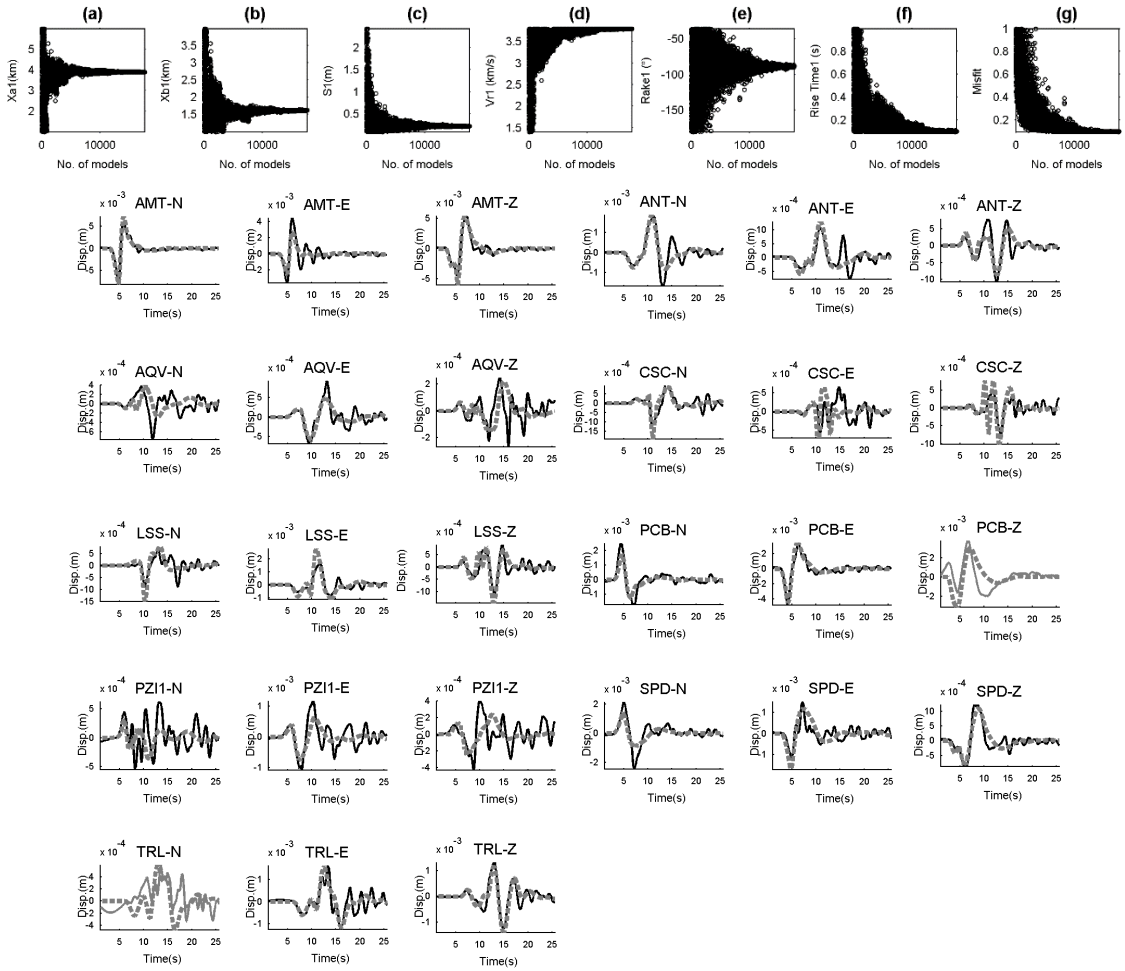

Figure Sb45. A) Convergence of model#5 source parameters obtained for the ML5.4 09:25:40 (GMT) event. b) Waveform fit of the model#5. Black and gray are real and synthetics, respectively. Gray solid lines did not use in the inversion and their displacements are simulated by forward modeling.

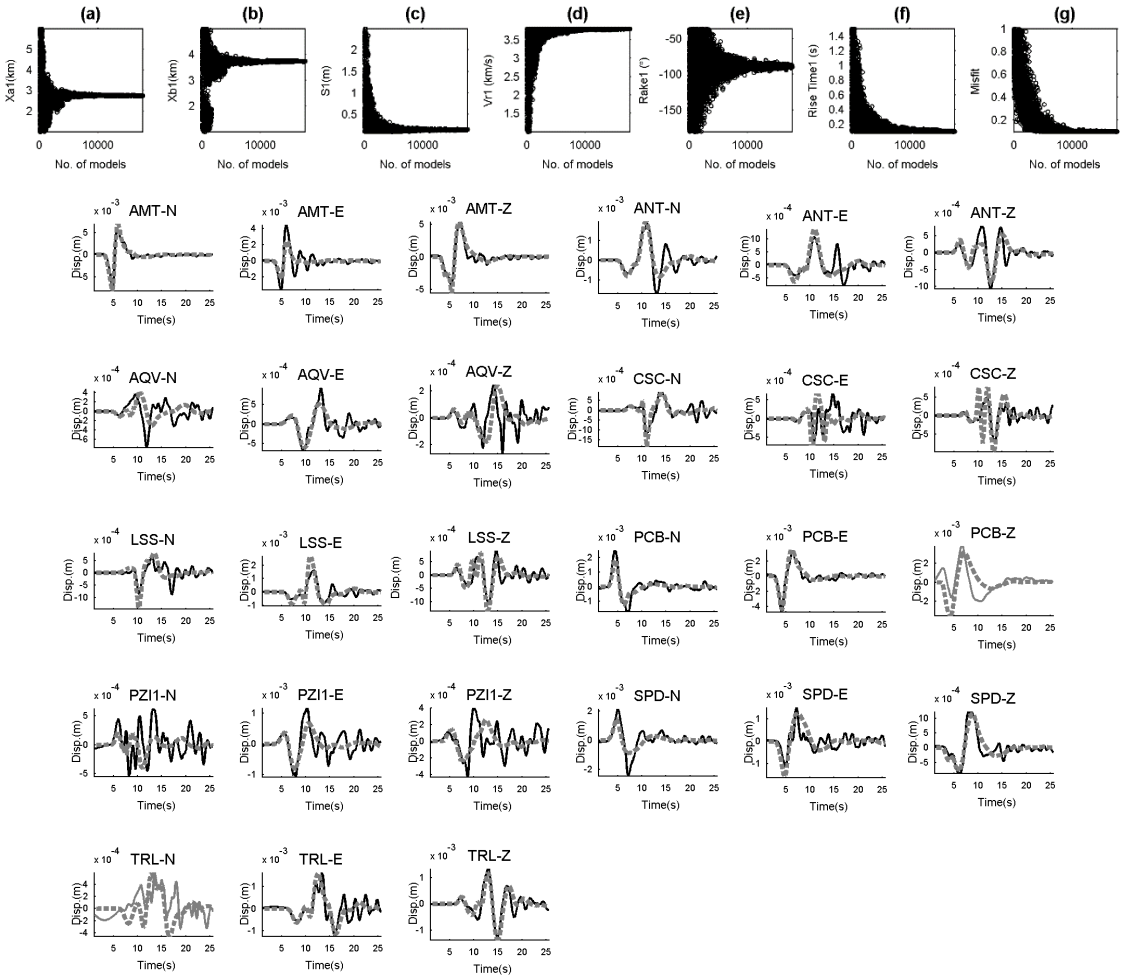

Figure Sb46. A) Convergence of model#6 source parameters obtained for the ML5.4 09:25:40 (GMT) event. b) Waveform fit of the model#6. Black and gray are real and synthetics, respectively. Gray solid lines did not use in the inversion and their displacements are simulated by forward modeling.

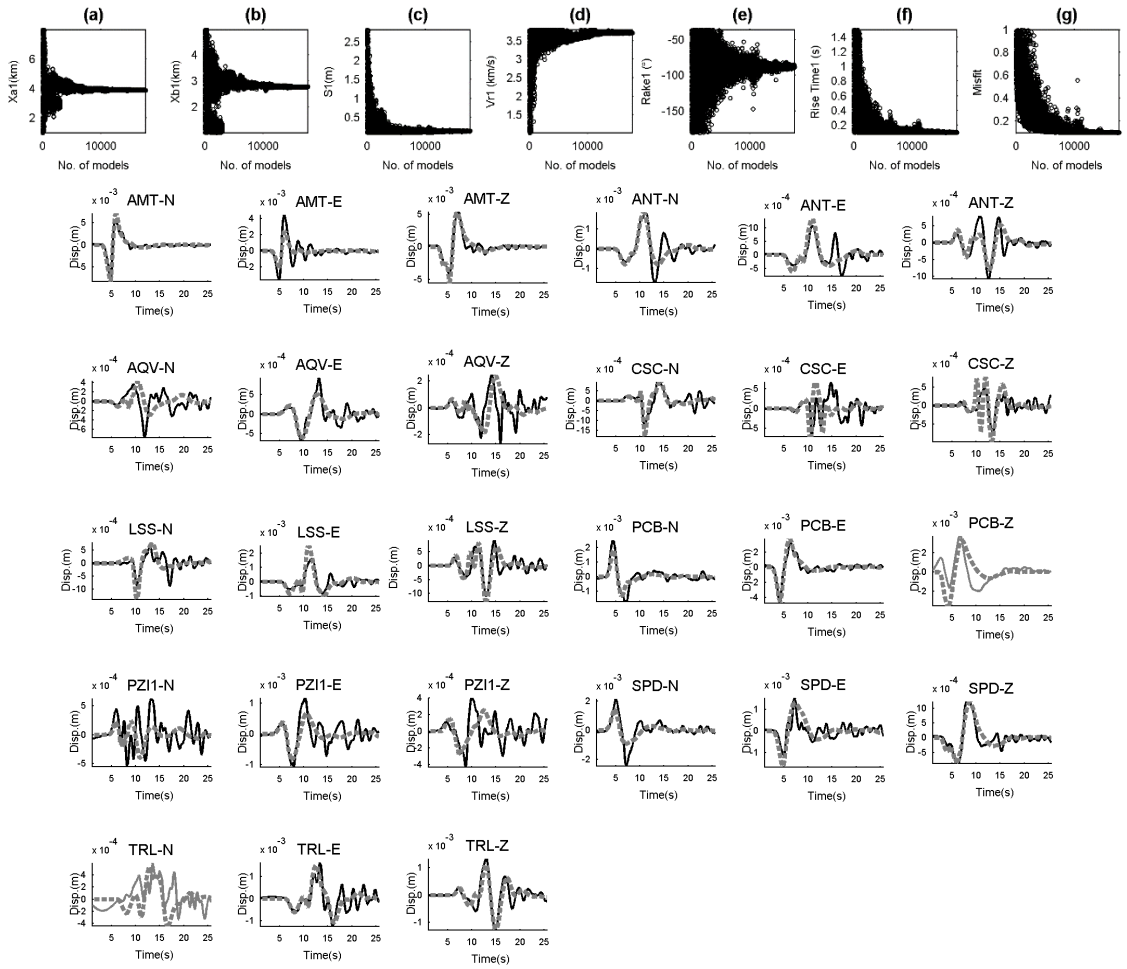

Figure Sb47. A) Convergence of model#7 source parameters obtained for the ML5.4 09:25:40 (GMT) event. b) Waveform fit of the model#7. Black and gray are real and synthetics, respectively. Gray solid lines did not use in the inversion and their displacements are simulated by forward modeling.

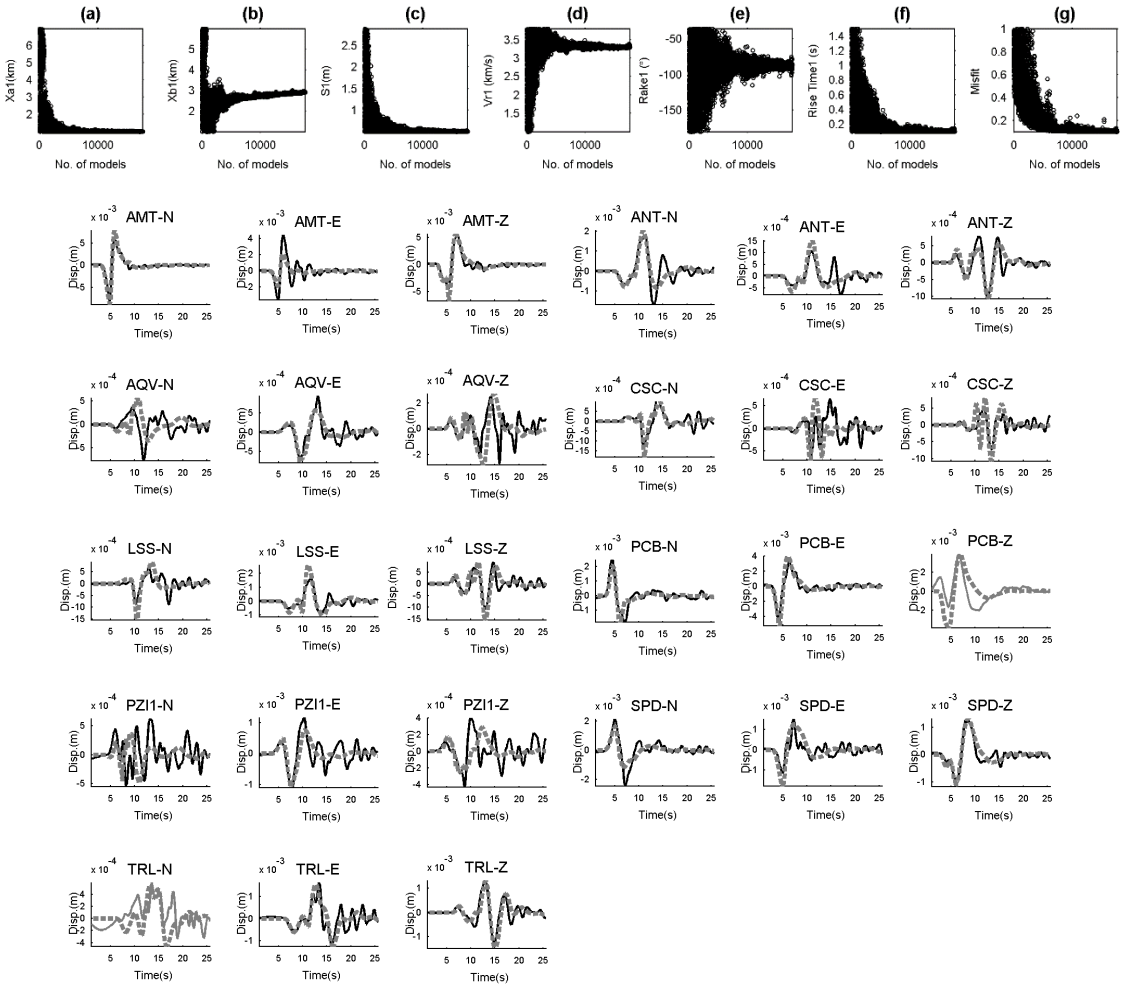

Figure Sb48. A) Convergence of model#8 source parameters obtained for the ML5.4 09:25:40 (GMT) event. b) Waveform fit of the model#8. Black and gray are real and synthetics, respectively. Gray solid lines did not use in the inversion and their displacements are simulated by forward modeling.

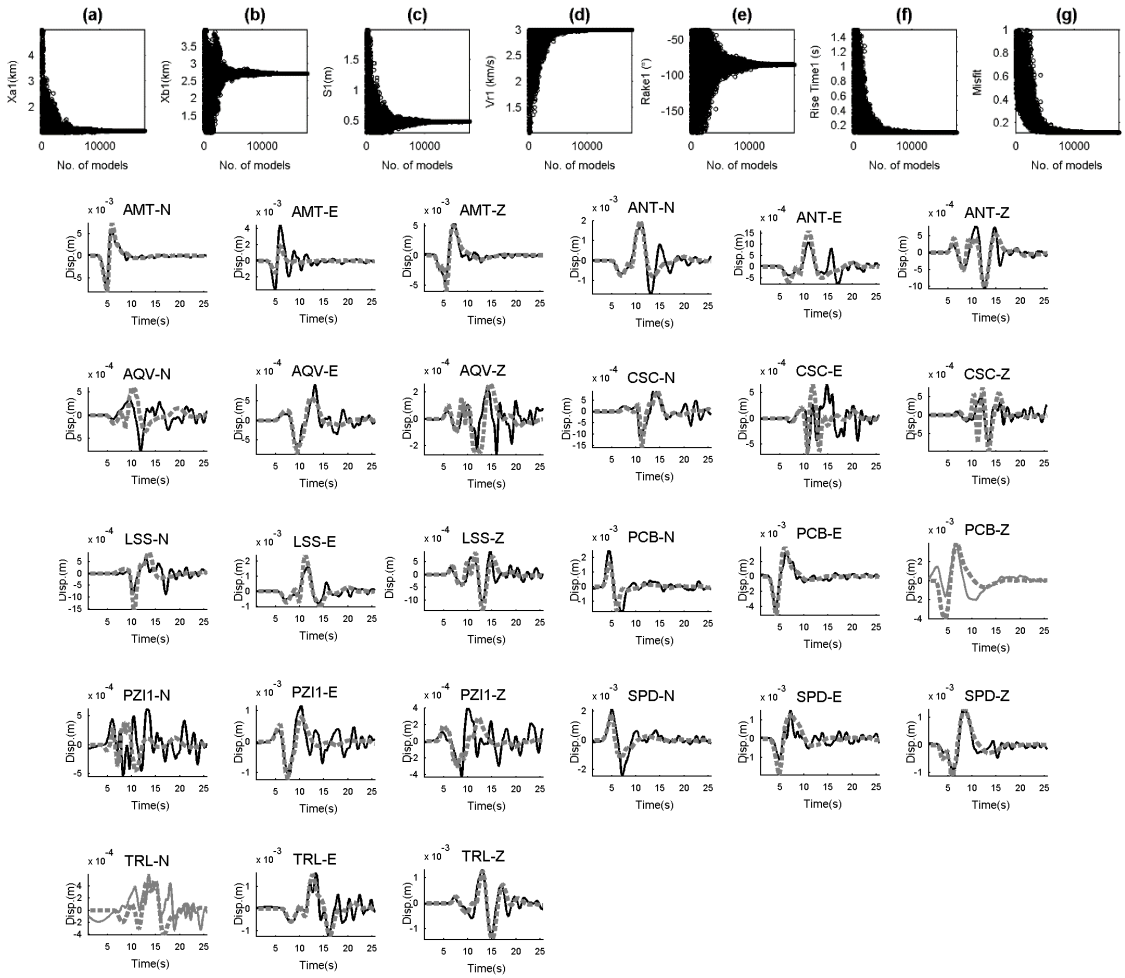

Figure Sb49. A) Convergence of model#9 source parameters obtained for the ML5.4 09:25:40 (GMT) event. b) Waveform fit of the model#9. Black and gray are real and synthetics, respectively. Gray solid lines did not use in the inversion and their displacements are simulated by forward modeling.

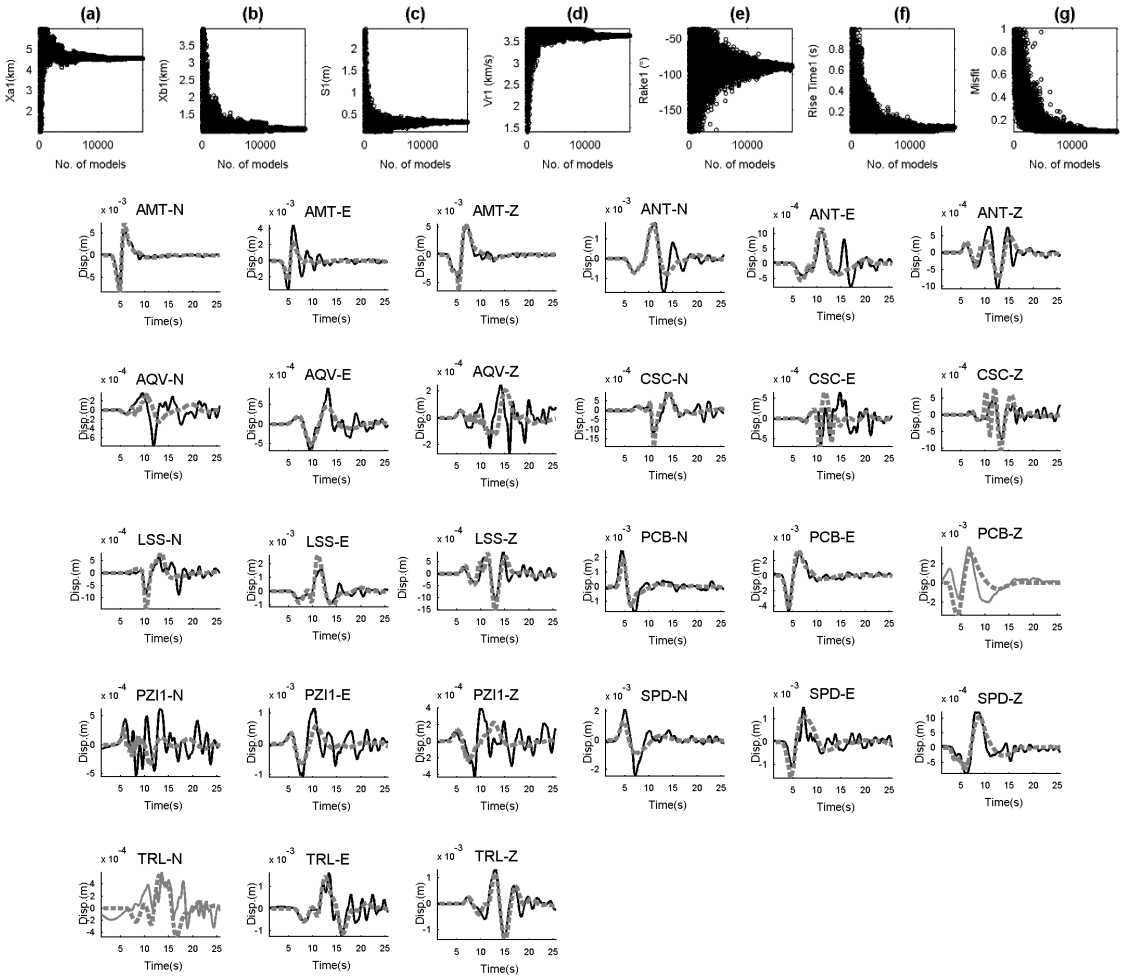

Figure Sb50. A) Convergence of model#10 source parameters obtained for the ML5.4 09:25:40 (GMT) event. b) Waveform fit of the model#10. Black and gray are real and synthetics, respectively. Gray solid lines did not use in the inversion and their displacements are simulated by forward modeling.

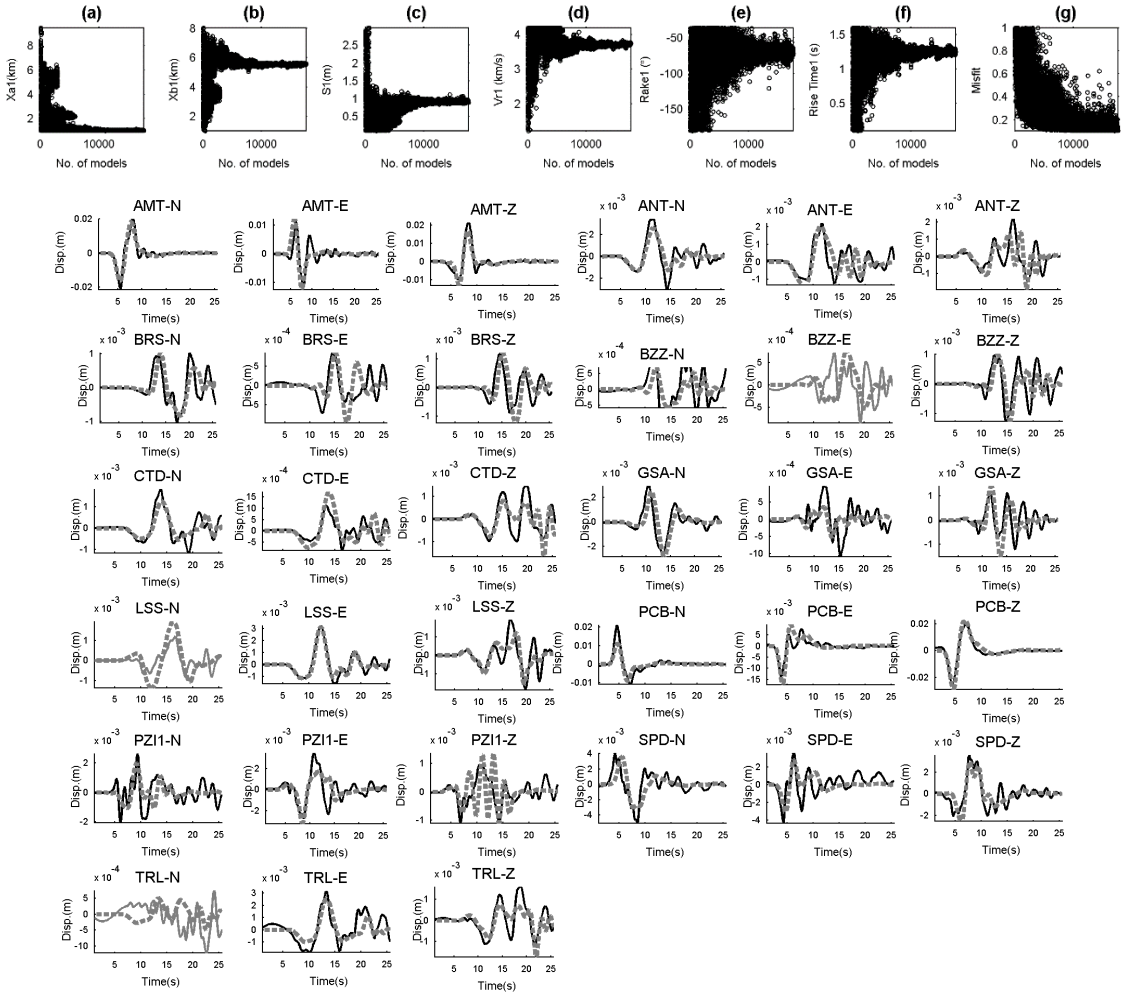

Figure Sb51. A) Convergence of model#1 source parameters obtained for the ML5.4 10:14:10 (GMT) event. b) Waveform fit of the model#1. Black and gray are real and synthetics, respectively. Gray solid lines did not use in the inversion and their displacements are simulated by forward modeling.

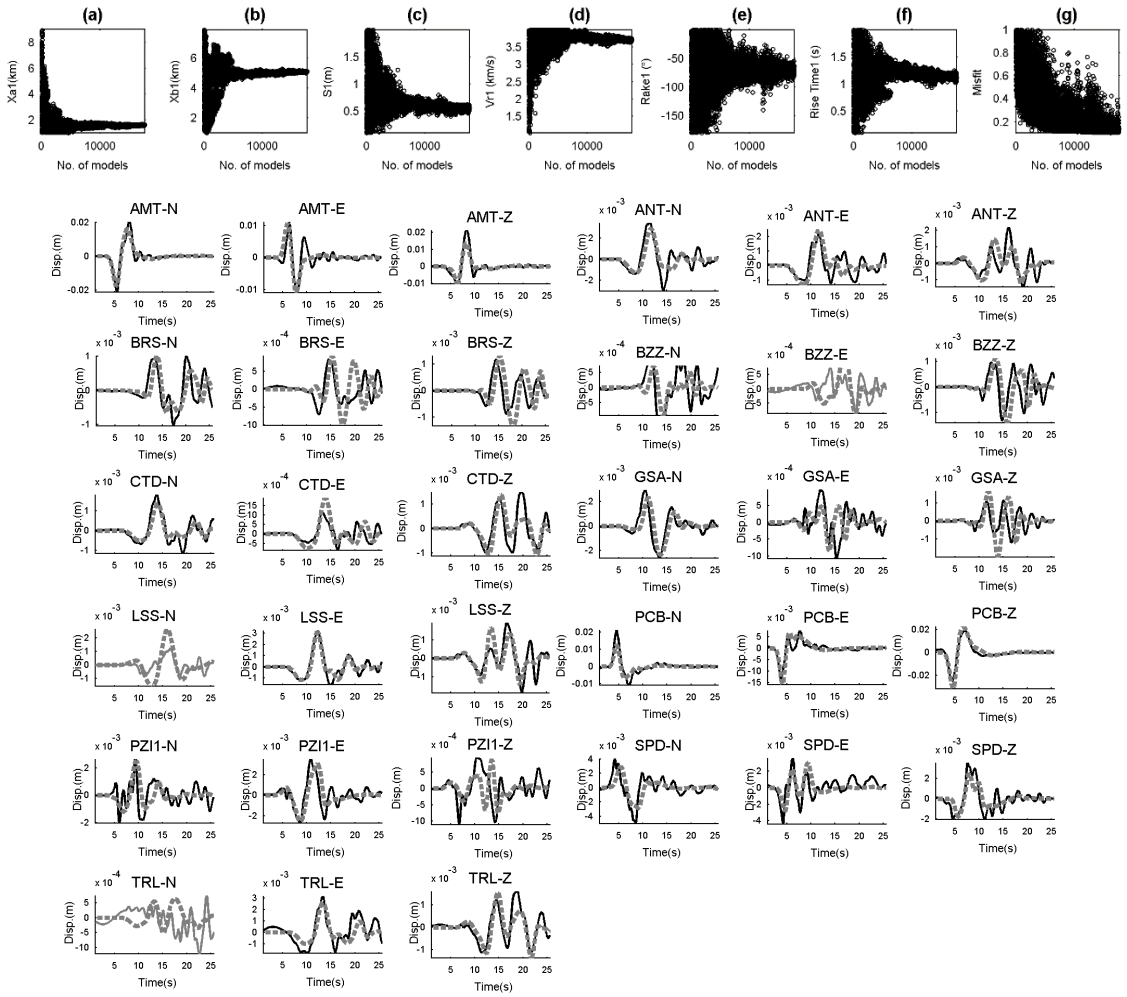

Figure Sb52. A) Convergence of model#2 source parameters obtained for the ML5.4 10:14:10 (GMT) event. b) Waveform fit of the model#2. Black and gray are real and synthetics, respectively. Gray solid lines did not use in the inversion and their displacements are simulated by forward modeling.

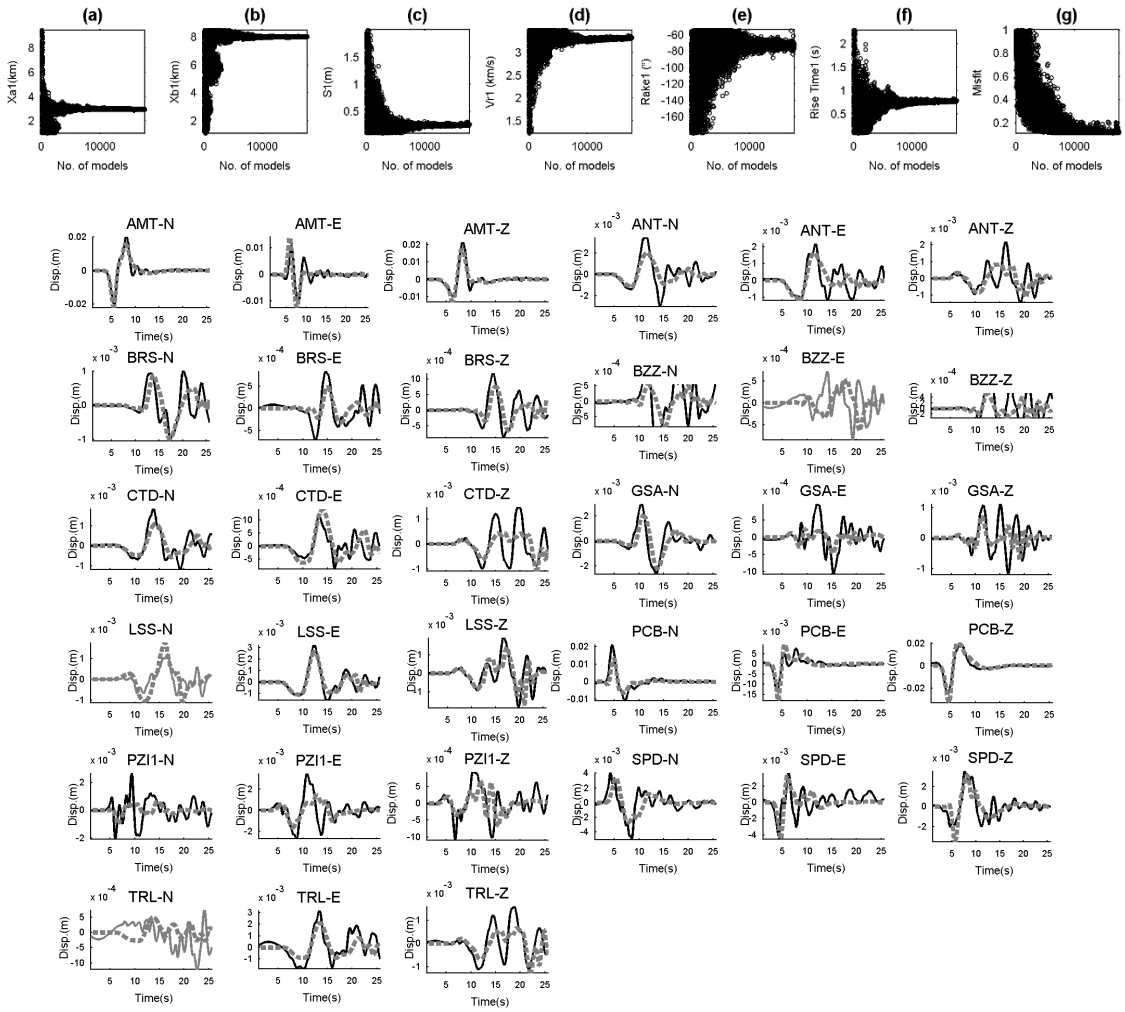

Figure Sb53. A) Convergence of model#3 source parameters obtained for the ML5.4 10:14:10 (GMT) event. b) Waveform fit of the model#3. Black and gray are real and synthetics, respectively. Gray solid lines did not use in the inversion and their displacements are simulated by forward modeling.

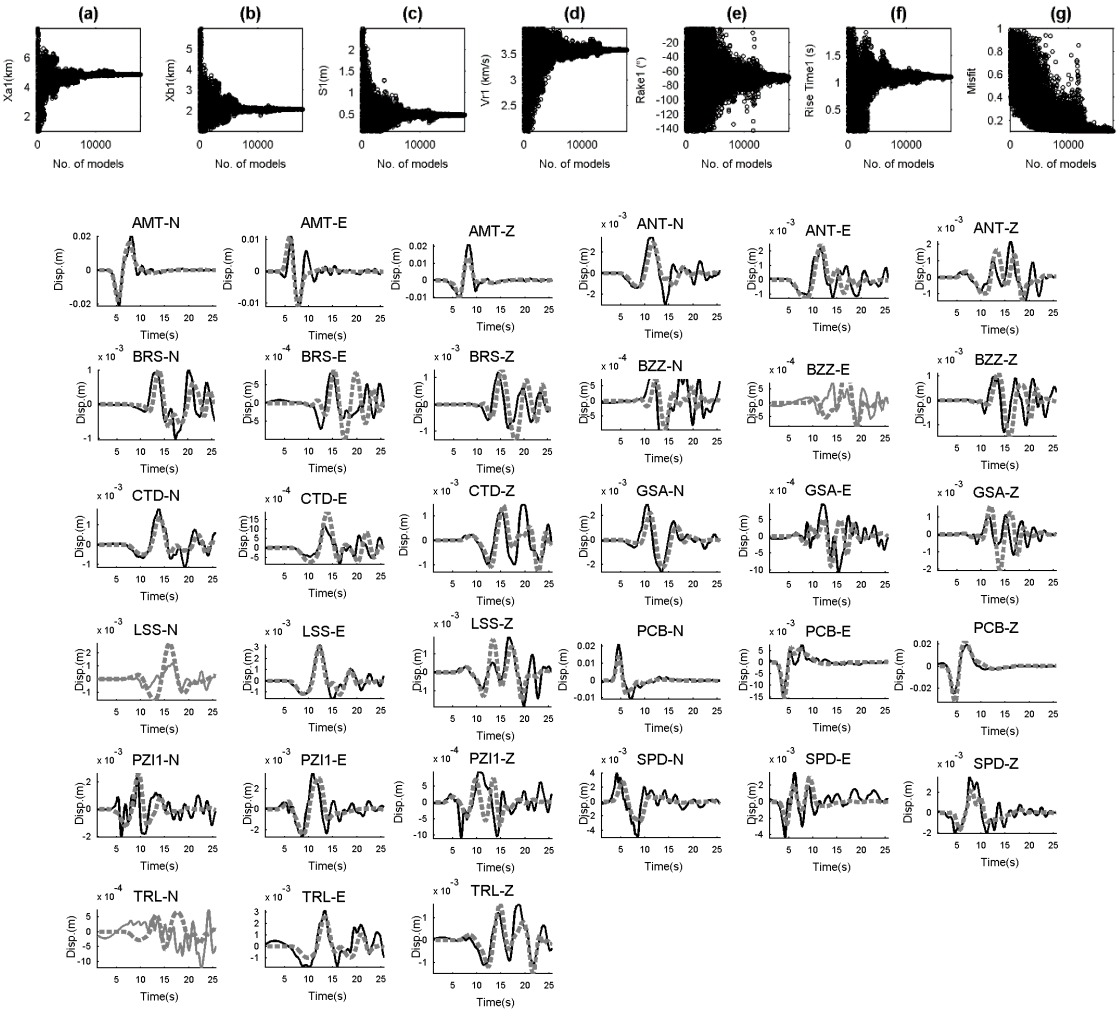

Figure Sb54. A) Convergence of model#4 source parameters obtained for the ML5.4 10:14:10 (GMT) event. b) Waveform fit of the model#4. Black and gray are real and synthetics, respectively. Gray solid lines did not use in the inversion and their displacements are simulated by forward modeling.

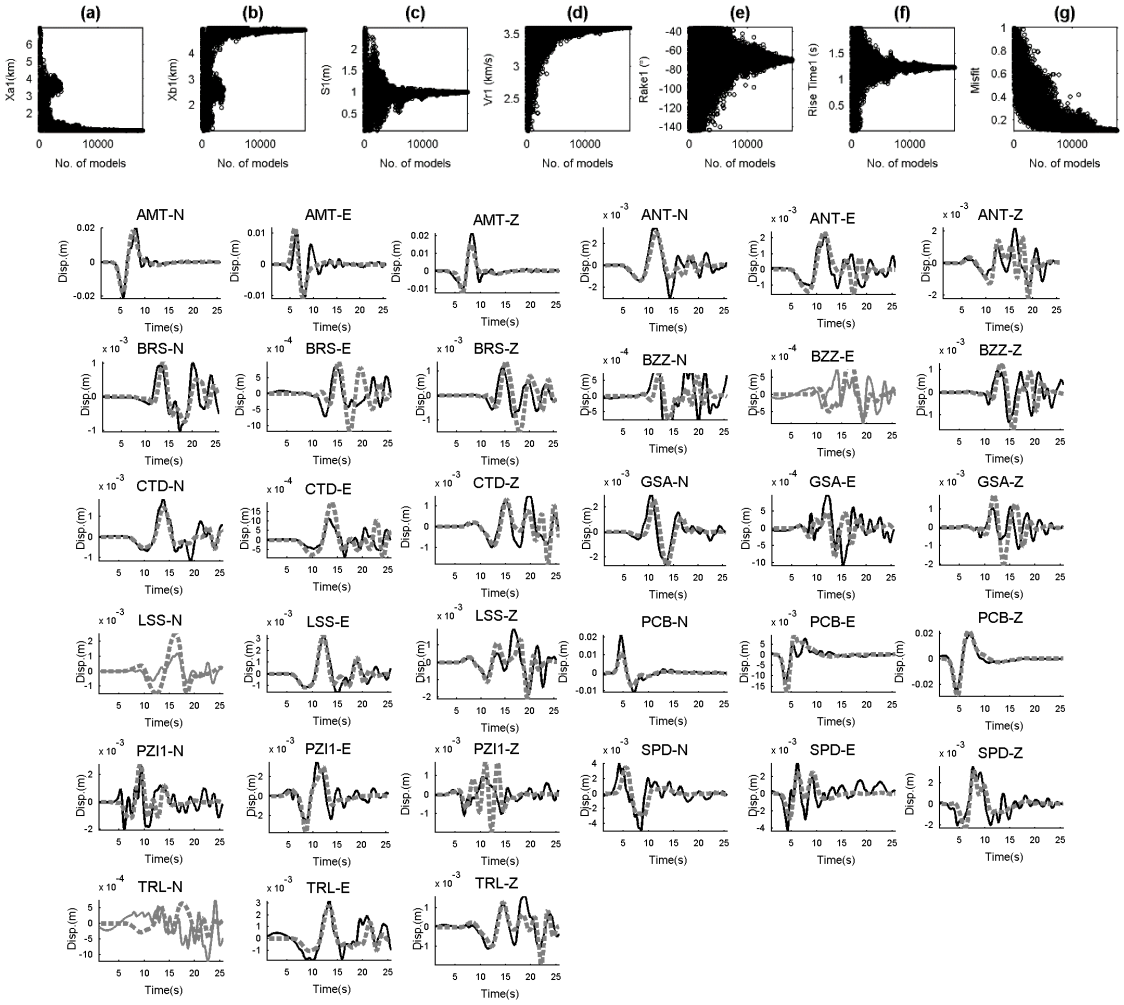

Figure Sb55. A) Convergence of model#5 source parameters obtained for the ML5.4 10:14:10 (GMT) event. b) Waveform fit of the model#5. Black and gray are real and synthetics, respectively. Gray solid lines did not use in the inversion and their displacements are simulated by forward modeling.

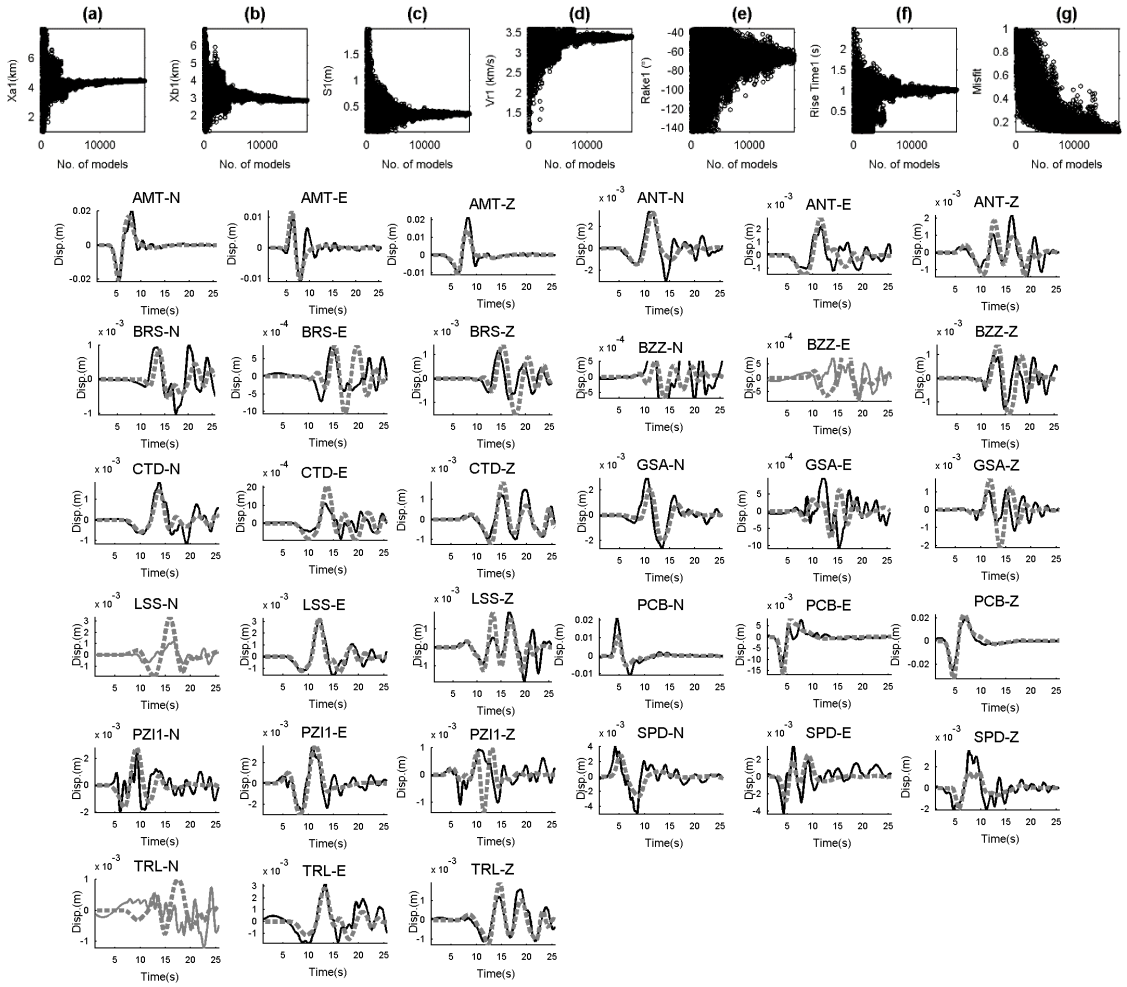

Figure Sb56. A) Convergence of model#6 source parameters obtained for the ML5.4 10:14:10 (GMT) event. b) Waveform fit of the model#6. Black and gray are real and synthetics, respectively. Gray solid lines did not use in the inversion and their displacements are simulated by forward modeling.

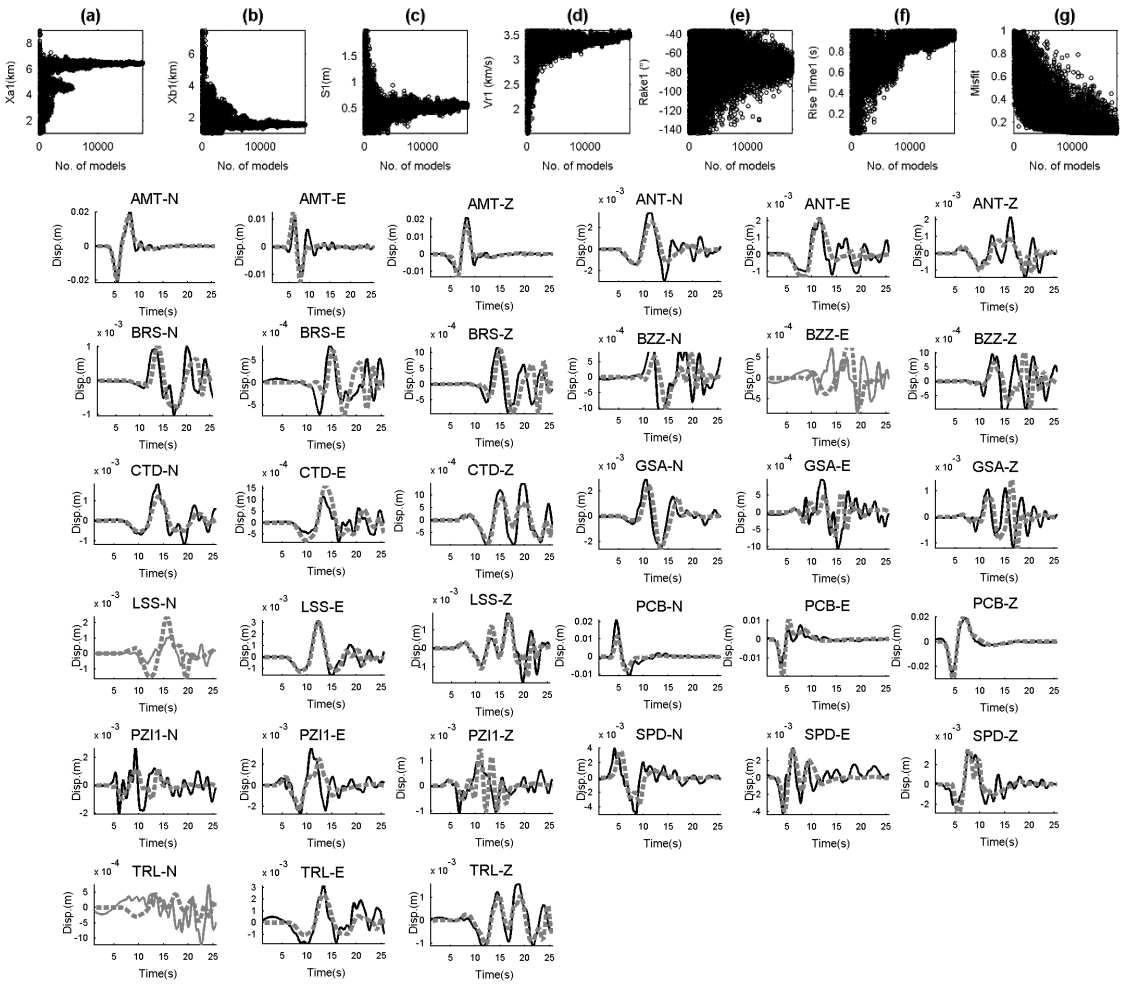

Figure Sb57. A) Convergence of model#7 source parameters obtained for the ML5.4 10:14:10 (GMT) event. b) Waveform fit of the model#7. Black and gray are real and synthetics, respectively. Gray solid lines did not use in the inversion and their displacements are simulated by forward modeling.

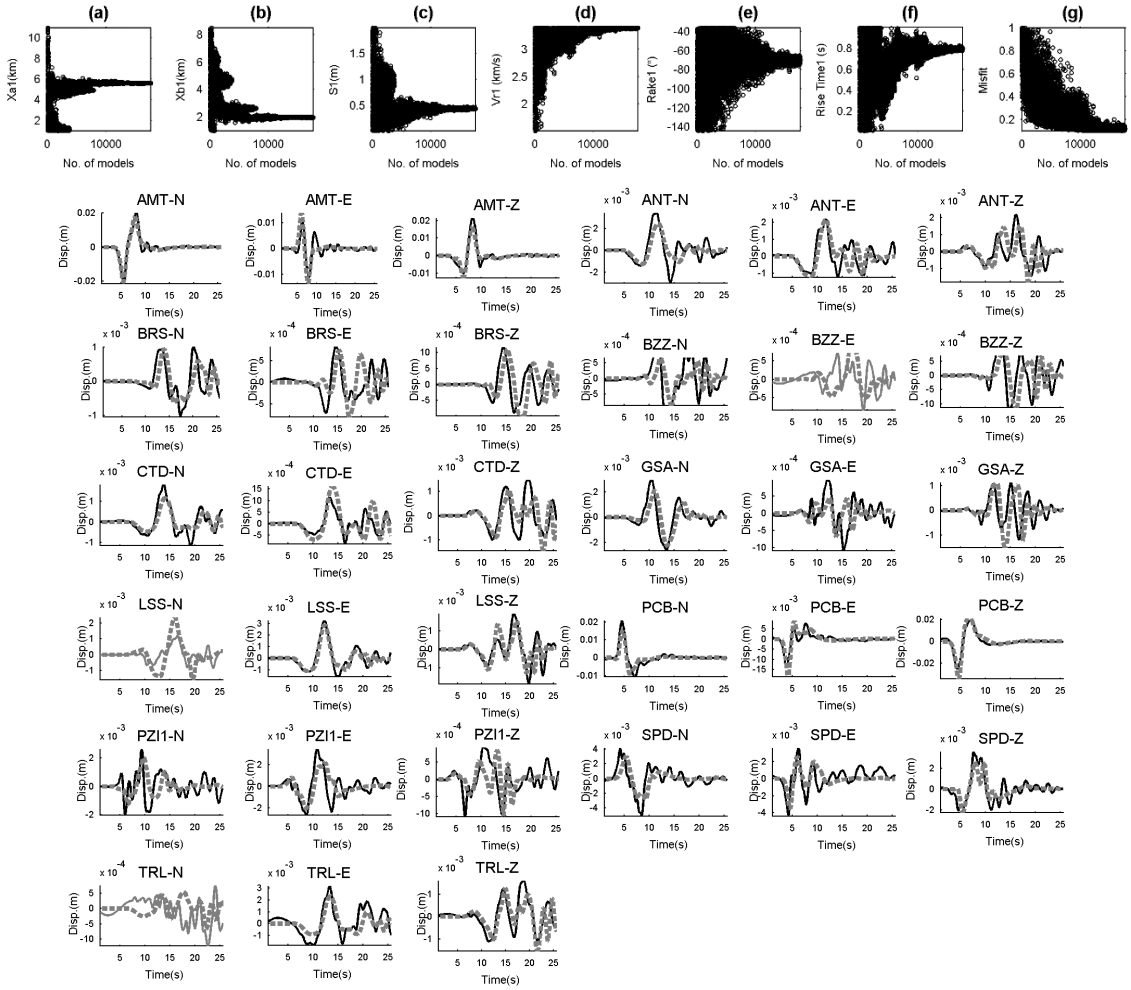

Figure Sb58. A) Convergence of model#8 source parameters obtained for the ML5.4 10:14:10 (GMT) event. b) Waveform fit of the model#8. Black and gray are real and synthetics, respectively. Gray solid lines did not use in the inversion and their displacements are simulated by forward modeling.

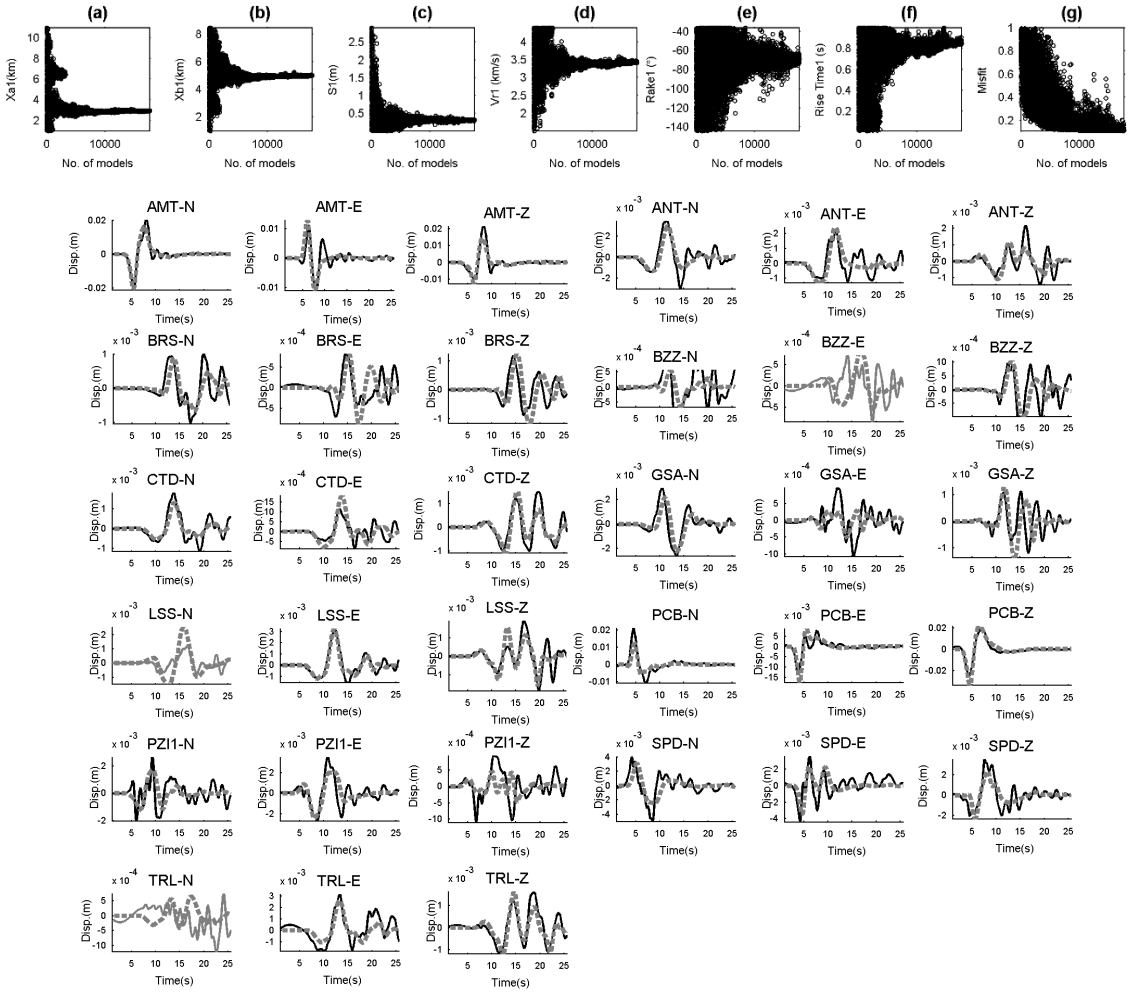

Figure Sb59. A) Convergence of model#9 source parameters obtained for the ML5.4 10:14:10 (GMT) event. b) Waveform fit of the model#9. Black and gray are real and synthetics, respectively. Gray solid lines did not use in the inversion and their displacements are simulated by forward modeling.

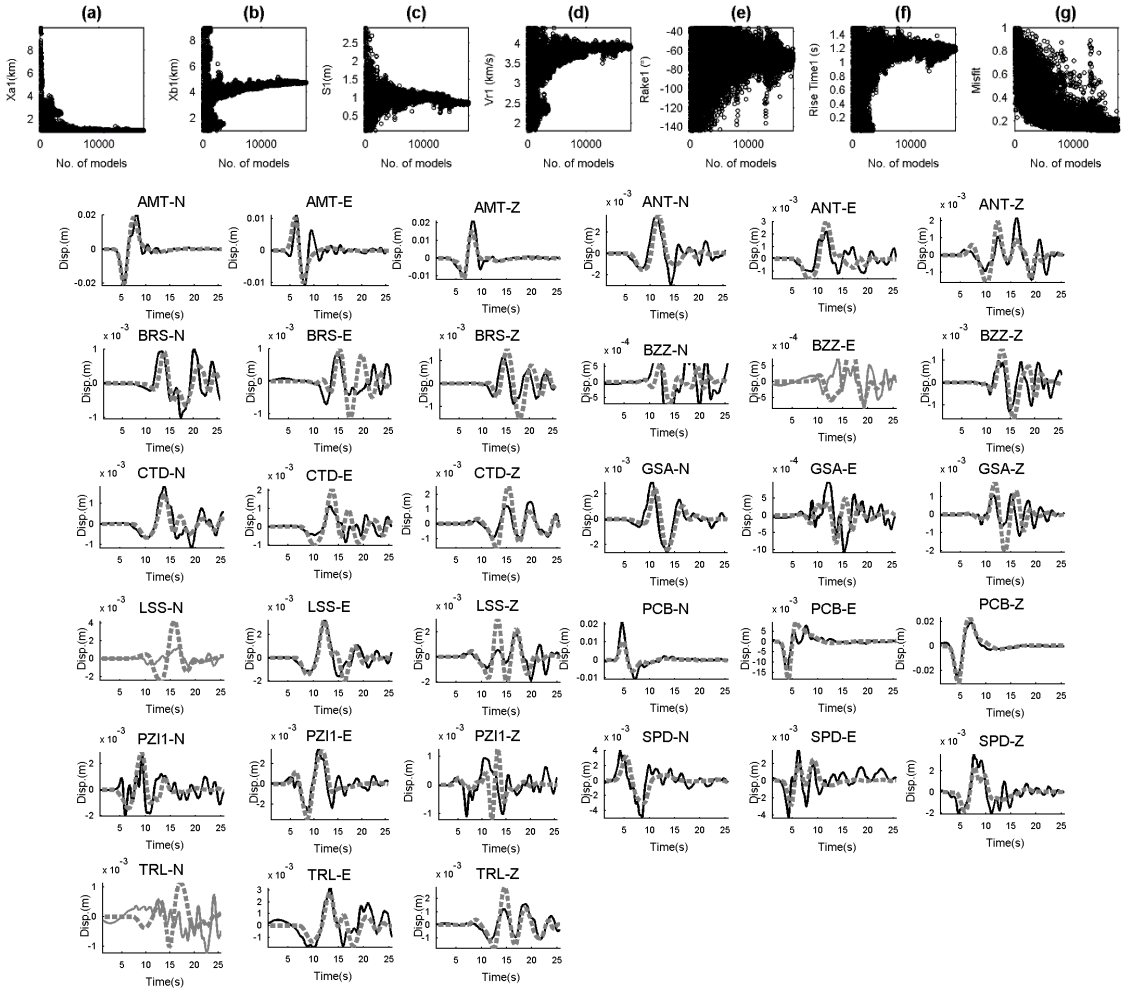

Figure Sb60. A) Convergence of model#10 source parameters obtained for the ML5.4 10:14:10 (GMT) event. b) Waveform fit of the model#10. Black and gray are real and synthetics, respectively. Gray solid lines did not use in the inversion and their displacements are simulated by forward modeling.

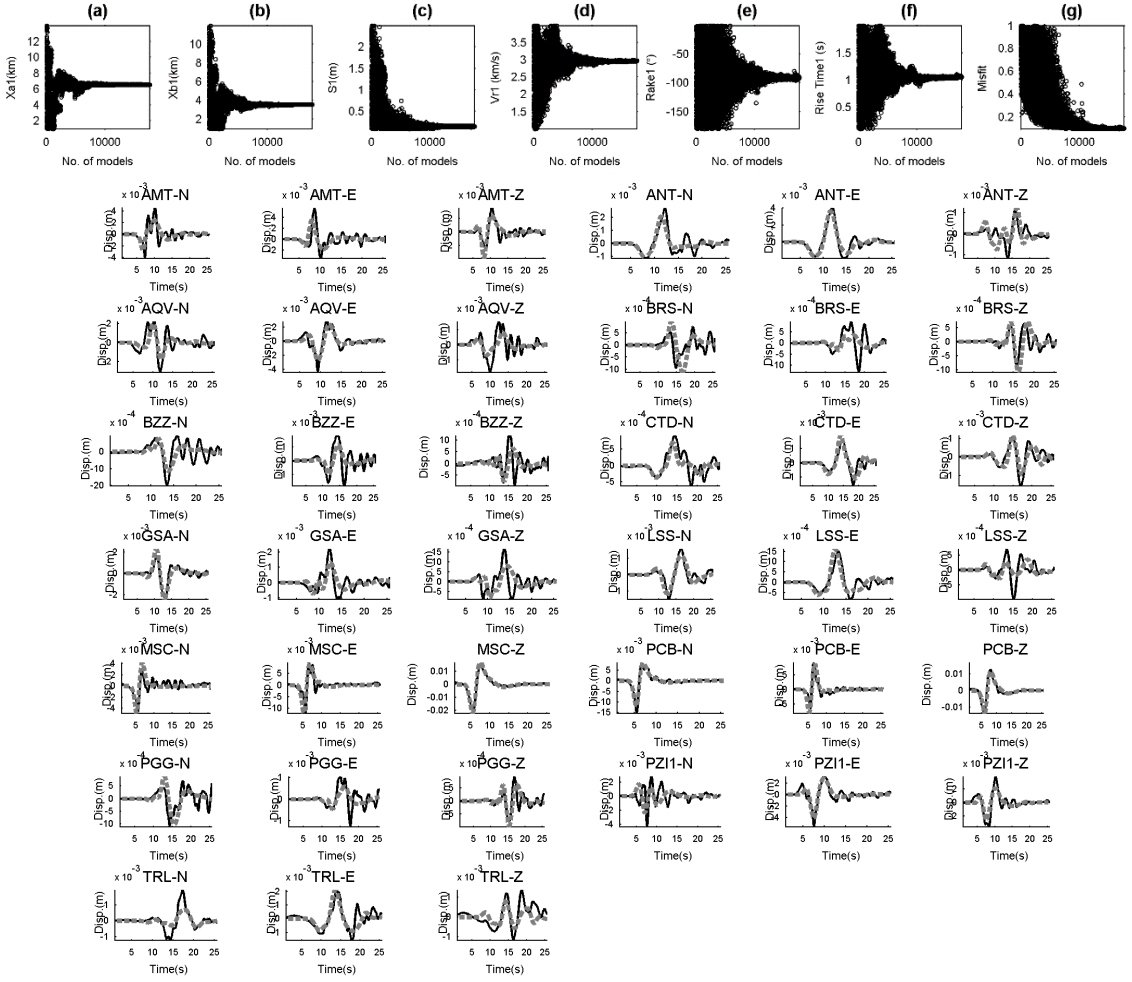

Figure Sb61. A) Convergence of model#1 source parameters obtained for the ML5.3 10:25:24 (GMT) event. b) Waveform fit of the model#1. Black and gray are real and synthetics, respectively.

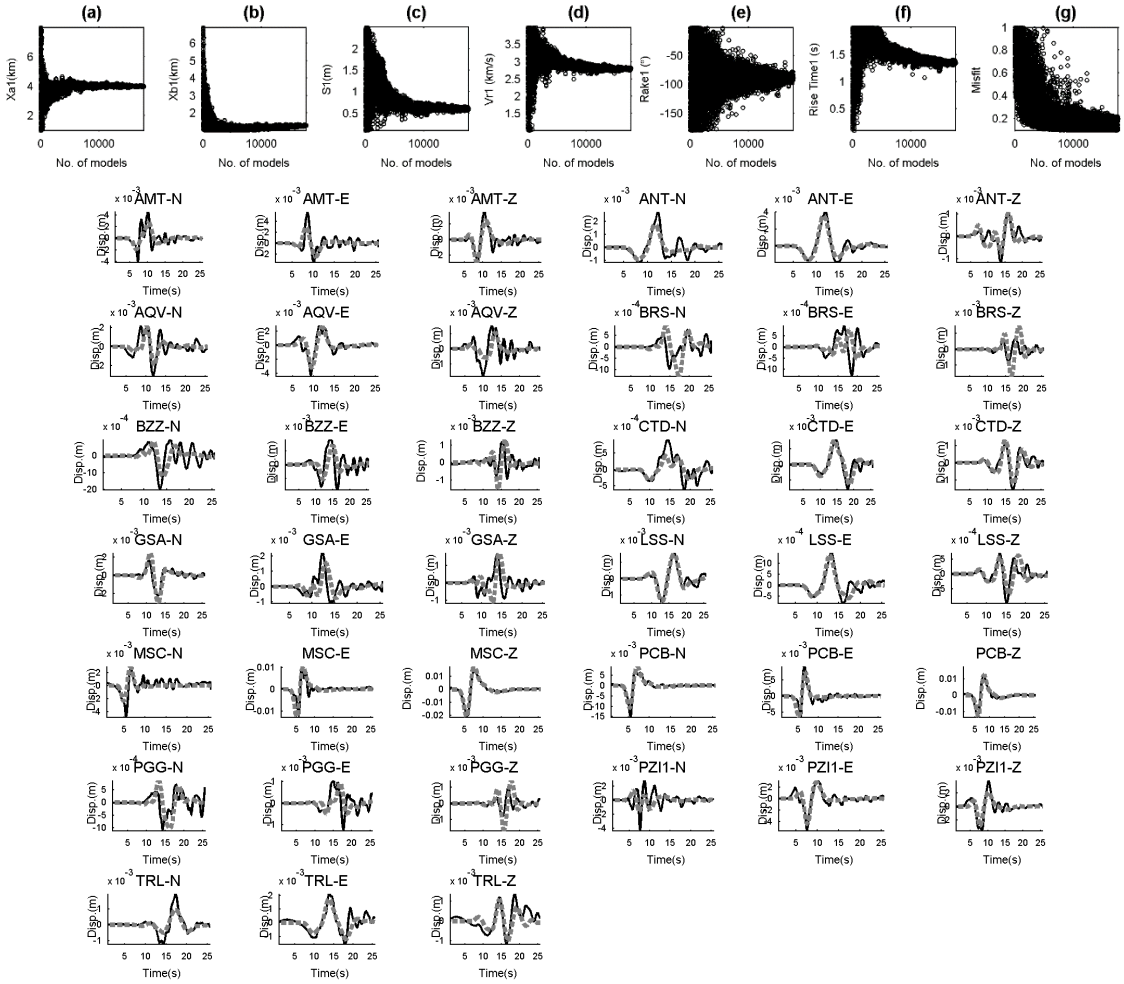

Figure Sb62. A) Convergence of model#2 source parameters obtained for the ML5.3 10:25:24 (GMT) event. b) Waveform fit of the model#2. Black and gray are real and synthetics, respectively.

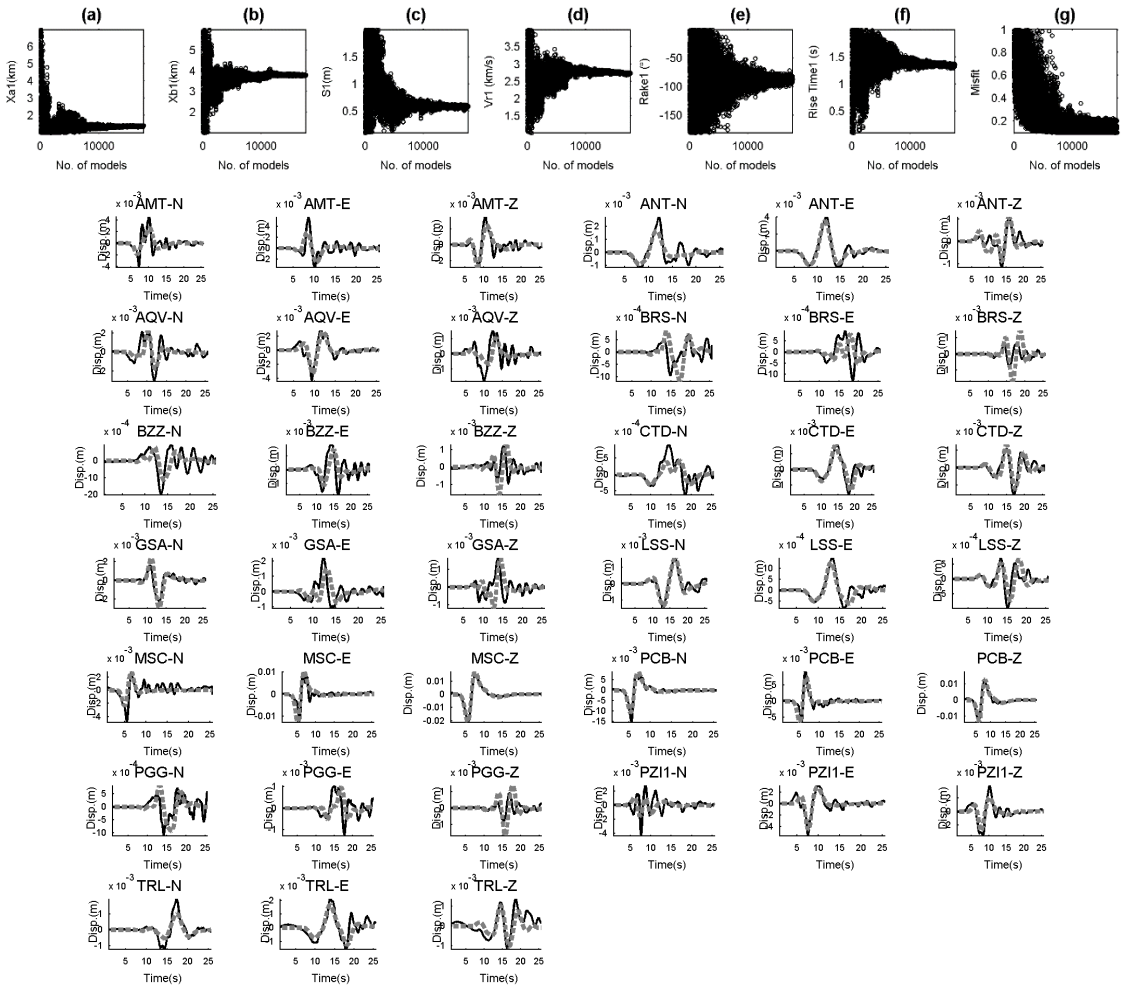

Figure Sb63. A) Convergence of model#3 source parameters obtained for the ML5.3 10:25:24 (GMT) event. b) Waveform fit of the model#3. Black and gray are real and synthetics, respectively.

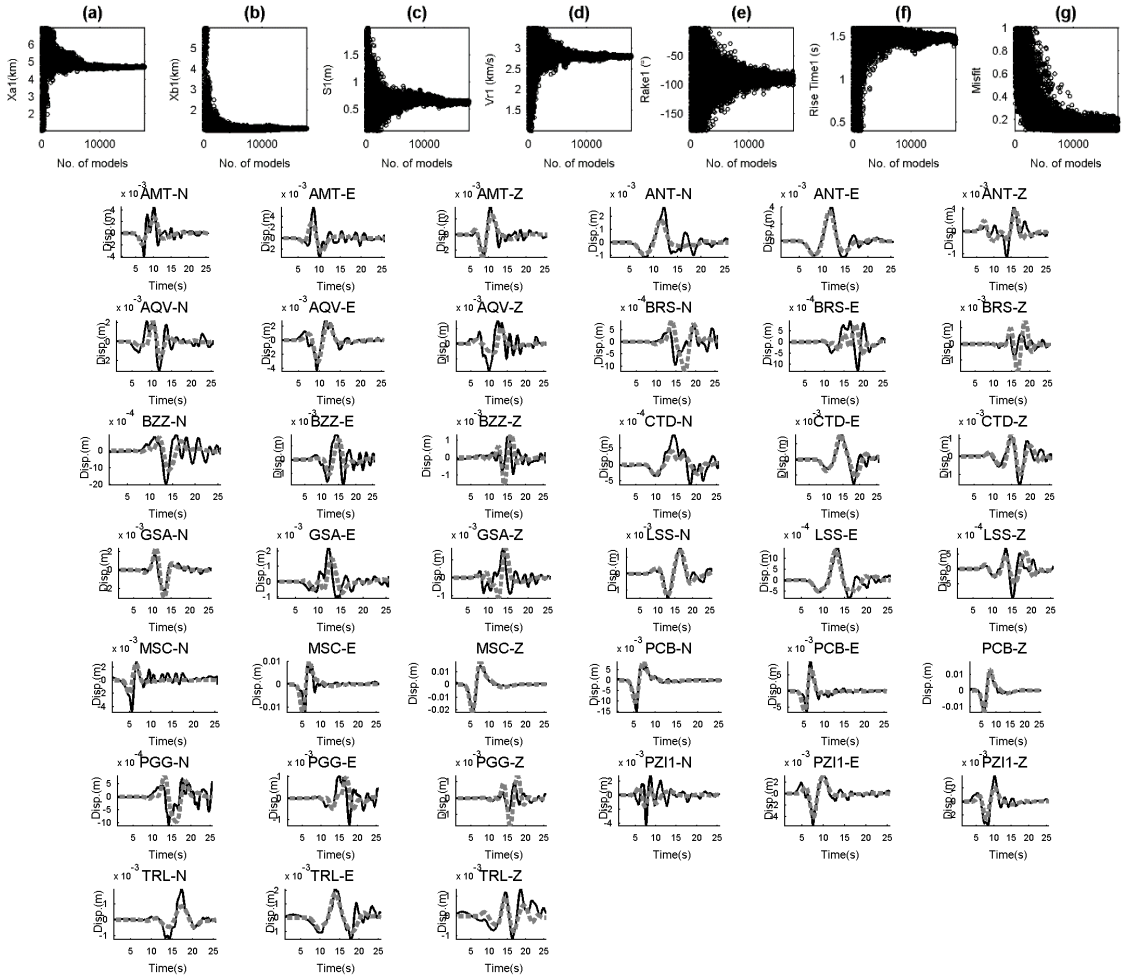

Figure Sb64. A) Convergence of model#4 source parameters obtained for the ML5.3 10:25:24 (GMT) event. b) Waveform fit of the model#4. Black and gray are real and synthetics, respectively.

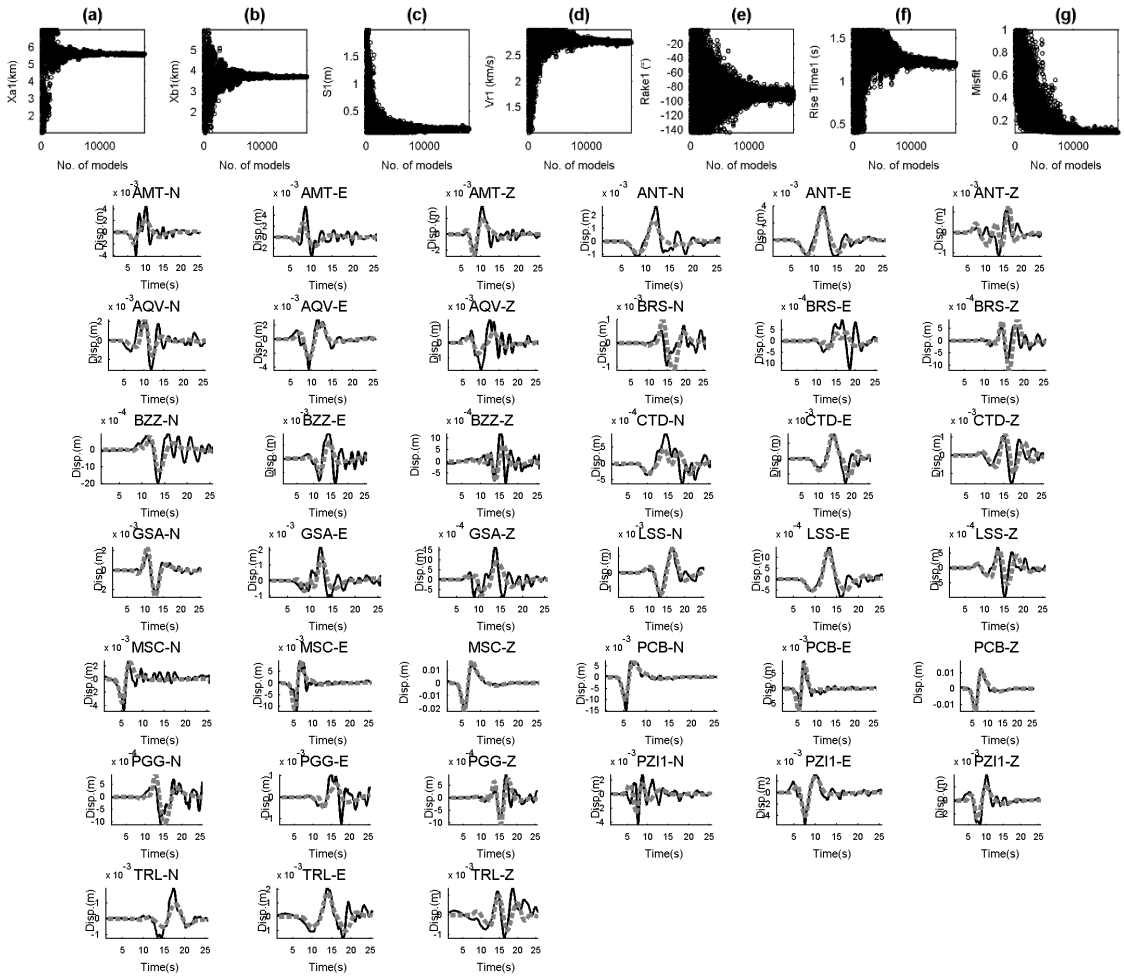

Figure Sb65. A) Convergence of model#5 source parameters obtained for the ML5.3 10:25:24 (GMT) event. b) Waveform fit of the model#5. Black and gray are real and synthetics, respectively.

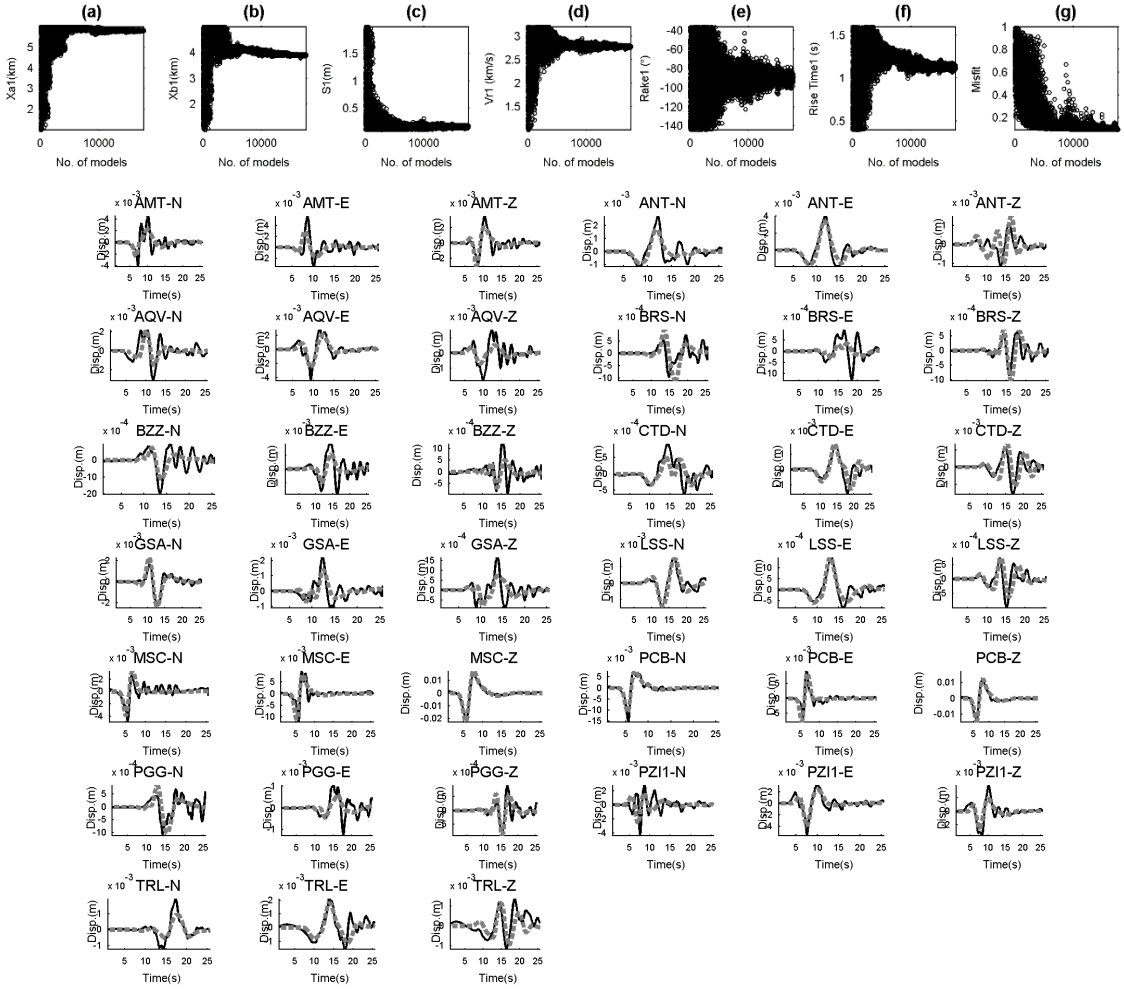

Figure Sb66. A) Convergence of model#6 source parameters obtained for the ML5.3 10:25:24 (GMT) event. b) Waveform fit of the model#6. Black and gray are real and synthetics, respectively.

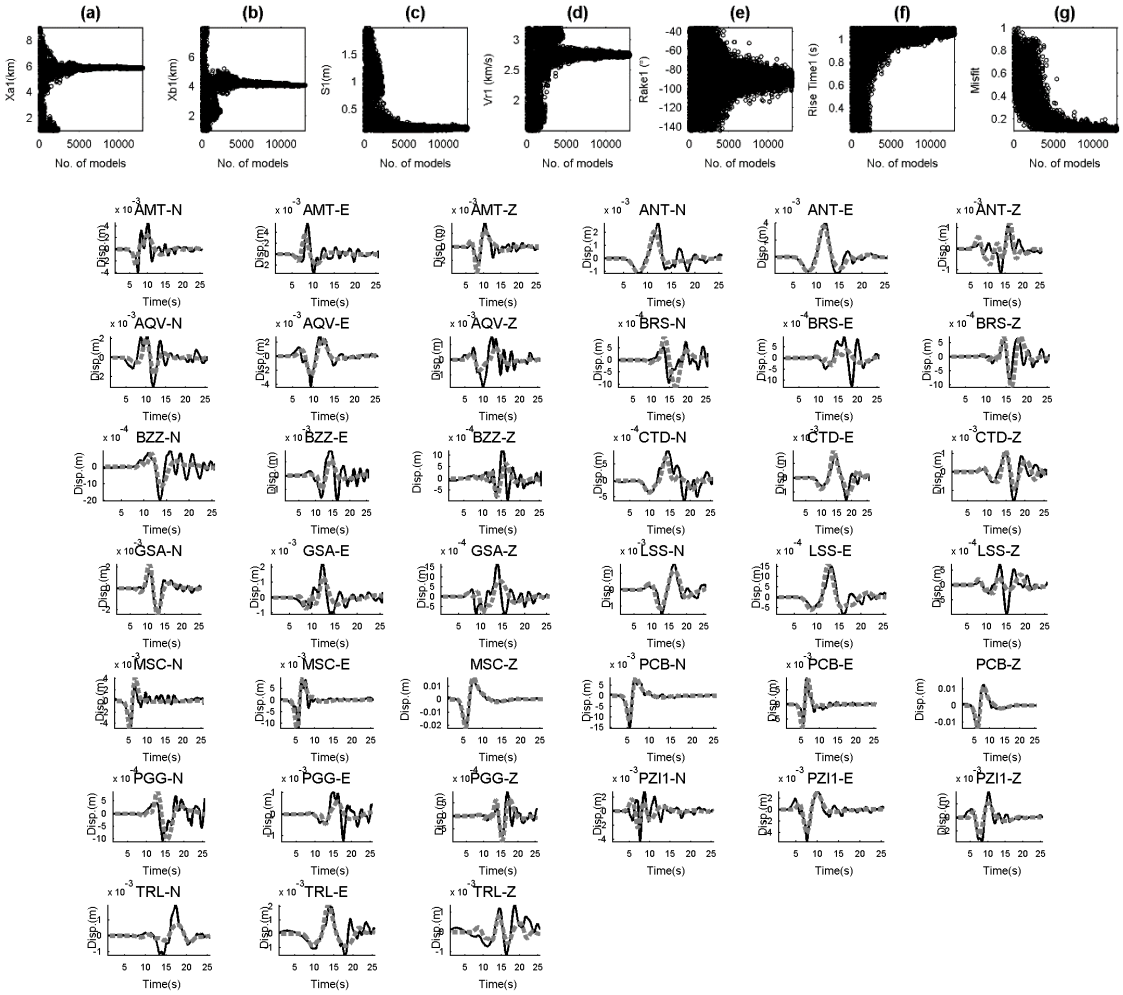

Figure Sb67. A) Convergence of model#7 source parameters obtained for the ML5.3 10:25:24 (GMT) event. b) Waveform fit of the model#7. Black and gray are real and synthetics, respectively.

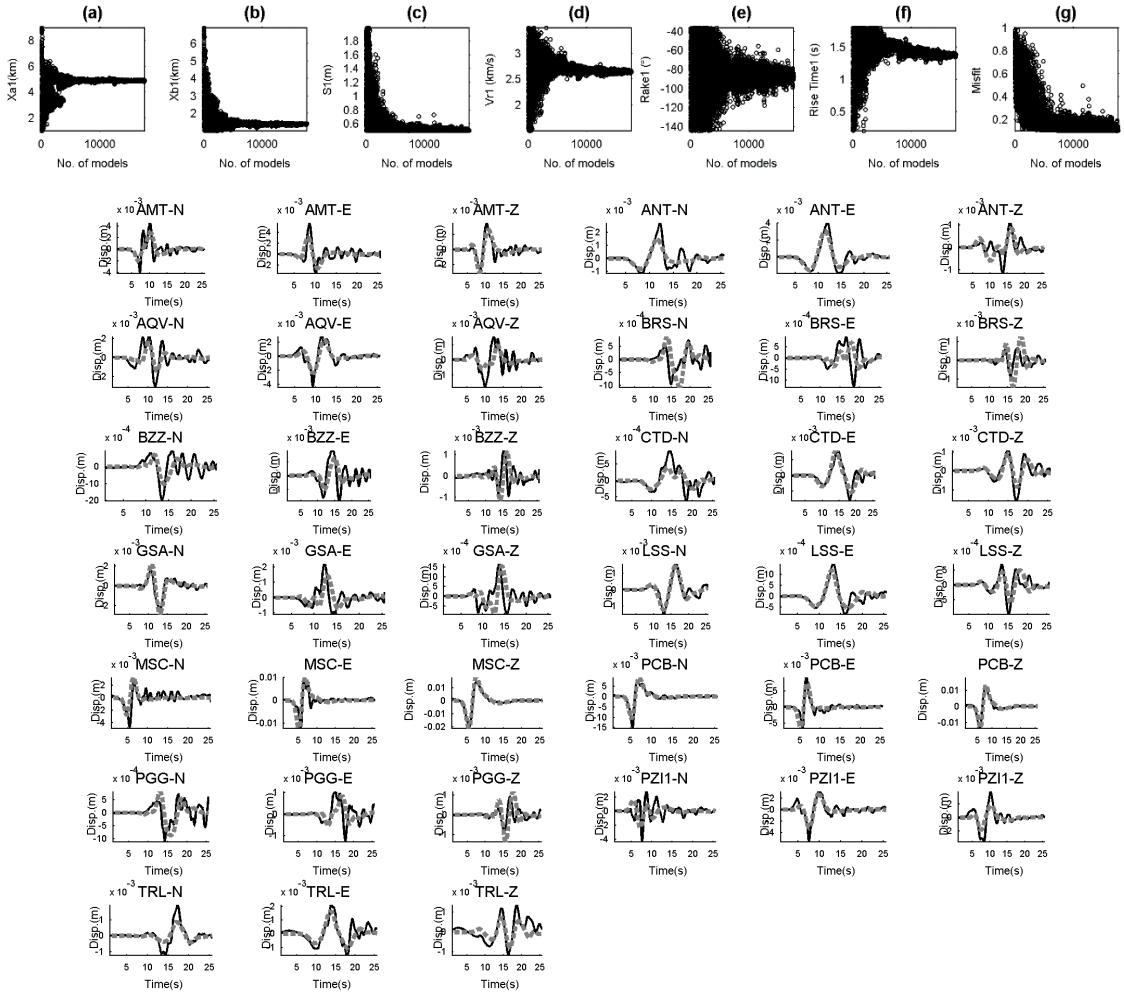

Figure Sb68. A) Convergence of model#8 source parameters obtained for the ML5.3 10:25:24 (GMT) event. b) Waveform fit of the model#8. Black and gray are real and synthetics, respectively.

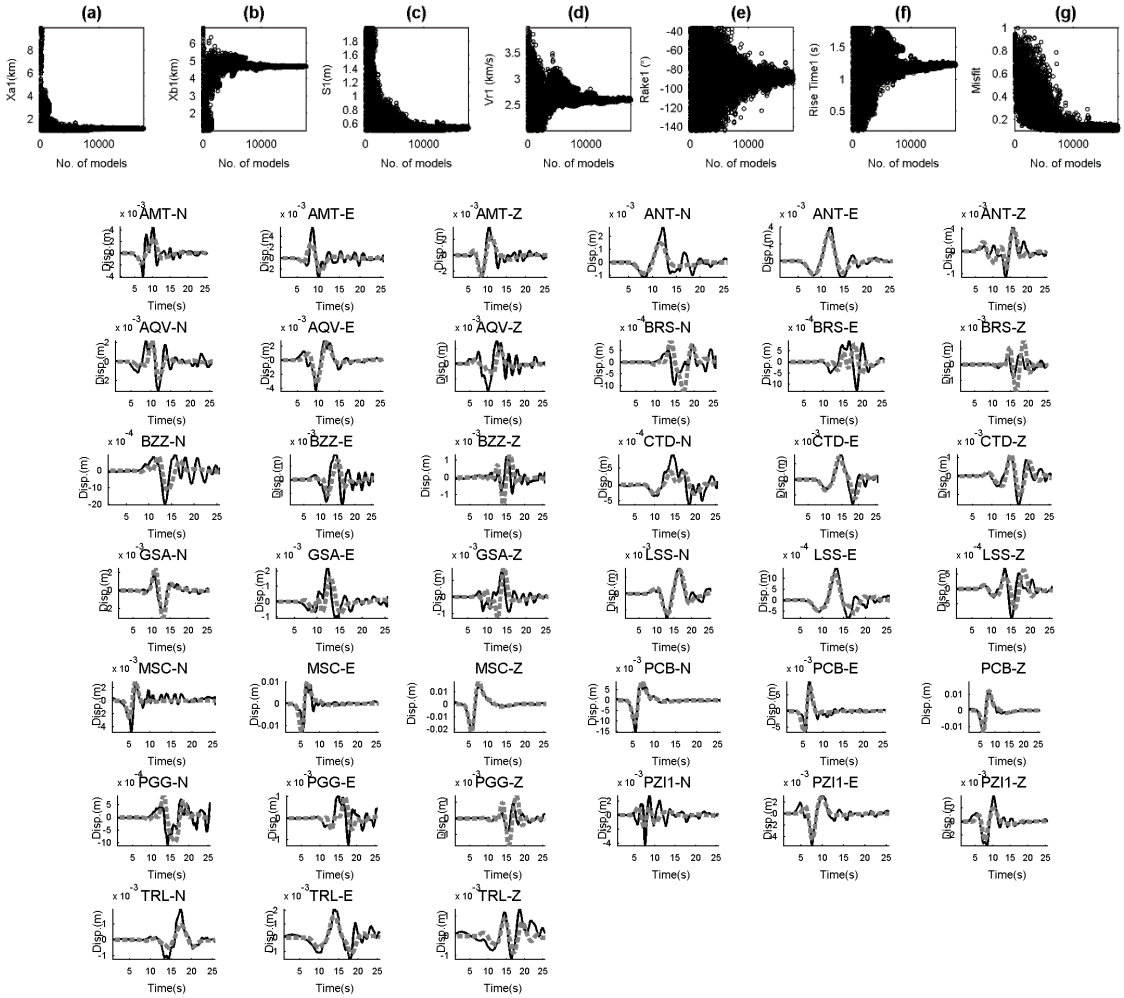

Figure Sb69. A) Convergence of model#9 source parameters obtained for the ML5.3 10:25:24 (GMT) event. b) Waveform fit of the model#9. Black and gray are real and synthetics, respectively.

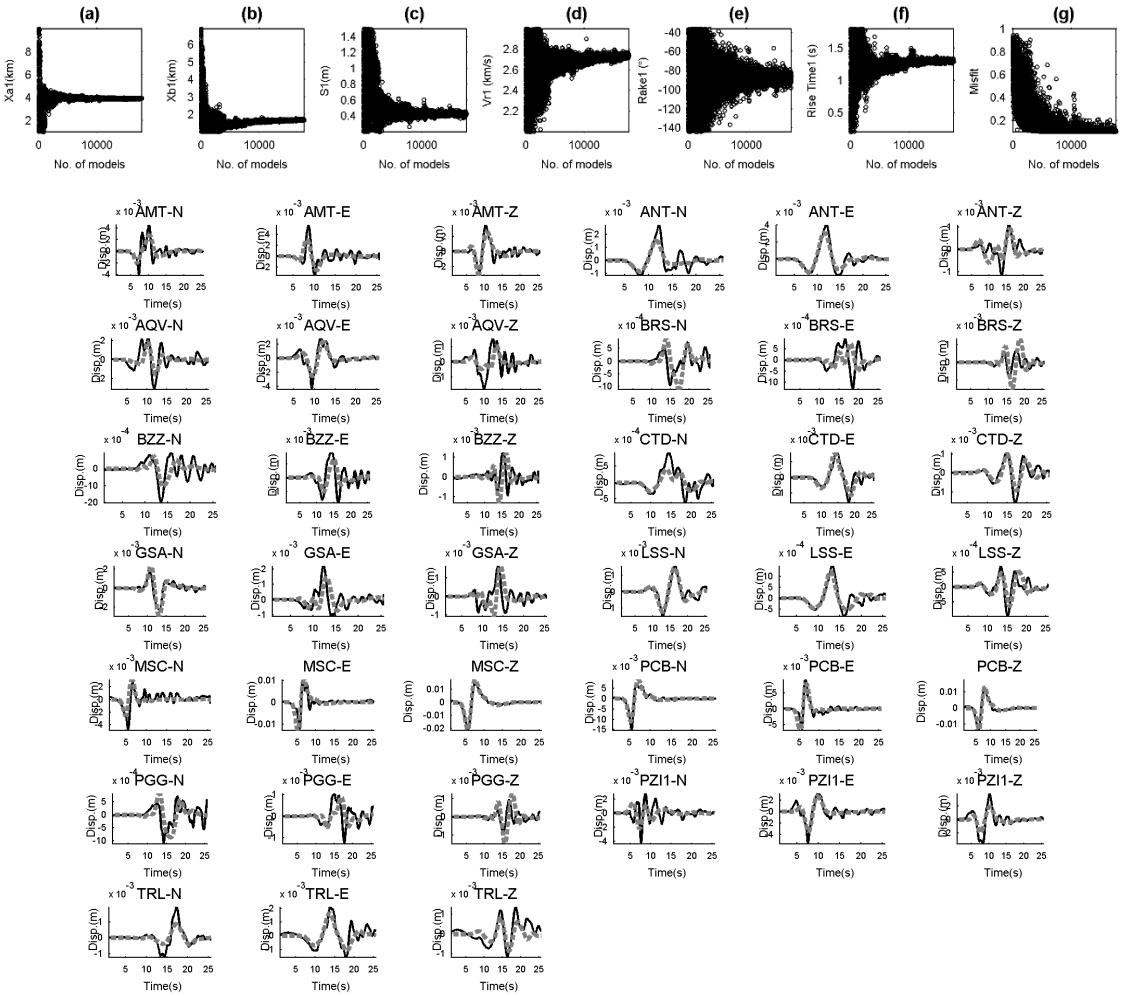

Figure Sb70. A) Convergence of model#10 source parameters obtained for the ML5.3 10:25:24 (GMT) event. b) Waveform fit of the model#10. Black and gray are real and synthetics, respectively.

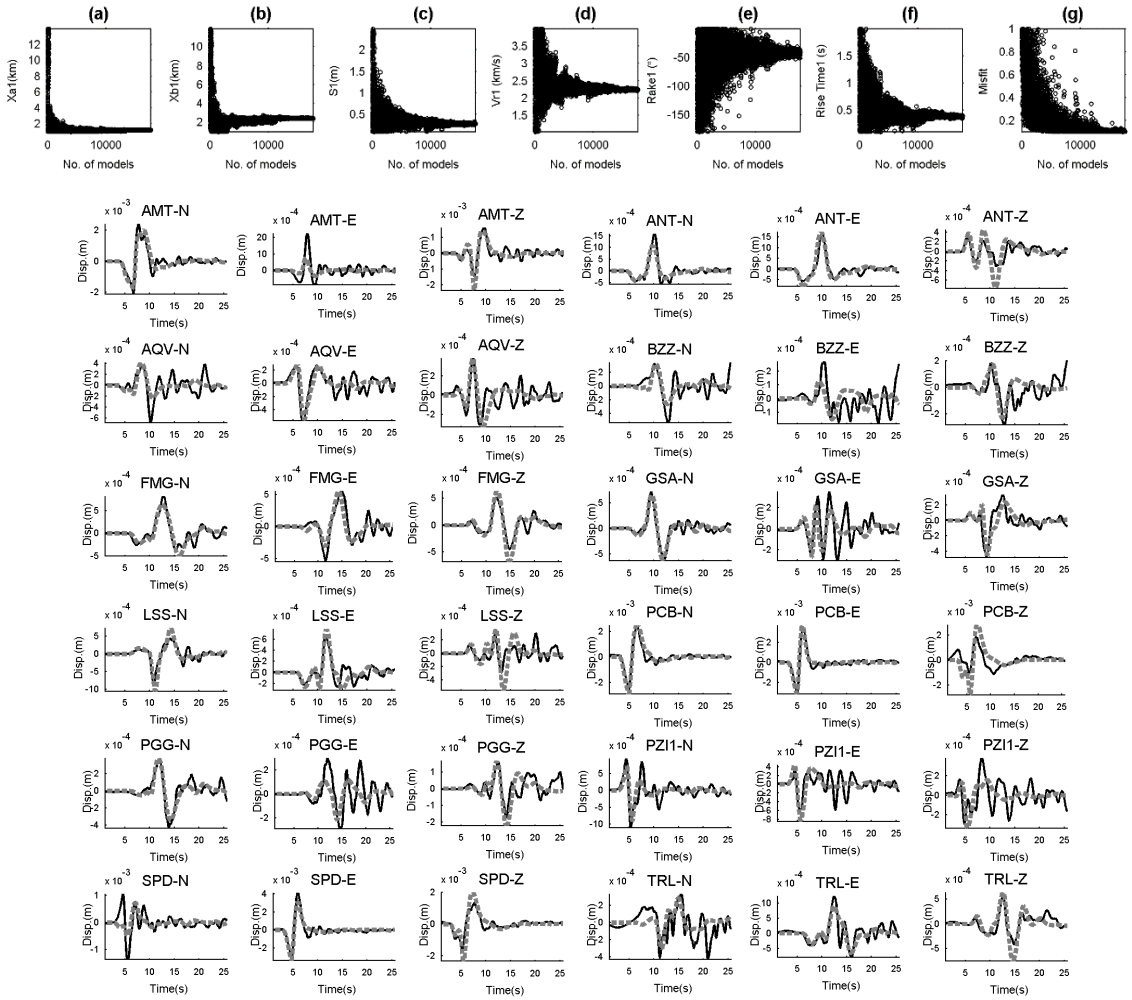

Figure Sb71. A) Convergence of model#1 source parameters obtained for the ML5.1 13:33:37 (GMT) event. b) Waveform fit for the model#1. Black and gray are real and synthetics, respectively.

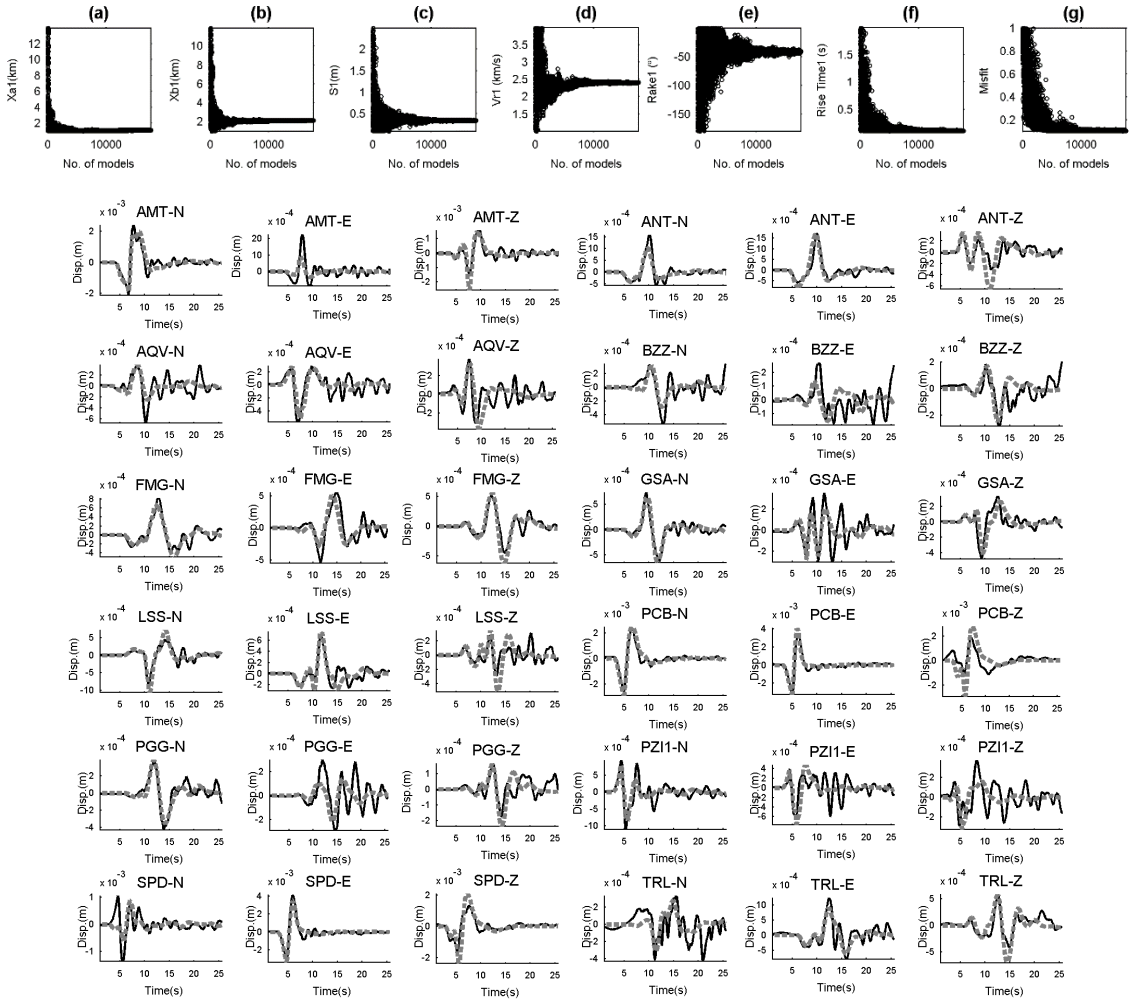

Figure Sb72. A) Convergence of model#2 source parameters obtained for the ML5.1 13:33:37 (GMT) event. b) Waveform fit for the model#2. Black and gray are real and synthetics, respectively.

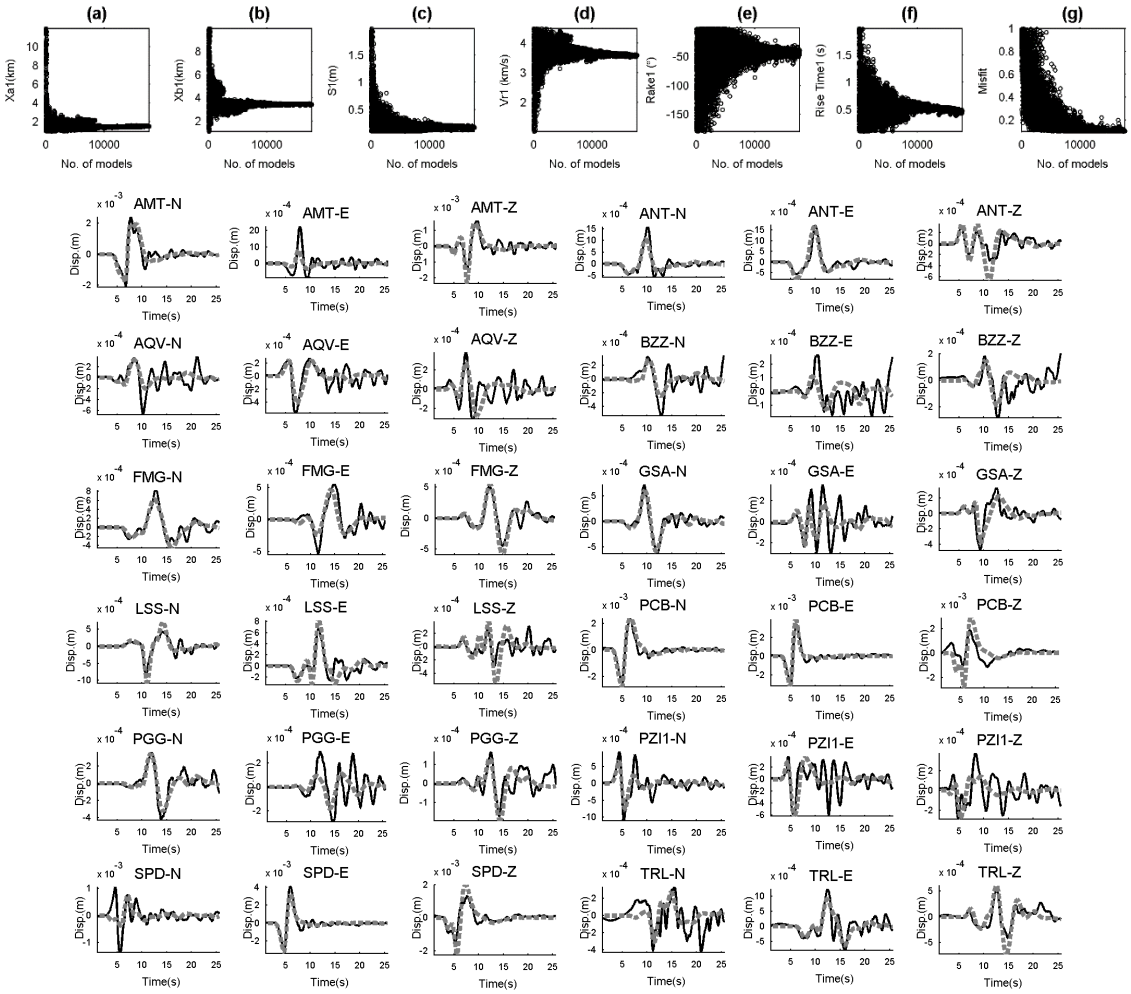

Figure Sb73. A) Convergence of model#3 source parameters obtained for the ML5.1 13:33:37 (GMT) event. b) Waveform fit for the model#3. Black and gray are real and synthetics, respectively.

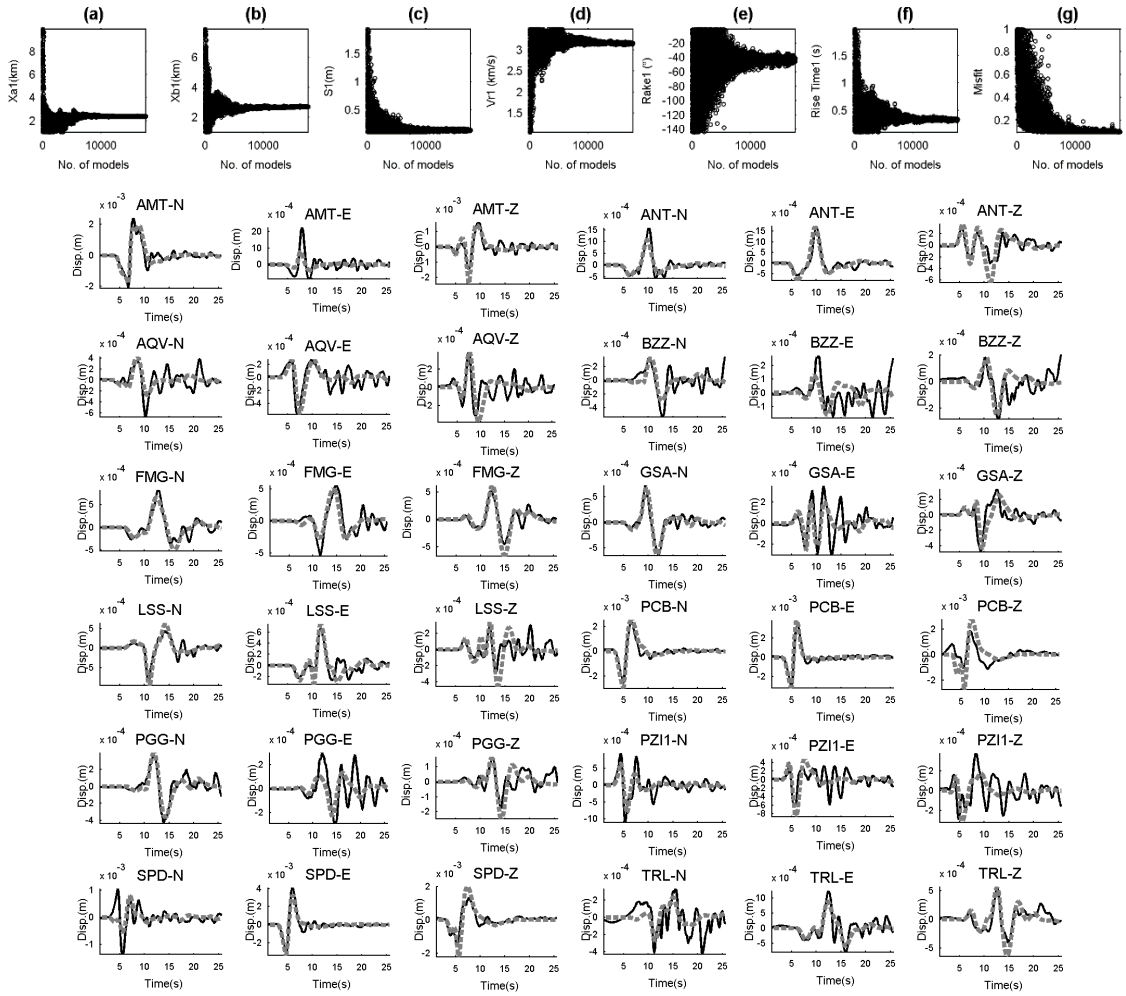

Figure Sb74. A) Convergence of model#4 source parameters obtained for the ML5.1 13:33:37 (GMT) event. b) Waveform fit for the model#4. Black and gray are real and synthetics, respectively.

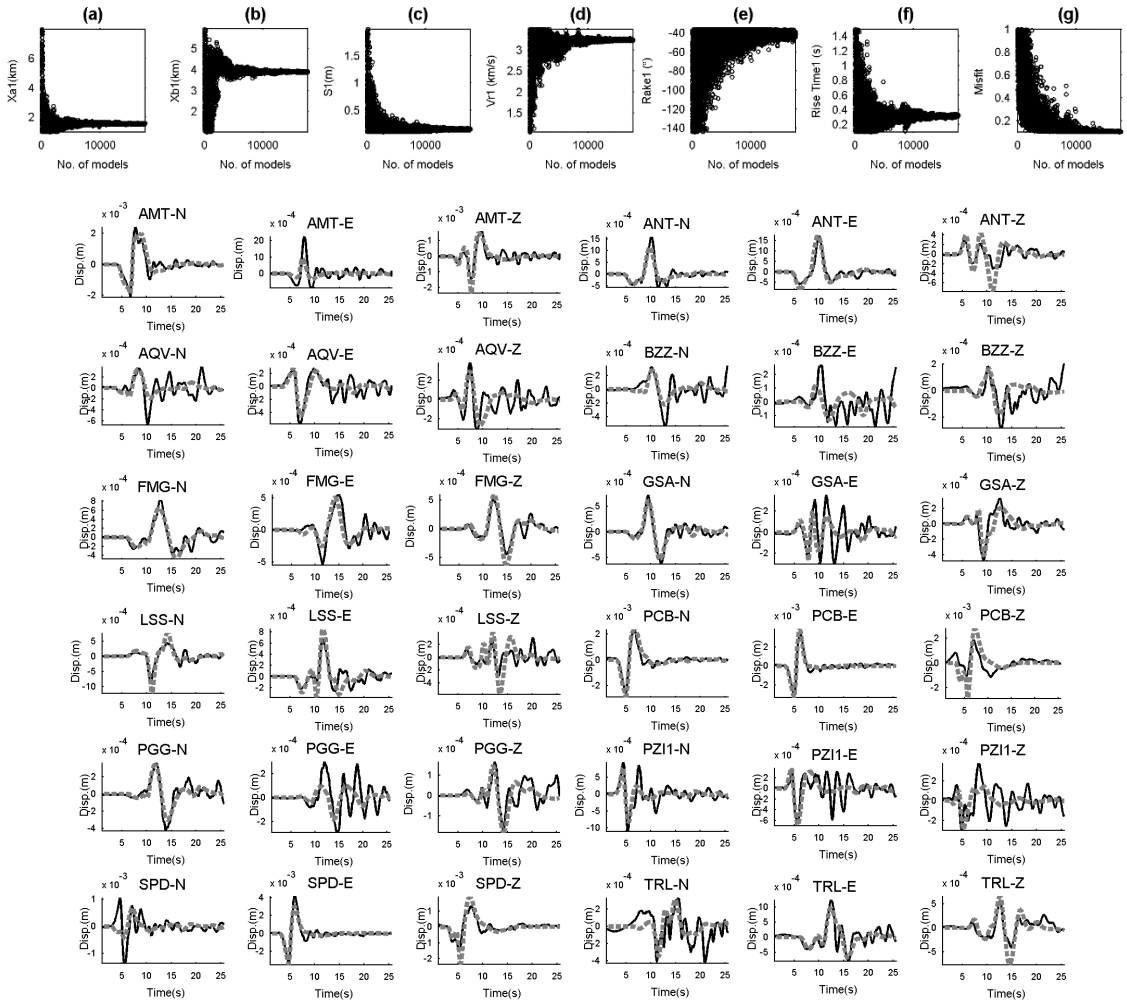

Figure Sb75. A) Convergence of model#5 source parameters obtained for the ML5.1 13:33:37 (GMT) event. b) Waveform fit for the model#5. Black and gray are real and synthetics, respectively.

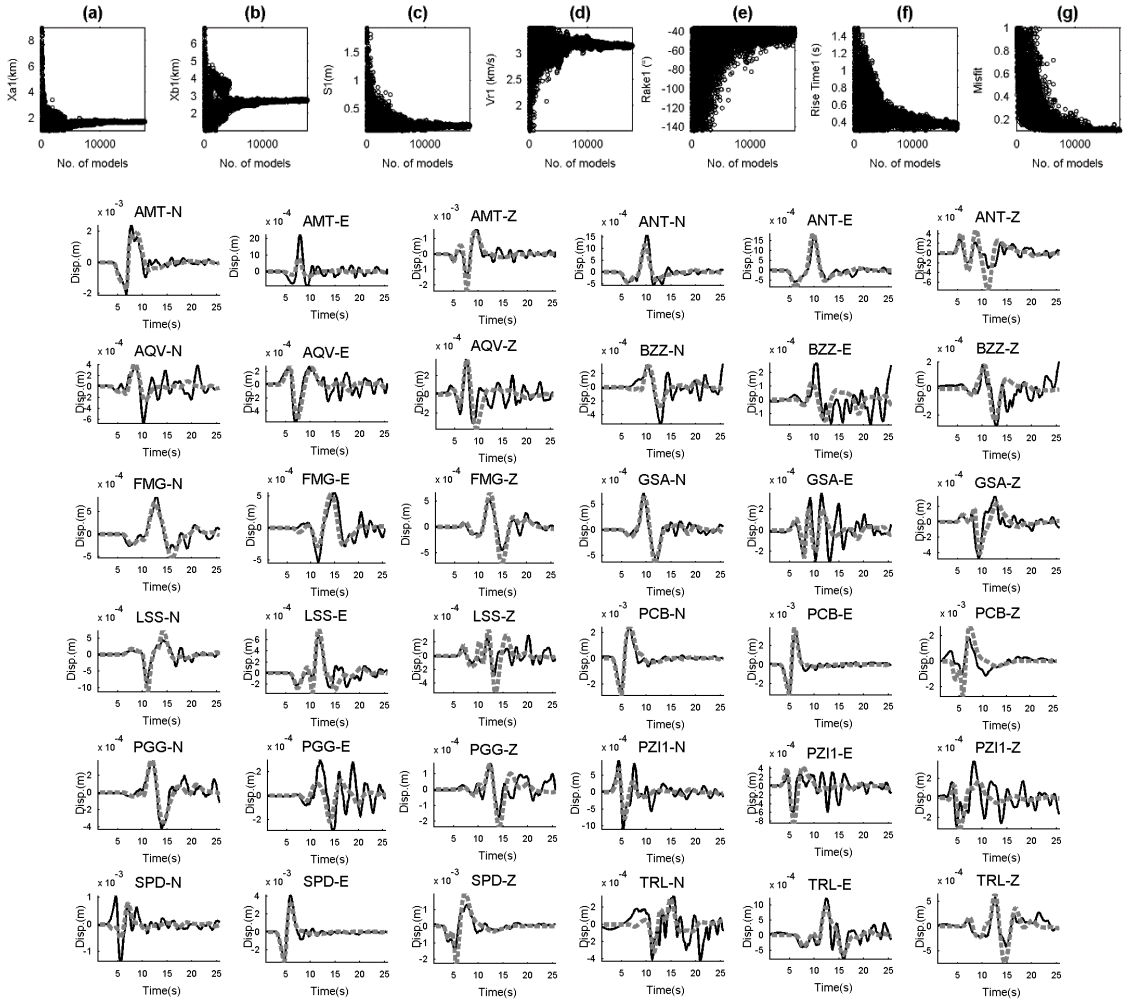

Figure Sb76. A) Convergence of model#6 source parameters obtained for the ML5.1 13:33:37 (GMT) event. b) Waveform fit for the model#6. Black and gray are real and synthetics, respectively.

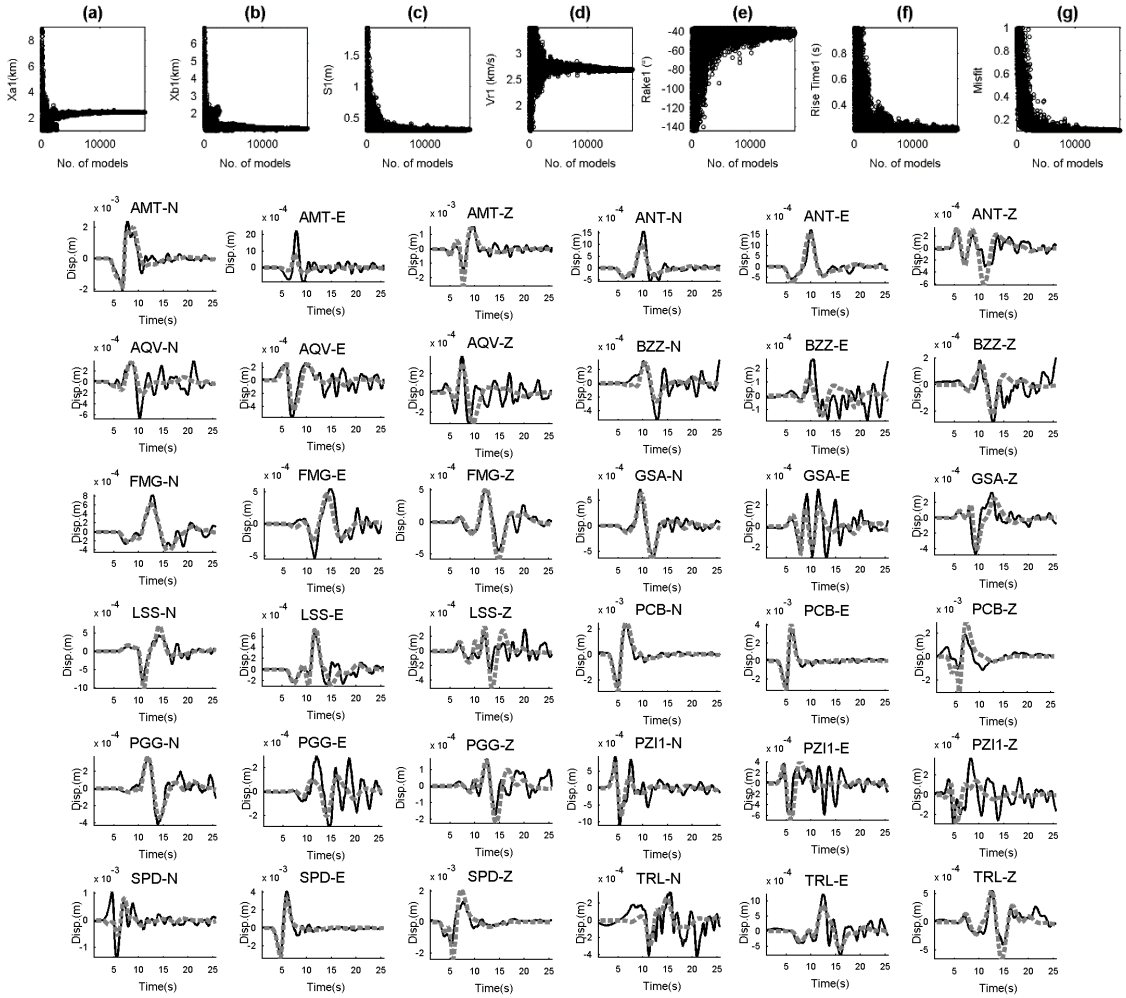

Figure Sb77. A) Convergence of model#7 source parameters obtained for the ML5.1 13:33:37 (GMT) event. b) Waveform fit for the model#7. Black and gray are real and synthetics, respectively.

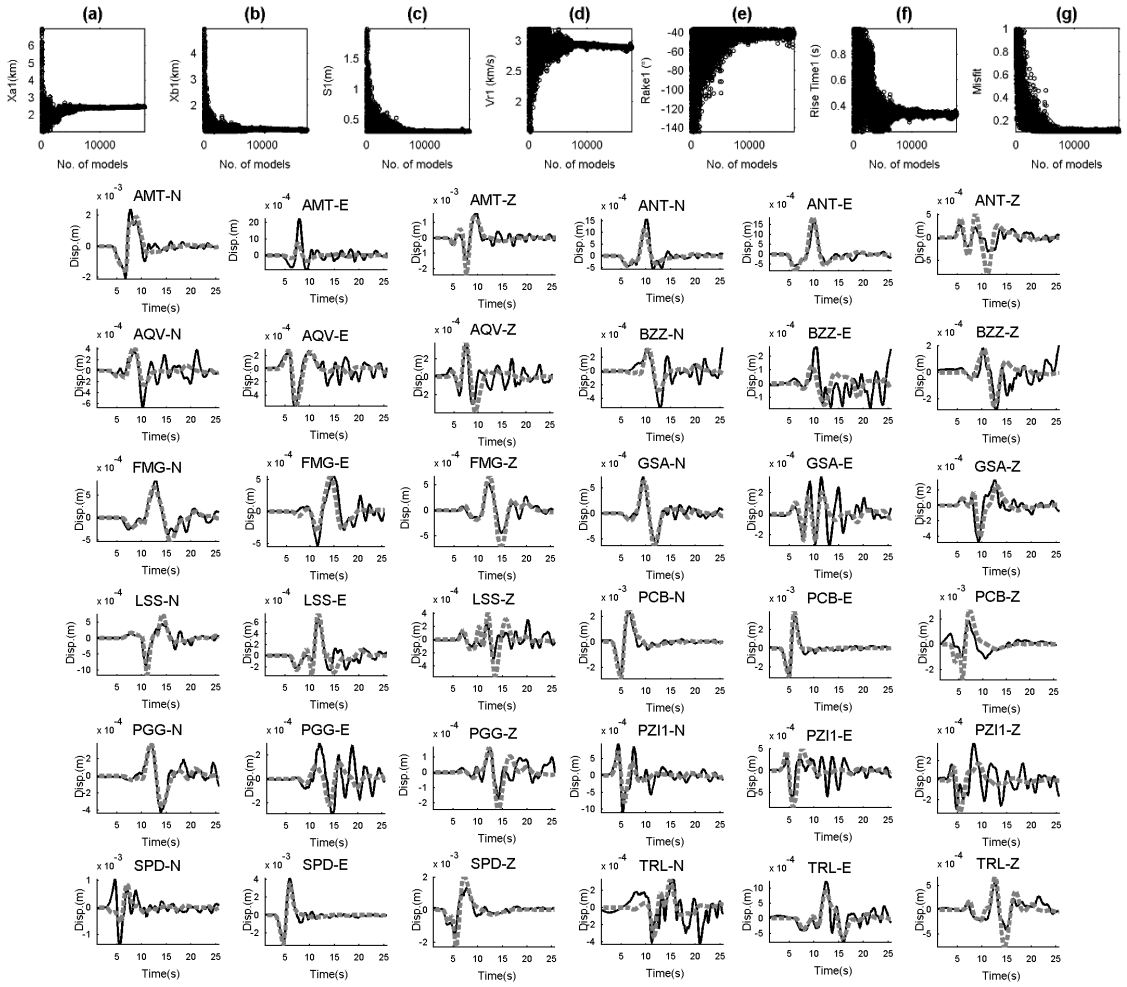

Figure Sb78. A) Convergence of model#8 source parameters obtained for the ML5.1 13:33:37 (GMT) event. b) Waveform fit for the model#8. Black and gray are real and synthetics, respectively.

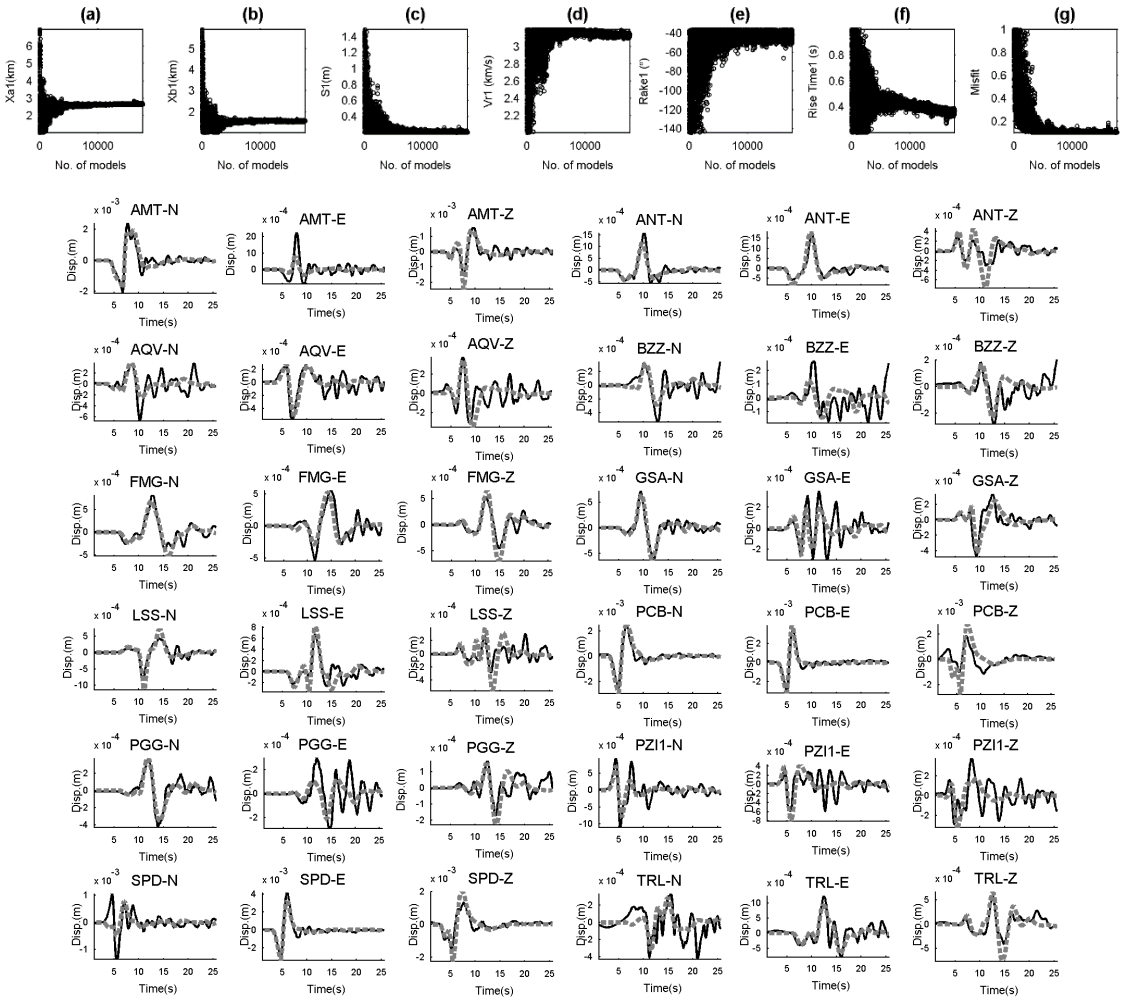

Figure Sb79. A) Convergence of model#9 source parameters obtained for the ML5.1 13:33:37 (GMT) event. b) Waveform fit for the model#9. Black and gray are real and synthetics, respectively.

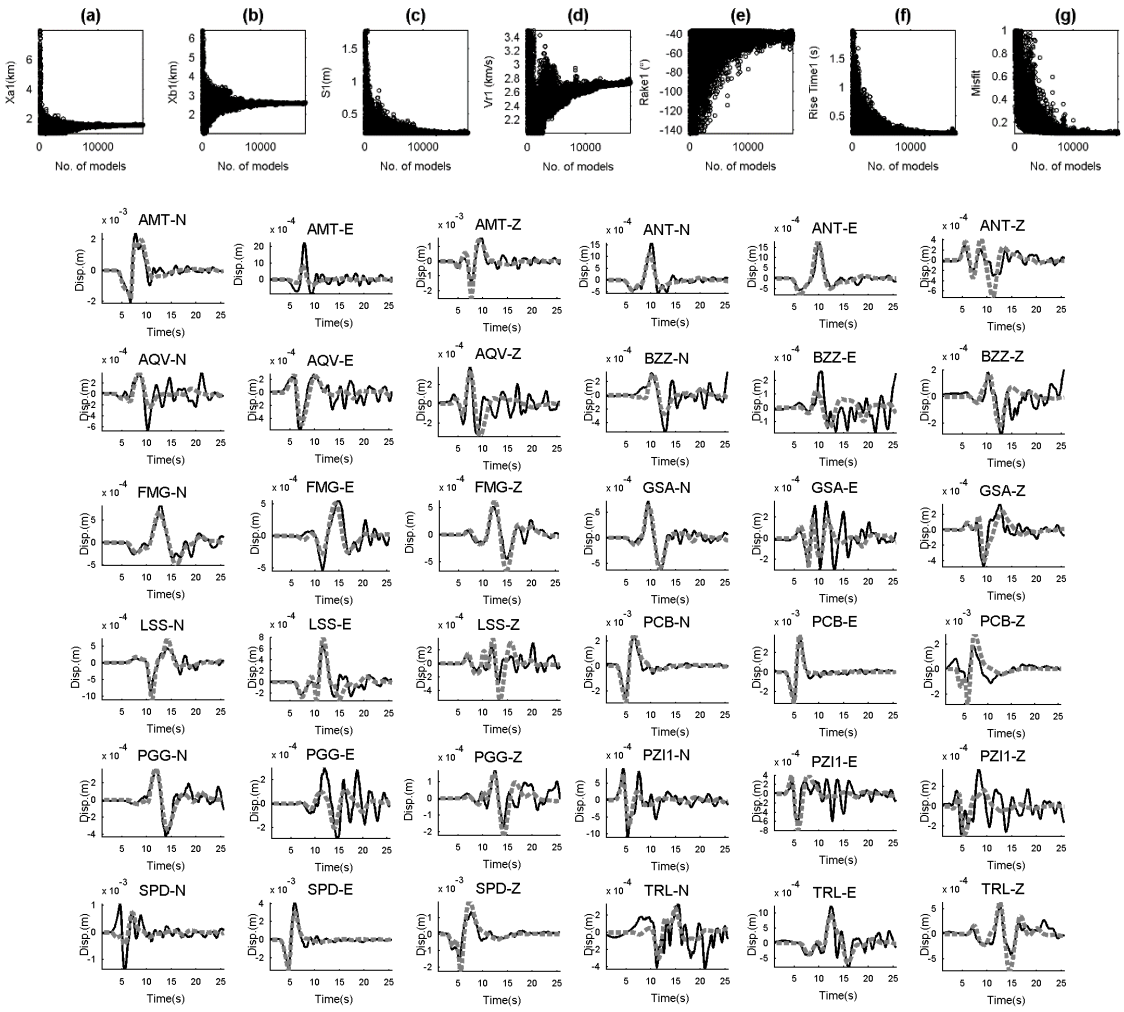

Figure Sb80. A) Convergence of model#10 source parameters obtained for the ML5.1 13:33:37 (GMT) event. b) Waveform fit for the model#10. Black and gray are real and synthetics, respectively.

Tables:

Table Sb1: 10 final source rupture parameters for the 2009/04/06 23:15:36 (GMT) Ml5.0 event. Xa and Xb are the semi-axis of elliptical slip areas. Vr: rupture velocity; Tr: rise time; Mo: scalar seismic moment.

No.	Xa(km)	Xb(km)	Slip(m)	Vr(km/s)	Rake/360(°)	Tr(s)	Mo.(Nm)	Misfit(%)
1	2.47	2.05	0.13	4.0	-0.23	0.02	3.5E16	14.6
2	1.77	1.19	0.29	3.37	-0.23	0.01	3.13E16	15.0
3	2.23	1.35	0.22	2.86	-0.22	0.02	3.35E16	15.9
4	1.44	1.15	0.36	3.0	-0.23	0.01	3.14E16	15.4
5	1.52	1.12	0.35	3.0	-0.23	0.01	3.14E16	15.5
6	2.09	1.12	0.28	3.0	-0.23	0.01	3.35E16	15.1
7	1.60	1.08	0.30	3.49	-0.23	0.01	3.15E16	14.9
8	1.46	1.16	0.37	3.23	-0.22	0.01	3.15E16	15.6
9	2.10	1.21	0.24	3.6	-0.23	0.03	3.32E16	14.6
10	1.79	1.09	0.29	3.68	-0.23	0.03	3.11E16	14.9

Table Sb2: 10 final source rupture parameters for the 2009/04/09 00:52:59 (GMT) Ml5.2 event. Annotations are same to Table-S1.

No.	Xa(km)	Xb(km)	Slip(m)	Vr(km/s)	Rake/360(°)	Tr(s)	Mo(Nm)	Misfit(%)
1	3.30	1.42	0.39	2.59	-0.22	0.17	9.45E16	10.1
2	5.01	1.22	0.32	3.96	-0.23	0.76	1.05E17	10
3	5.27	1.60	0.25	3.55	-0.22	0.76	1.05E17	10
4	4.29	1.06	0.43	3.20	-0.23	0.64	9.90E16	9.8
5	4.52	1.97	0.22	3.24	-0.23	0.58	1.00E17	10
6	3.88	1.51	0.32	2.74	-0.23	0.23	9.70E16	9.8
7	3.76	1.29	0.41	2.92	-0.23	0.45	9.71E16	9.9
8	2.89	1.10	0.53	2.73	-0.23	0.62	9.24E16	10
9	2.81	1.51	0.41	2.30	-0.23	0.06	9.16E16	10
10	3.72	2.20	0.24	2.97	-0.23	0.26	9.62E16	10

Table Sb3: 10 final source rupture parameters for the 2009/04/09 19:38:17 (GMT) Ml5.0 event. Annotations are same to Table-S1.

No.	Xa(km)	Xb(km)	Slip(m)	Vr(km/s)	Rake/360(°)	Tr(s)	Mo(Nm)	Misfit(%)
1	9.99	1.13	0.1	3.99	-0.22	0.18	3.45E16	7.6
2	1.61	1.0	0.41	3.75	-0.22	0.84	3.44E16	7.4
3	1.56	1.01	0.42	2.96	-0.21	0.78	3.44E16	7.4
4	1.51	1.01	0.43	3.4	-0.21	0.84	3.55E16	7.4
5	1.53	1.0	0.42	3.0	-0.21	0.78	3.44E16	7.4
6	2.23	1.37	0.23	3.14	-0.22	0.68	3.47E16	7.3
7	2.74	1.16	0.2	3.2	-0.22	0.57	3.47E16	7.3
8	2.16	1.3	0.22	2.45	-0.22	0.4	3.24E16	7.4
9	1.14	1.0	0.66	2.5	-0.21	0.75	3.34E16	7.4
10	1.19	1.0	0.66	2.8	-0.22	0.82	3.42E16	7.4

Table Sb4: 10 final source rupture parameters for the 2009/06/22 20:58:40 (GMT) Ml4.4 decollement event. Annotations are same to Table-S1.

No.	Xa(km)	Xb(km)	Slip(m)	Vr(km/s)	Rake/360(°)	Tr(s)	Mo(Nm)	Misfit(%)
1	2.11	1.13	0.05	4.0	-0.46	0.09	5.43E15	8.8
2	1.72	1.21	0.05	3.04	-0.47	0.07	5.37E15	8.9
3	1.87	1.15	0.05	4.0	-0.46	0.05	5.18E15	8.9
4	1.29	1.11	0.07	2.8	-0.47	0.07	5.44E15	8.9
5	1.33	1.02	0.08	3.03	-0.46	0.08	5.37E15	8.9

6	1.27	1.26	0.07	3.61	-0.46	0.06	5.18E15	8.8
7	1.60	1.08	0.06	3.3	-0.46	0.05	5.31E15	8.8
8	1.44	1.02	0.07	3.47	-0.46	0.09	5.18E15	8.9
9	1.53	1.16	0.06	2.92	-0.47	0.08	5.31E15	8.9
10	1.76	1.03	0.06	3.27	-0.46	0.06	5.57E15	8.8

Table Sb5: 10 final source rupture parameters for the 2017/01/18 09:25:40 (GMT) Ml5.4 event. Annotations are same to Table-S1.

No.	Xa(km)	Xb(km)	Slip(m)	Vr(km/s)	Rake/360(°)	Tr(s)	Mo(Nm)	Misfit(%)
1	4.26	2.82	0.13	3.99	-0.25	0.11	8.15E16	9.6
2	2.96	1.23	0.37	3.42	-0.24	0.10	7.45E16	10
3	2.89	2.21	0.24	3.42	-0.24	0.10	7.51E16	10
4	3.03	1.82	0.26	3.50	-0.24	0.10	7.51E16	10
5	3.89	1.63	0.22	3.80	-0.25	0.10	7.77E16	9.5
6	3.73	2.74	0.15	3.80	-0.25	0.10	8.15E16	9.7
7	3.90	2.77	0.15	3.71	-0.24	0.10	8.08E16	9.7
8	2.94	0.70	0.50	3.31	-0.24	0.10	7.90E16	10
9	2.72	1.07	0.48	3.00	-0.24	0.10	7.53E16	11.4
10	4.56	1.09	0.32	3.64	-0.25	0.05	7.74E16	9.7

Table Sb6: 10 final source rupture parameters for the 2017/01/18 10:14:10 (GMT) Ml5.4 event. Annotations are same to Table-S1.

No.	Xa(km)	Xb(km)	Slip(m)	Vr(km/s)	Rake/360(°)	Tr(s)	Mo(Nm)	Misfit(%)
1	5.58	1.01	0.92	3.71	-0.20	1.23	2.98E17	10.9
2	5.12	1.59	0.53	3.73	-0.19	1.17	2.70E17	10.7
3	8.01	2.96	0.25	3.33	-0.20	0.78	2.97E17	11.2
4	4.86	2.08	0.48	3.59	-0.19	1.11	2.66E17	10.5
5	4.91	1.0	1.0	3.6	-0.19	1.23	2.80E17	10.7
6	4.47	2.84	0.36	3.38	-0.18	1.02	2.68E17	11.9
7	6.43	1.56	0.54	3.53	-0.20	0.97	3.01E17	10.2
8	5.61	1.96	0.45	3.4	-0.19	0.80	2.67E17	10.5
9	5.01	2.91	0.3	3.45	-0.19	0.86	2.59E17	11.1
10	4.73	1.01	0.88	3.9	-0.19	1.19	2.74E17	11.9

Table Sb7: 10 final source rupture parameters for the 2017/01/18 10:25:24 (GMT) Ml5.3 event. Annotations are same to Table-S1.

No.	Xa(km)	Xb(km)	Slip(m)	Vr(km/s)	Rake/360(°)	Tr(s)	Mo(Nm)	Misfit(%)
1	6.55	3.57	0.16	2.97	-0.25	1.06	2.01E17	9.7
2	3.99	1.27	0.61	2.79	-0.25	1.35	1.75E17	9.9
3	3.78	1.39	0.58	2.72	-0.25	1.33	1.74E17	9.9
4	4.73	1.12	0.62	2.80	-0.25	1.44	1.81E17	10
5	5.58	3.71	0.17	2.76	-0.25	1.20	1.95E17	9.2
6	5.81	3.90	0.16	2.77	-0.25	1.12	1.94E17	9.3
7	6.55	3.57	0.16	2.97	-0.25	1.06	2.11E17	9.9
8	4.86	1.38	0.50	2.64	-0.24	1.37	1.86E17	10.3
9	4.69	1.19	0.55	2.60	-0.25	1.22	1.67E17	10.1
10	3.91	1.66	0.43	2.74	-0.24	1.30	1.78E17	10.2

Table Sb8: 10 final source rupture parameters for the 2017/01/18 13:33:37 (GMT) Ml5.1 event. Annotations are same to Table-S1.

No.	Xa(km)	Xb(km)	Slip(m)	Vr(km/s)	Rake/360(°)	Tr(s)	Mo(Nm)	Misfit(%)

1	3.62	2.25	0.11	3.29	-0.12	0.31	4.53E16	9.8
2	2.12	1.13	0.35	2.41	-0.12	0.1	4.45E16	10.8
3	3.41	1.55	0.17	3.58	-0.12	0.47	4.61E16	10.2
4	2.71	2.36	0.13	3.16	-0.12	0.33	4.50E16	9.9
5	3.87	1.54	0.16	3.25	-0.12	0.32	4.61E16	10
6	2.77	1.72	0.19	3.15	-0.12	.37	4.48E16	10.1
7	2.45	1.13	0.32	2.68	-0.12	.21	4.48E16	10.4
8	2.47	1.06	0.30	2.9	-0.12	.34	4.30E16	10.4
9	2.68	1.56	0.20	3.14	-0.12	.36	4.40E16	10.1
10	2.62	1.58	0.2	2.73	-0.12	.20	4.45E16	10.1

Appendix-C - GPS data analysis

We have provided the IGS08 position time-series used in this work by the repository of the Nevada Geodetic Laboratory (Blewitt et al, 2018). From this database we selected the continuous GPS (cGPS) stations staying along the Apennines Chain, from the area characterized by the Alto Tiberina Fault (ATF) to the southern zone hit by the 2009 April 6 Mw 6.3 L'Aquila earthquake (Fig. Sc1).
The time series of the selected stations have been analysed following the procedure approach as in Barzaghi and Borghi (2018) that included the estimate of discontinuities due to station equipment changes and seismic events, as the 2009 L'Aquila earthquake, the estimate of periodic signals and a linear velocity term, considering the time correlation between data. The time-series has been filtered in time using the least-square collocation method with the covariance functions obtained by the analysis of the temporal correlation (Borghi et al., 2009; Borghi et al., 2016). The data are also spatial filtered to remove spatial correlated noise using the PCA (Principal Component Analysis), as suggested by Dong et al. (2006).
The aim of this study was the investigation of the geodetic data for possible signals associated to fault creeping or slow slip events, as some similar signals have already been found and reported in literature: analysis of cGPS Borghi et al. (2016) discovered that the 2009 L'Aquila mainshock was preceded by a slow slip event in the Campotosto fault; Gualandi et al. (2017) highlighted an aseismic deformation in the area of the ATF, that the authors correlated to the earthquake swarm that was ongoing in the area. Moreover, non-tectonic transient signals have been highlighted in the Central Apennines by integrating the GPS time-series with hydrological data, as temperature, monthly rainfall and daily spring discharge (Silverii et al., 2019), but the cGPS sites that present a higher correlation with the hydrological records are not the ones involved in this analysis, even if Silverii et al. (2019) have analysed the GPS stations of Fig. Sc1 as well.
As the procedure described in Borghi et al. (2016) has been demonstrated to be efficient in solving this type of problems we have applied the same procedure, looking for transient deformations in the principal components of the PCA. This approach has been also improved considering other methods, which are used in so-called blind source separation (BSS) problem as Fast Independent Component Analysis (ICA), fast fixed-point ICA (acffpICA) (Hyvärinen & Oja, 2000), and the variational Bayesian Independent Component Analysis (vbICA) (Choudrey & Roberts, 2003), the last one already used in GPS time series as in Gualandi et al. (2016) and Gualandi et al. (2017).

At first, we tested again our methodology looking for the aseismic deformation in the ATF reported in Gualandi et al. (2017), so we consider a temporal interval from 2012 to 2015 and the 11 stations available in this area. If we consider separately the coordinate components (N,E,U) the second principal component of the coordinate North and a component of the vbICA shows a discontinuity at the end of 2013 that the Bayesian test (Borghi et al., 2012) quantifies around the days of the years (356 ± 5) and (358 ± 5) with a total probability of the 97% and 99%, respectively, as shown in Fig. Sc2. The main foreshocks of the seismic swarm occurred in December 18 and 22, 2013, that in DoY 352 and 356, so the discontinuities highlighted by the component analyses could be reasonably interpreted as the co-seismic displacement due to these two seismic events (Fig. Sc2). Gualandi et al. (2017) highlighted this not seasonal behaviour in the fourth Independent Component (IC), but they didn't try to fix the time where the signal happened and they have interpreted this signal as an aseismic deformation indeed. So this first analysis in the ATF zone succeeded and we decided to continue the analysis including the southern stations and considering the time interval from 2015 to the day before the 20016 August 24 Mw 6 Amatrice earthquake.
The analysed network is reported in Fig. Sc1 and presents an empty zone in the area hit by the mainshock, because no stations were installed in that period or we do not have the available data. Although the vbICA method has resulted to be very efficient in finding the signal in the ATF zone, we preferred to apply also the PCA method, because this method allows finding the average behaviour of the stations and avoids interpretation of local effects. In this case the second Principal Component (PC2) of the East component presents an increasing of the values starting around the beginning of 2016 and the contribution of each single station to this PC2 seems to be geographically clustered. So, we repeated the analysing splitting the stations in the Northern part of the network (ATF) and in the southern part of the network. These two-separated analyses allowed us to point out a similar behaviour of the ATF and Campotosto stations but shifted in time: the Campotosto stations present this discontinuity in the first vbICA component at the beginning of 2016, at January 7 with a probability around the 94% as detected by the Bayesian test inference, whereas the ATF stations present an analogous behaviour seven months later in July 7 with a probability of 98% (Fig. 3 of the manuscript).

The last analysis performed involves the cGPS stations that have been set up after the 2016 October 30 Mw 6.5 of the Amatrice, Norcia, Visso sequence (Fig. Sc1): CESI, CTEL, GUMA, FOL1, MNCO, PREC, USSI. The plots of the times-series clearly show the no-linear effect of a post-seismic deformation, so we preferred to no fit the data using any functional models but performing the component analysis to describe this deformation. In Fig.

Sc3 the first and second principal components are reported. All the stations have affected by a common signal represented by the linear tectonic rate and the post-seismic deformations, as shown by the first PC (Fig. Sc3), but a discontinuity seems to be present at the beginning of 2018 and it is added to the other signals in the first and second PC (Fig. Sc3)

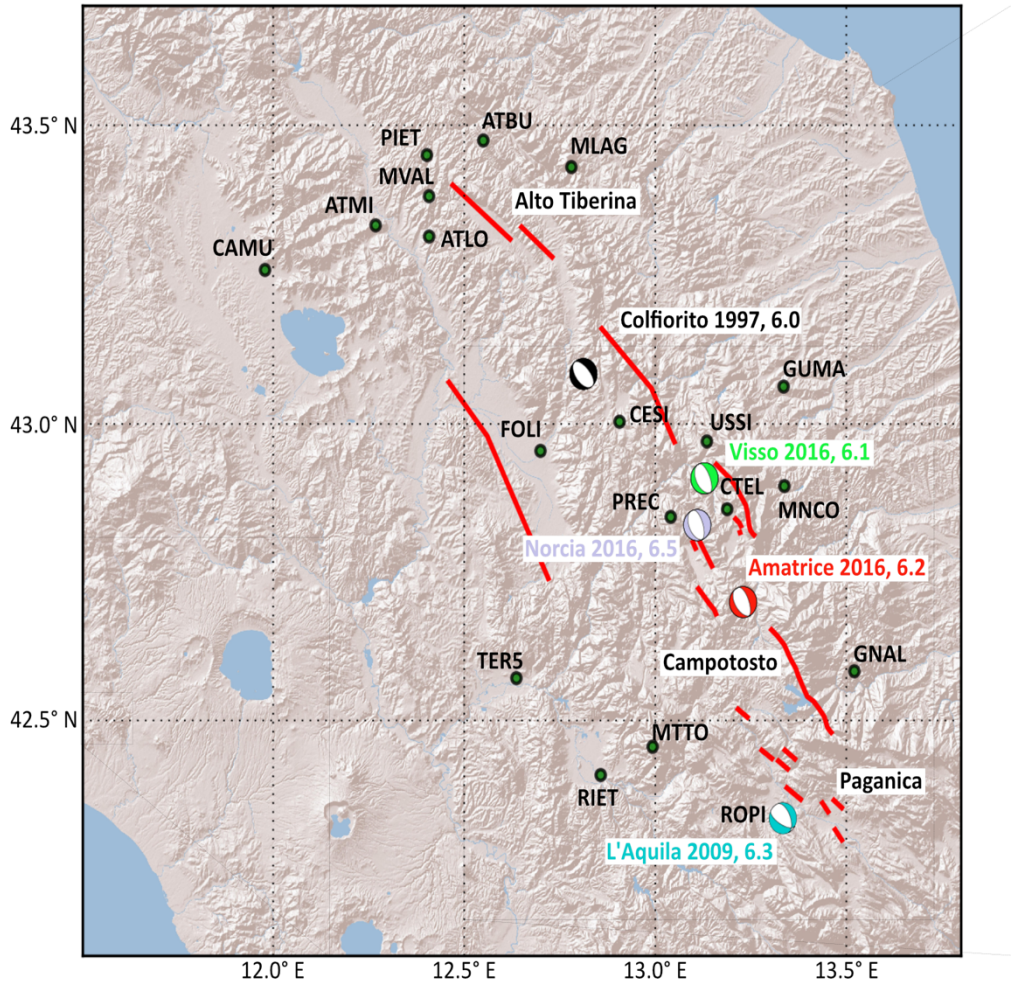

Figure Sc1 – Map of the GPS stations taken into account in this analysis. The stations around the seismic events of Norcia and Visso 2016, CTEL, MNCO, PREC, USSI, have been set up after the seismic events.

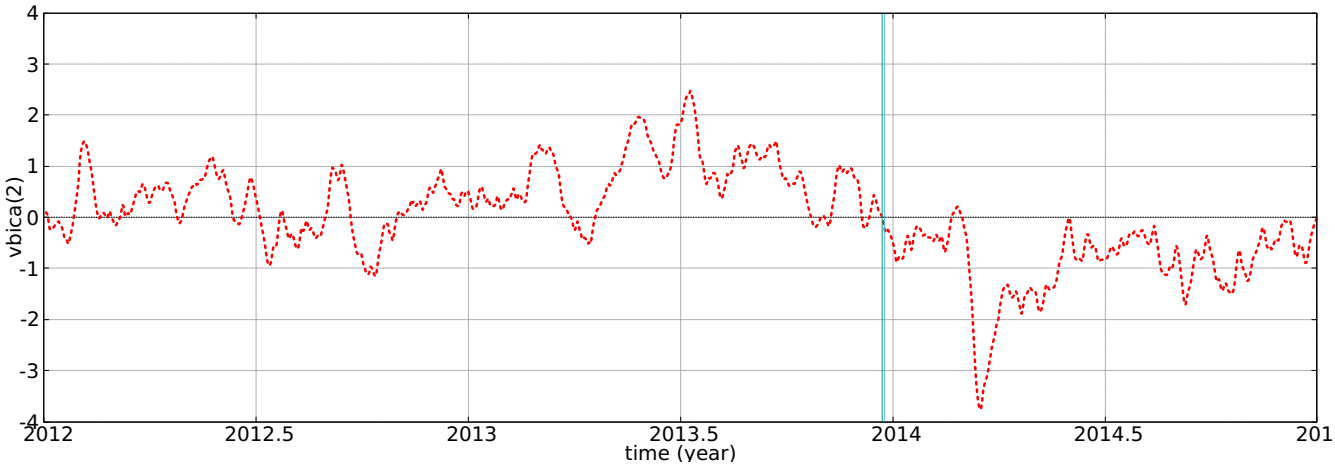

Figure Sc2 – Second independent component of the vbICA of the North component (red dashed line) of the stations in the ATF zone from 2012 to 2015: the green line (the first from the left) represents the December 22nd when the biggest seismic event of the seismic swam happened, the light-blue line is the discontinuities epoch found by the Bayesian test.

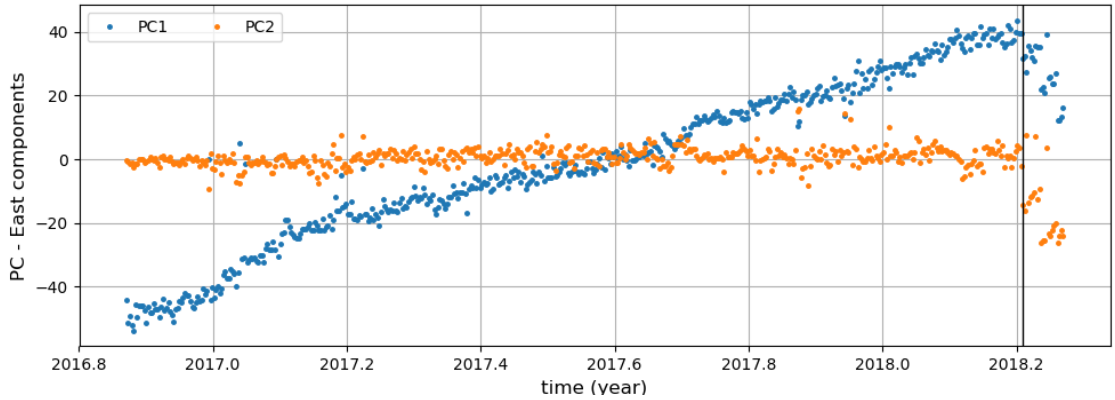

Figure Sc3 - First and second principal components for the East components of the stations set up after the Amatrice, Norcia, Visso sequence. The vertical black line represents the discontinuity indicated by the Bayesian inference.

References

Borghi A., Aoudia A., Riva R., Barzaghi R. (2009). GPS monitoring and earthquake prediction: a success story towards a useful integration. Tectonophysics, 465, pp 177-189, ISSN 0040-1951, doi: 10.1016/j.tecto.2008.11.022

Borghi, A., L. Cannizzaro, A. Vitti (2012). Advanced techniques for discontinuities detection in GNSS coordinate time-series. An Italian case study. Proceedings of IAG 2009 Scientific Assembly "Geodesy for Planet Earth", Buenos Aires, August 31 to September 4, 2009, Springer, ISBN 978-364220337-4, DOI 10.1007/978-3-642-20338-1_77

Borghi, A., A. Aoudia, F. Javed and R. Barzaghi (2016), Precursory slow-slip loaded the 2009 L'Aquila earthquake sequence, Geophysical Journal International 205(2), DOI: 10.1093/gji/ggw046

Barzaghi, R. and A. Borghi (2018), Theory of second order stationary random processes applied to GPS coordinate time-series, GPS Solutions 22(3), DOI: 10.1007/s10291-018-0748-4

Blewitt, G., W. C. Hammond, and C. Kreemer (2018), Harnessing the GPS data explosion for interdisciplinary science, Eos, 99, https://doi.org/10.1029/2018EO104623.

Choudrey, R.A. and Roberts, S.J. (2003), Variational Mixture of Bayesian Independent Component Analyzers, Neural Computation 2003 15:1, 213-252, https://doi.org/10.1162/089976603321043766.

Dong, D., P. Fang, Y. Bock, F. Webb, L. Prawirodirdjo, S. Kedar, and P. Jamason (2006), Spatiotemporal filtering using principal component analysis and Karhunen-Loeve expansion approaches for regional GPS network analysis, J. Geophys. Res., 111, B03405, doi:10.1029/2005JB003806.

Gualandi A., E. Serpelloni and M. E. Belardinelli (2016), Blind source separation problem in GPS time series, J Geod (2016) 90:323–341, DOI 10.1007/s00190-015-0875-4

Gualandi, A., C. Nichele, E. Serpelloni, L. Chiaraluce, L. Anderlini, D. Latorre, M. E. Belardinelli, and J.-P. Avouac (2017), Aseismic deformation associated with an earthquake swarm in the northern Apennines (Italy), Geophys. Res. Lett., 44, 7706–7714, doi:10.1002/2017GL073687.

Hyvärinen, A. & Oja, E. (2000), Independent component analysis: algorithms and applications. Neural networks 13 (4-5), 411-430, https://doi.org/10.1016/S0893-6080(00)00026-5

Silverii, F., N. D'Agostino, A. A. Borsa, S. Calcaterra, P. Gambino, R. Giuliani, M. Mattone (2019), Transient crustal deformation from karst aquifers hydrology in the Appennines (Italy), Earth and Planetary Science Letters 506 (2019) 23-37, doi: 10.1016/j.epsl.2018.10.019.